Department of Precision and Microsystems Engineering

Correlating Fluorescence and Stress/Strain for Spiropyran Mechanosensors

Anuj Joshi

Report no	: 2024.025
Committee	: Dr. Siddhant Kumar, Dr. Georgy Filonenko
	: Dr. Murali Ghatkesar, Dr.ir. Sophinese Iskander-Rizk
Specialisation	: Micro and Nano Engineering
Type of report	: Masters Thesis
Date	: May 31, 2024

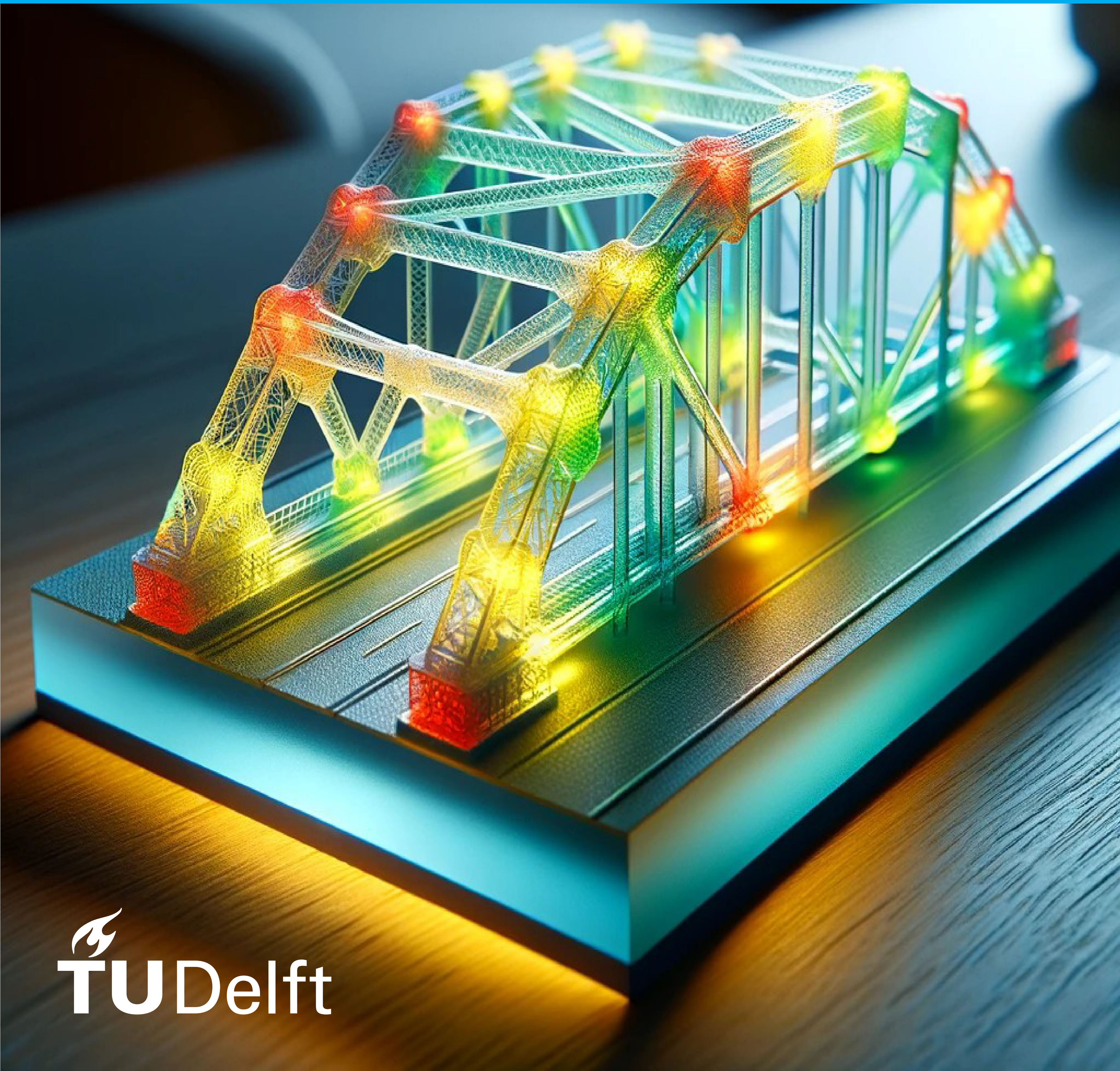

TU Delft

Correlating Fluorescence and Stress/Strain for Spiropyran Mechanosensors

by

Anuj Joshi

Student Name	Student Number
Anuj Joshi	5713560

Committee:	Dr. Sid Kumar, Dr. Georgy Filonenko, Dr. Murali Ghatkesar. Dr.ir. Sophinese Iskander-Rizk
Project Duration:	August, 2023 - May, 2024
Faculty:	Faculty of Mechanical Engineering, Delft

TU Delft

Acknowledgements

My time while pursuing an MSc in Mechanical (High-Tech) Engineering has been beyond rewarding for my career. Apart from shaping my skills in mechanical design engineering, it has given me a new research inclination towards the field of continuum mechanics, hence motivating my thesis topic.

The success of this MSc Thesis project is vastly attributed to my great supervisors Sid, Georgy and Murali. Your approach made the research process both enjoyable and productive. I would further like to extend my gratitude towards my colleagues at the Functional Polymers and Sensors (FPS) group and Mechanics, Materials and Computation Lab respectively, for their timely insights and assistance. Lastly, I would like to thank Eveline Matroos, the track coordinator of High-Tech Engineering for making day-to-day processes seamless.

I would also like to thank my mom, dad and Harsh for their unconditional love and support throughout my academics and career. Thanks to Preksha for supporting me, and keeping me sane these two years. Thanks to the ”Haye-Tech” gang for being with me during all the celebrations, main quest and of course, my side quests as well. Finally, I would take this moment to share this beautiful quote that motivated me and helped me get through tough times - "कोई लोड नहीं। कल की कल देखेंगे।"

Anuj Joshi
Delft, June 2024

Abstract

When designing mechanical components, they commonly undergo multiple modeling phases for stress determination using analytical or numerical methods like the Finite Element Method (FEM). This is followed by experimental validation performed via stress mapping to identify and account for possible mechanical failure within the design phase. Among the experimental stress mapping techniques, mechanosensing is gaining rapidly increasing attention by research and industry. Mechanosensing is a chemistry-based technique that utilizes molecules called mechanophores. When mechanophores are embedded in transparent polymers, they act as mechanical probes sensing stress/strain throughout the polymer by emitting fluorescence under deformation. While studies have shown the capabilities of mechanophores as stress/strain probes qualitatively, it is currently not known how the mechanophore activation is correlated with the stress/strain-based quantities from a solid mechanics perspective. This study addresses this problem from a phenomenological viewpoint to fill the research area gap. In this work, using a uniaxial tensile testor, experiments are conducted on a Polydimethylsiloxane (PDMS) with a mechanophore spiropyran embedded homogeneously in the bulk of the polymer. The fluorescence data captured in the tests is correlated with the numerically obtained continuum mechanics stress/strain quantities. These correlations will be useful in giving directions towards research in the fundamental understanding of the mechanics of mechanophores, thereby bridging the gap between chemistry and mechanics of mechanosensors. This will pave the way towards optical-only in-situ measurements of stress-strain behavior.

Contents

Acknowledgements i

Abstract ii

1 Introduction 1
- 1.1 Methods for stress mapping 2
  - 1.1.1 Analytical methods 3
  - 1.1.2 Numerical methods 3
  - 1.1.3 Experimental methods 3
- 1.2 Motivation 4
- 1.3 Thesis outline 4

2 Literature preliminaries 6
- 2.1 Photoelasticity 6
  - 2.1.1 Concept of birefringence 7
  - 2.1.2 Stress-induced birefringence 8
  - 2.1.3 Stress-optic law 9
  - 2.1.4 Photoelasticity for detecting stress concentrations 10
- 2.2 Mechanosensing 11
  - 2.2.1 Mechanics of mechanophores 12
  - 2.2.2 Chemistry of spiropyran 13
  - 2.2.3 Factors influencing mechanophore activation in bulk systems 14
- 2.3 Visualization of stress concentrations using mechanosensing 15
  - 2.3.1 Visualization of stress concentrations at the macro-scale 16
  - 2.3.2 Visualization of stress concentrations at the micro-scale 17
- 2.4 Attempts at quantitative stress mapping in mechanosensing 18
  - 2.4.1 Gossweiler et al. (2014) 19
  - 2.4.2 Celestine et al. (2019) 19
  - 2.4.3 Chen et al. (2020) 20
  - 2.4.4 Gohl et al. (2023) 21
- 2.5 Literature conclusions 22

3 Research methodology 24
- 3.1 Research objectives 24
- 3.2 Thesis overview 25
  - 3.2.1 Experimental methodology 25
  - 3.2.2 Simulation methodology 28
  - 3.2.3 Correlation methodology 30

4 Fluorescence measurements of mechanically-induced spiropyran activation 32
- 4.1 Ruling out ”Photoelasticity due to elasticity” 33
- 4.2 Ruling out ”Photoelasticity due to viscoelasticity” 33
- 4.3 Spatial distribution of fluorescence 34
- 4.4 Activation duration of spiropyran under stress 34

5 Correlating mechanics with spiropyran fluorescence 36
- 5.1 Analysis along radial lines 36
  - 5.1.1 Analysis of fluorescence and von Mises stress along radial lines 36
  - 5.1.2 Analysis of decay rate time constant and von Mises stress along radial lines 38
- 5.2 Correlation heatmaps 39
  - 5.2.1 Correlation between fluorescence and simulated quantites 40

5.2.2 Correlation between decay rate time constant and simulated quantities 41

6 Conclusions 42

7 Recommendations 43
7.1 Possible improvements 43
7.1.1 Sample slippage during experiments 43
7.1.2 Light scattering at the edge of the hole 43
7.1.3 Shadow formation 44
7.1.4 Enhancing material model accuracy 44
7.1.5 Reducing the variance in the decay rate time constant image 44
7.2 Future extensions to the current study 44
7.2.1 Future areas of application and impact 45

References 46

A Appendix A - Experimental setup and support software 49
A.1 Linear stage 49
A.2 Peripherals and stage motion 49
A.3 Load cell and force data acquisition 50
A.3.1 Data acquisition LabVIEW project 50
A.4 Image processing software 52
A.5 Mold design for sample curing 54
A.6 Sample preparation procedure 55

B Appendix B - Experimental setup validation and error calculation 56
B.1 Visual inspection 56
B.2 Repeatability 58
B.3 Validation with reference Universal Testing Machine 58
B.3.1 Backlash 59
B.3.2 Force-strain curve comparison 59
B.4 Accounting for stress relaxation of the setup 59

C Appendix C - Simulation framework 60
C.1 Strain data acquisition during tensile test 60
C.2 Parametric fitting for material model selection 61
C.3 Numerical simulation 62
C.3.1 Mesh refinement convergence study. 62

D Appendix D - Correlation data 65

1

Introduction

Modern society is built on the pillars of a vast array of technologies. From the most basic tools such as hammers to complex devices like smartphones and their intricately designed internal components, all have a limited functional capacity. This can be expressed as the product's lifespan or its maximum load-bearing capacity. When subjected to loads which exceed this capacity, they may lose their load-carrying capability, break or malfunction. In engineering disciplines, such occurrences are commonly denoted as ”failure”.

Every manufactured product goes through a design process, which determines its functionalities, and ergonomics and, more importantly, anticipates and accounts for its vulnerabilities. This foresight is important for understanding the product's weakness before operational use. For example, before a ship sets sail, a building is constructed, or a gearbox is activated, knowing its failure methods and weak points will help prevent catastrophic events, loss of resources wasted in building the structure, and the potential for human casualties.

Failure typically involves initiating and propagating a macroscopic crack, ultimately leading to structural failure. The World War II era Liberty ships' failure is well-known and dramatic. Three of the early ships, similar to the Liberty S.S. Schenectady as depicted in Fig. 1.1 (a), split in half as soon as they were let into the water due to cracks that grew beyond a critical length in the hull and decks of the ships [1]. Fig. 1.1 (b) shows a critical failure of an oil tanker with a brittle fracture along the midline of its length due to the propagation of a crack through its entire circumference. The fracture likely originated from a slight notch. As the tanker was buffeted about while at sea, resulting stresses around the notch amplified due to the tanker's weight and external forces from waves, such that the crack rapidly grew and eventually

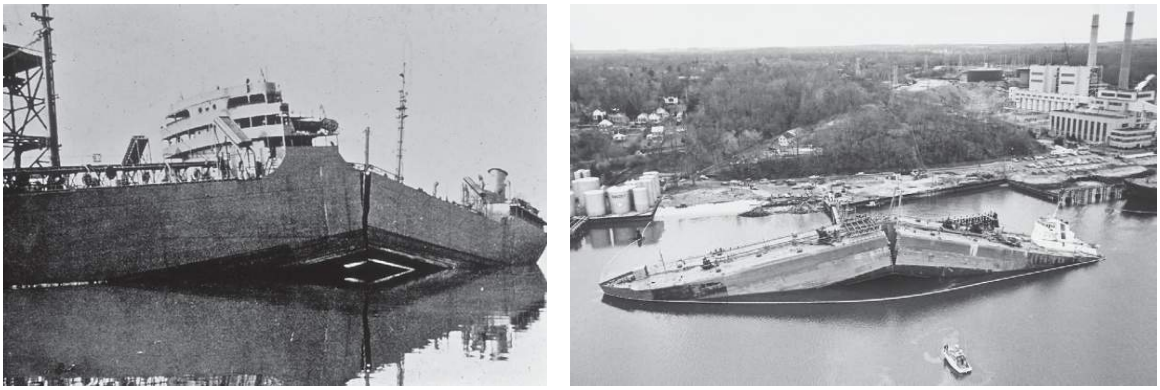
(a) (b)

Figure 1.1: (a) The Liberty ship S.S. Schenectady, which, in 1943, failed before leaving the shipyard, (b) An oil tanker split in half due to a brittle crack propagation; Image adapted from ref. [1].

led to material failure [1].

The first commercial jetliner, ”de Havilland 106 Comet,” in 1953, experienced another such disaster (Fig. 1.2 (a)). To take full advantage of the jet engine, the Comet flew at an altitude of 35000 ft, much higher than the propeller planes of the time. The Comet encountered reduced drag and lower turbulence, making it faster, more fuel-efficient, and much more comfortable for the passengers. To achieve this, the jet’s cabin had to be pressurized from the inside. Pressurized cabins were new and poorly understood at the time. After one year in service, three Comet airplanes had broken down mid-air. When the carcass was examined, the engineers found a design flaw in the square windows being subjected to multiple load cycles [2]. The square windows acted as a focal point for the stress, particularly during the high altitude flights when the cabin pressure was significantly higher than the outside air pressure. The stress concentration was much higher near the window’s edges and corners. These acted as crack initiation points [3]. Over time, with repeated pressurization and depressurization, the cracks propagated until they reached a critical length. Ultimately, the structure of the plane broke down due to metal fatigue, which resulted in a blast in mid-air. The disaster was followed by re-designs that replaced square windows with oval ones (Fig. 1.2 (b)), which allowed an even stress distribution and improved the structural reliability drastically.

To avoid such catastrophic events, a proactive approach is necessary. This approach involves accurate estimation of the stress distribution within structures before the design phase. Mapping stresses in continuous bodies was studied extensively in the literature, and various techniques were developed over the past decades.

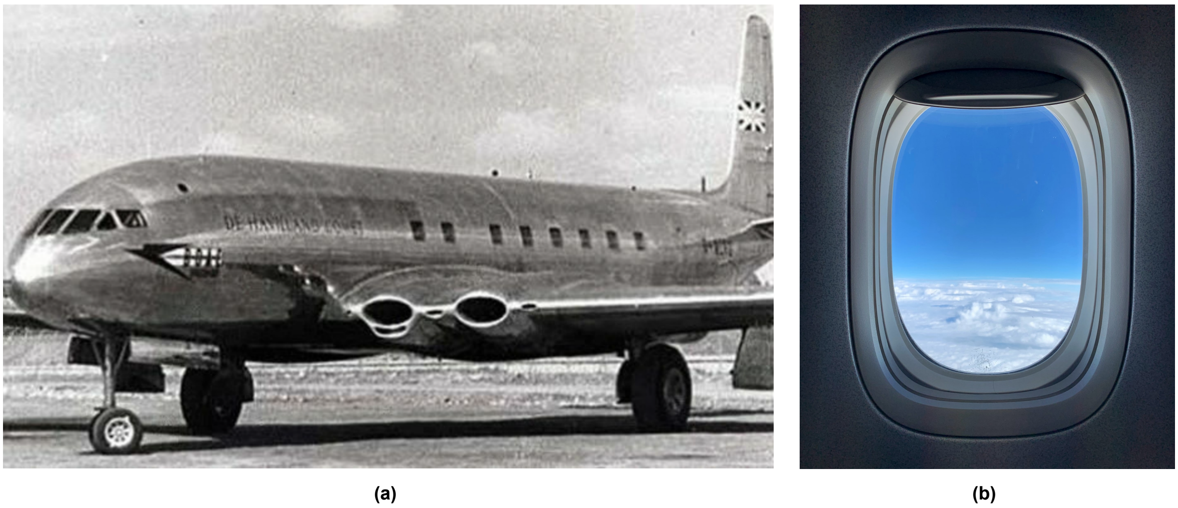
(a) (b)

Figure 1.2: (a) De Havilland DH 106 Comet (1954) with its square windows in focus; Image adapted from ref. [3], (b) Redesigned oval windows for modern aircraft; Image adapted from ref. [4].

1.1. Methods for stress mapping

The failure of materials under stress is an intricate phenomenon influenced not only by external forces but also by the structural geometry of the object under consideration. Studying the effect of loading is important to understand the strength of materials. Complimentarily, the role of geometry, particularly stress concentrations and surface roughness, is equally important as these factors can cause the material to fail instantly.

To address these challenges, researchers proposed so-called stress mapping techniques, which allow for the visualization and quantification of stress distribution within a material. In practical product development, a combination of analytical mathematical modeling, computational simulations, and experimental methods is commonly utilized to predict and accommodate for stresses in the structure. In this section, a few important and widely used stress mapping methods will be discussed that are broadly characterized into three sections:

1.1.1. Analytical methods

Analytical techniques are among the earliest methods developed for stress analysis. They are based on the use of equations and principles from mechanics and materials science to predict stress patterns. They are very effective for simple geometries and loading conditions. Analytical methods attempt to solve the governing equations in their strong form to calculate the stress distributions accurately.

Analytical methods serve as a foundation for the understanding of stress concentrations and potential points of failure in a structure, upon which, the more complex and computationally more intensive numerical methods are built. They serve as a benchmark for validating experimental and computational methods.

In a continuum mechanics framework, several analytical models were formed to accurately predict the distribution of stresses and strains for different loading conditions and underlying geometries. The Eshelby model aids in the understanding of material behavior in cases of defects and inhomogeneities. Hence, it is used to model and predict the responses of many composite materials. Additionally, Airy's Stress Function represents another analytical approach that can be used to simplify two-dimensional elasticity problems.

1.1.2. Numerical methods

While analytical techniques provide precise and exact solutions under simplified conditions and simple geometries, numerical techniques are widely used to obtain approximate solutions for complex geometries and loading scenarios where exact solutions are impossible to obtain analytically. The three most widely used numerical methods are the Finite Element Method (FEM), Finite Volume Method (FVM) and the Finite Difference Method (FDM). FEM is most commonly used in computational solid mechanics, whereas FVM is preferred in computational fluid dynamics. Fig. 1.3 shows the von Mises stress distribution around a square window, highlighting the area of high-stress concentration at the corner.

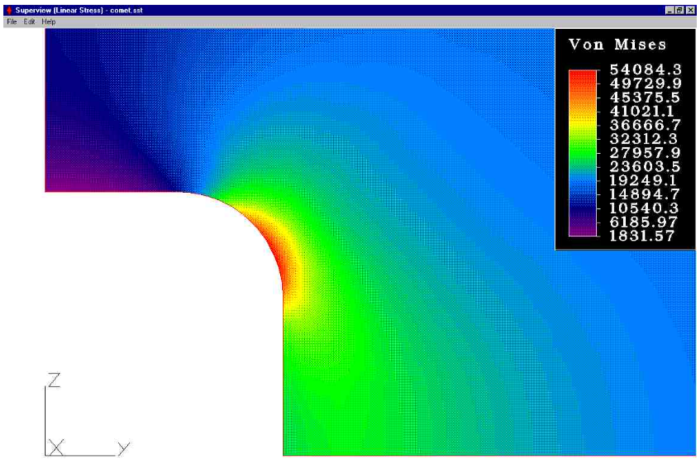

Figure 1.3: Finite element simulation to visualize corner stresses of a curved aircraft window. The regions of highest stresses are denoted by the red color; Image adapted from ref. [5].

The Finite Element Method discretizes the geometry of the structure and the displacement field on a mesh comprised of a finite number of elements. The governing differential equations are then solved for at the nodes of the mesh, and interpolated in between elements. Stresses and strains can then be postprocessed from the derived displacement field and similarly interpolated over elements, to provide a comprehensive stress map over the structure.

1.1.3. Experimental methods

Experimental methods are essential for verifying the results obtained from analytical and numerical analysis. These methods are particularly crucial because certain features can neither accurately be modeled analytically nor numerically. Such features include hysteresis effects caused by friction, surface roughness, shape irregularities, and manufacturing defects.

Some of the crucial experimental methods for stress mapping from the state-of-the-art are listed as follows:

1. **Optical methods:**
   Optical stress analysis methods comprise a variety of techniques that use light to evaluate the stress distribution within a material. These methods depend on the interaction of light with the material properties that change under stress, such as refractive index, birefringence, or reflectivity. Photoelasticity is the most common among the optical methods for stress sensing, which creates stress field images using changes in birefringence. Mechanosensing, which combines optics with chemistry, is another growing approach in this field. At the micro-scale, techniques like Confocal Raman Microscopy and Laser Speckle Interferometry are also widely used [6].

2. **X-ray diffraction:**
   X-ray diffraction (XRD) is an experimental technique used for analyzing the crystalline structure of materials. By directing X-rays toward a sample and detecting the angles and intensities of the diffracted beams, XRD allows for the determination of a crystal's lattice parameters and the spacing between lattice planes. This non-destructive method provides details into the structural arrangement of atoms, identification of phases, and detection of stress and strain in crystalline materials. The spatial resolution of X-ray diffraction is around 10 nm [7].

3. **Thermoelastic stress analysis:**
   Thermoelastic Stress Analysis (TSA) is a non-contact, non-destructive experimental technique used to measure the small temperature changes when materials are subjected to cyclic loading. These temperature changes are related to the stress changes in the material through the thermoelastic effect. Under adiabatic conditions, where no heat is allowed to leave the sample, temperature variations in a solid body are directly proportional to the changes in the sum of principal stresses [8]. TSA uses sensitive infrared detectors to capture the minute temperature variations that are indicative of the stress state of the material. However, the spatial resolution of TSA is limited by the pixel size of the infrared camera, which is in the order of $\mu\mathrm{m}$ [8].

1.2. Motivation

As highlighted earlier in Section 1.1, material failure is affected not only by applied loading but also by the structural geometry, such as notches and surface roughness, which act as crack initiation points. Additionally, manufacturing processes can add defects and residual stresses to the structure, which are impossible to predict and thus model analytically or numerically. To visualize stress distributions at the macro-scale, two prominent techniques - photoelasticity and mechanosensing are most widely used.

Photoelasticity has been prevalent in the industry since the 1960s. The Stress-Optic Law of Photoelasticity allows for direct visualization of stress fields by analyzing the birefringence fringe patterns. On the other hand, mechanosensing is a growing technology with high potential in stress mapping. While researchers have demonstrated the various capabilities of the mechanosensing method qualitatively, there is a significant gap in linking the fluorescence observed in mechanosensing to the local stresses experienced by the material. This thesis aims to bridge the gap by exploring the quantitative relationship between fluorescence and stress in mechanosensing from a phenomenological perspective.

1.3. Thesis outline

The current chapter, Chapter 1, outlines a brief classification of Stress Mapping techniques, presents the motivation for the research, and identifies the research gap. The remaining part of the thesis report is structured as follows:

- Chapter 2 provides a brief introduction to the background concepts needed for understanding this research. It provides a comprehensive literature overview of photoelasticity and mechanosensing stress mapping techniques.

- Chapter 3 outlines the research questions to be answered and the objectives for the thesis. It presents the methodology followed for the experimental, simulation, and correlation phases of the research.
- Chapter 4 provides insights and in-depth discussions on the fluorescence measurements and the observations of the control experiments.
- Chapter 5 covers the outcomes of the correlation between the fluorescence and the continuum mechanics quantities.
- Chapter 6 summarizes the outcomes of the research.
- Chapter 7 gives recommendations for improvements in the present work to make it more refined and detailed, along with a discussion on potential future work that could extend and build upon this research.

2

Literature preliminaries

This chapter provides a comprehensive overview of the fundamental concepts required to understand the research work done in the following chapters. The basic concepts and applications of photoelasticity are explained followed by those for mechanosensing. Lastly, a literature overview of the attempts to quantify stresses using the mechanosensing technique is provided.

2.1. Photoelasticity

Photoelasticity is one of the primary and earliest experimental techniques to analyze the stress and strain fields within the material. It remains one of the most widely used methods in industry, capable of providing the stress field of the entire cross-section in a single experiment. One of the earliest descriptions of the technique was given by Coker and Filon in 1932 [9].

In 1932, Oppel introduced the concept of frozen stress photoelasticity, which allowed three-dimensional stress field analysis [10, 11]. The method involves making a model of the component from a thermosetting polymer, typically an epoxy resin. The model is loaded to its stressed state and heated above a certain temperature, referred to as the stress-freezing temperature of the polymer. The model is thermally soaked for some time, slowly cooled to room temperature, and then unloaded. The strain and birefringence induced due to the loading do not vanish even when the model is cooled. This process is known as stress freezing. The stress-frozen model is then sliced either mechanically or optically to reveal the stress distribution in the cross-section.

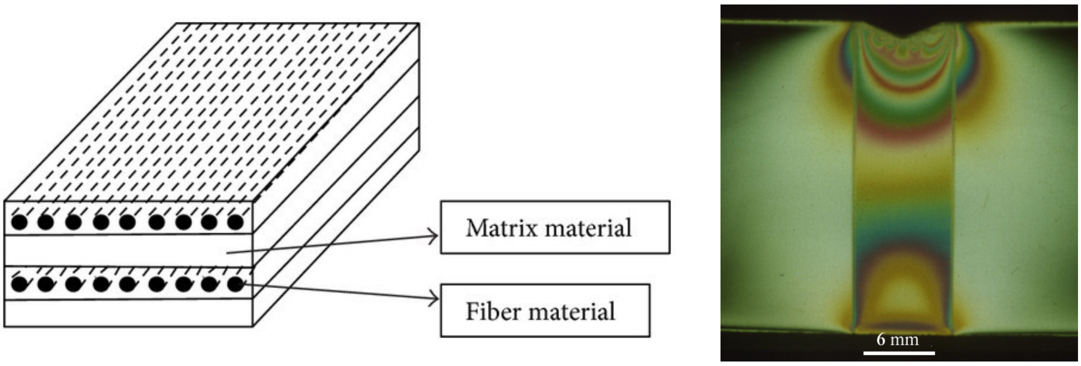

(a)

(b)

Figure 2.1: (a) Schematic diagram of a composite material with fiber and matrix; Image adapted from ref. [12], (b) Frozen stress photoelastic fringe pattern of a composite material's fiber-matrix interface cross-section; Image adapted from ref. [13].

In the structural composition of composite materials, fibers are embedded into a matrix that lead to improved structural properties along the fiber's axial direction. Fig. 2.1 (b) shows an optical image of a sliced photoelastic model of a fiber-matrix interface being debonded in a composite material [13]. The fringe pattern qualitatively suggests high-stress concentrations at the interface's four corners due to shear stresses, which can be inferred by the higher concentration of the fringes near the corners of the fiber-matrix interface.

Since photoelasticity relies on optical phenomena, the following sections introduce the fundamentals of the optical method and guide the reader from the basic properties of polarized light to the manifestations of its interaction with materials under stress.

2.1.1. Concept of birefringence

According to Maxwell's electromagnetic theory, light is comprised of two perpendicular vector fields - an electric field (E) and a magnetic field (B) (Fig. 2.2 (a)). Most light sources have many molecular light emitters producing light in randomly oriented directions. If the geometrical oscillations of the light are made to follow a specific law, the light is called polarized light [10]. The most common types of polarized light are i) plane polarized light, ii) circularly polarized light, and iii) elliptically polarized light (Fig. 2.2 (b)).

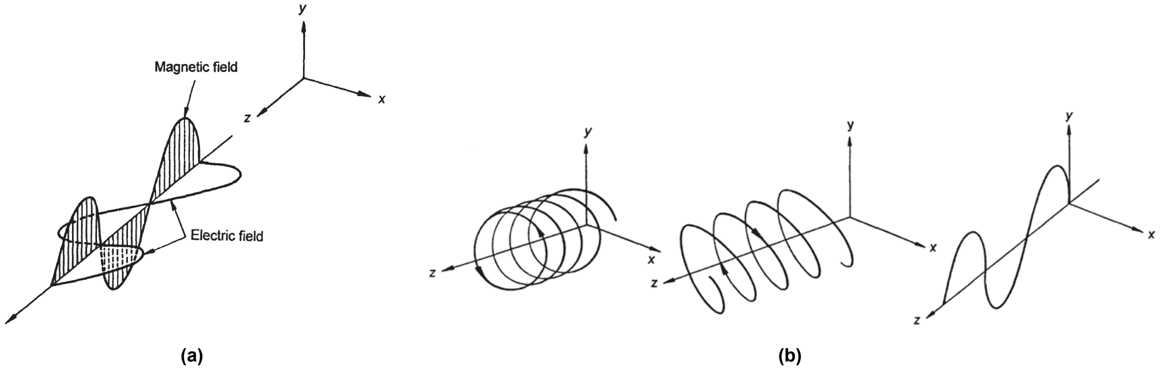

Figure 2.2: (a) Light constituted of the electric and magnetic field, (b) Circularly, elliptically, and linearly polarized light; Image adapted from ref. [10].

The physical laws that govern the passage of light through isotropic materials are well known as Snell's Laws (Fig. 2.3 (a)). In essence, the Snell's Laws consist of two laws:

1. The normal to the incident ray, the normal to the interface, and the normal of the refracted ray lie in the same plane.
2. The ratio of the sine of the angle of incidence and the sine of the angle of refraction is constant and is known as the "relative refractive index." Thus, if c is the velocity of light in vacuum, then it holds:

$$\frac{\sin i}{\sin r} = \frac{v_1}{v_2} = n_{12}, \text{ with } n_1 = \frac{c}{v_1}, \text{ and } n_2 = \frac{c}{v_2}. \tag{2.1}$$

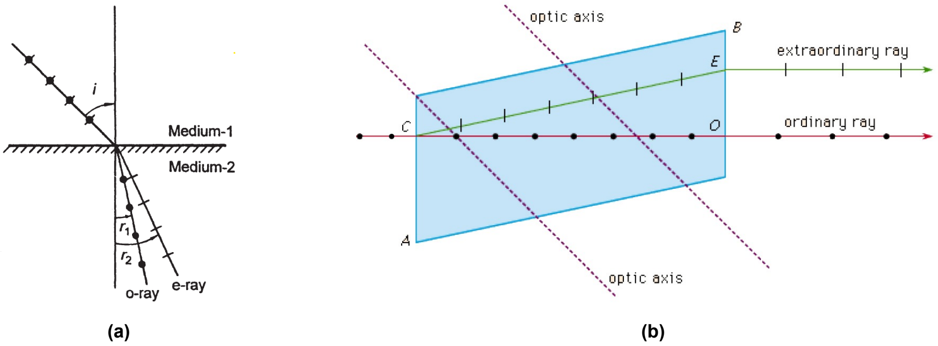

Figure 2.3: (a) Refraction of light when passing from air to water; Image adapted from ref. [10], (b) Double refraction of light in calcite; Image adapted from ref. [14].

When light passes through a crystalline material, a single incident ray splits into two refracted rays - i) Ordinary ray (o) and ii) extraordinary ray (e). This phenomenon is known as ”Double Refraction” (Fig. 2.3 (b)). The extraordinary ray (e) is called likewise because it manages to disobey the Snell’s Laws. The ’e’ ray need not be confined to the plane of incidence. Additionally, the ’e’ ray experiences a different refractive index, and thus the velocity of the ’e’ ray changes depending on the angle of incidence.

The photoelastic effect is observed when the incident light is perpendicular to the optic axis of the crystal. The principal stress directions act as polarizing axes at any point of interest. In this orientation, the ’o’ ray and the ’e’ ray travel in the same direction; but the ’e’ ray travels faster than the ’o’ ray due to its lower refractive index. When the rays emerge out of the crystal, there exists a relative retardation between the rays. (Fig. 2.4). When the emerging light is passed through a polarizer, the rays align on a particular plane and we see constructive and destructive interference. This leads to the formation of fringes. The following section explains the mathematical formulation of the relation between the fringes and the stress in the material for polymers.

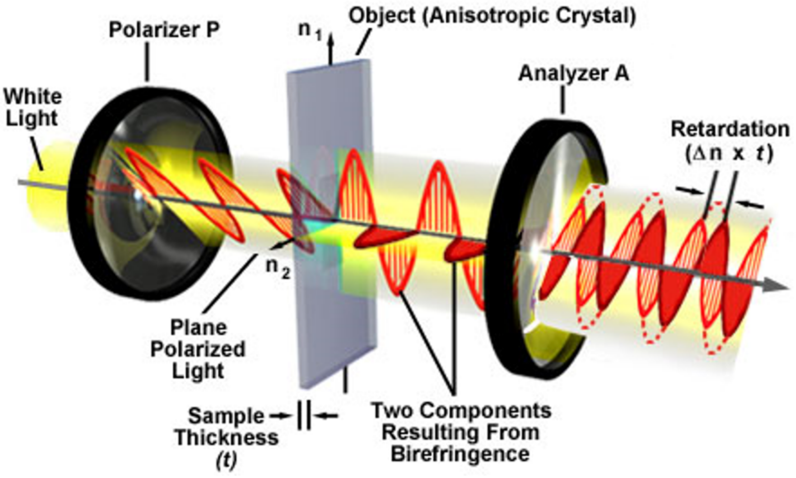

Figure 2.4: Birefringence mechanism in an anisotropic crystal; Image adapted from ref. [15].

2.1.2. Stress-induced birefringence

Under pressure or tension, the refractive index of transparent isotropic media changes, exhibiting optical anisotropy. If the stress within the transparent material is non-uniform, then the birefringence is also non-uniform across the material. Thus, light rays passing through different points in the material accumulate different phase differences. By analyzing these differences, it is possible to analyze the stress distribution within mechanical structures.

2.1.3. Stress-optic law

The Stress-Optic Law aids in mathematically quantifying the stress in the material based on optical measurements. In this section, we delve into the mathematical formulation of the Stress-Optic Law.

Retardation through a crystalline medium

Consider a crystalline plate of thickness h. Let a plane polarized light be incident on it as shown in Fig. 2.5 (a). Let the principal stress components, and thus the polarizing axes of the plate, be aligned at angles θ and $\theta + \pi/2$ with the horizontal. Let the light be incident to the optic axis of the crystal.

Since the light is perpendicular to the optic axis, the wave splits into 2 refracted waves - an 'o' wave and an 'e' wave; traveling in the same direction but at different velocities v_1 and v_2. Thus, these two waves have a net phase difference of δ when they emerge from the crystal. Note that the two perpendicular waves shown in Fig.2.5 (b) are the ordinary (o) and the extraordinary (e) waves and must not be confused with the electric and magnetic components of light.

Since the velocities of propagation of the two waves are different, they take different times, h/v_1 and h/v_2 seconds, respectively, to pass through the crystal of thickness h. If the frequency of light is f, the phase difference δ is given as:

$$\begin{aligned} \delta &= 2\pi f\left(\frac{h}{v_1}-\frac{h}{v_2}\right) = 2\pi h\frac{c}{\lambda}\left(\frac{1}{v_1}-\frac{1}{v_2}\right), \\ \delta &= \frac{2\pi h}{\lambda}(n_1-n_2). \end{aligned} \tag{2.2}$$

where n_1 and n_2 are the refractive indices experienced by the ordinary and extraordinary waves. The phase difference δ is also known as the "relative retardation" between the waves.

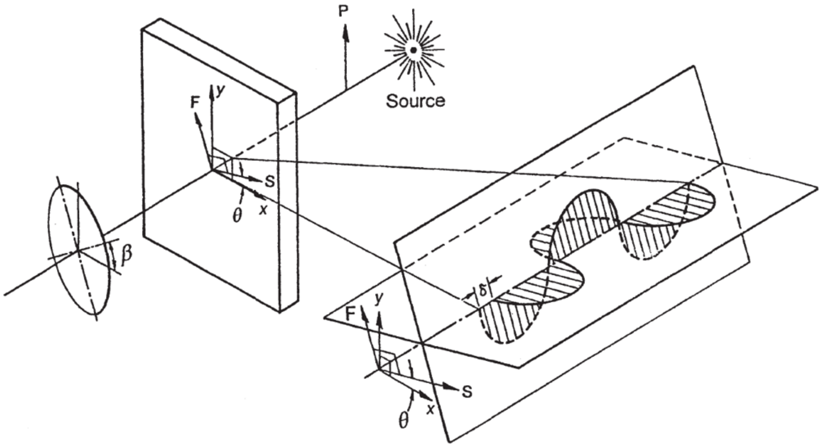

Figure 2.5: Linearly polarized light inside an anisotropic crystal incident perpendicular to the optic axis. Inside the crystal, two plane-polarized lights, whose planes of polarization coincide with the fast and slow axes, travel with different velocities; Image adapted from ref. [10].

Stress-optic relation for transparent polymers

Consider a transparent polymer model under a plane state of stress. The state of stress at a given point can be displayed through the two principal stress directions σ_1 and σ_2. It is known that when stressed, the model becomes doubly refractive. Also, the direction of polarization axes at a given point coincides with the principal stress directions. Let n_1 and n_2 be the refractive indices at the given point in the two principal stress directions. In 1852, Maxwell formulated the relations between stress components and the index of refraction:

$$\begin{aligned} n_1 - n &= c_1\sigma_1 - c_2\sigma_2, \\ n_2 - n &= c_1\sigma_2 - c_2\sigma_1. \end{aligned} \tag{2.3}$$

where c_1 is termed the direct stress-optic coefficient and c_2 is the transverse direct-optic coefficient.

If a plane polarized light is incident on the model, then the relative retardation δ can be expressed in terms of the refractive indices as shown in Eq. (2.2). Substituting Eq. (2.2) into Eq. (2.3), we get

$$\delta = \frac{2\pi h}{\lambda}(c_1 + c_2)(\sigma_1 - \sigma_2), \tag{2.4}$$

$c_1 + c_2$ can be replaced by C to get the relative retardation as

$$\delta = \frac{2\pi hC}{\lambda}(\sigma_1 - \sigma_2), \tag{2.5}$$

which can be rewritten in terms of fringe order N as

$$N = \frac{\delta}{2\pi} = \frac{hC}{\lambda}(\sigma_1 - \sigma_2), \tag{2.6}$$

C is known as the relative stress-optic coefficient, which is assumed to be constant for a material. Studies have found that C depends on the wavelength and the material [16]. Eq. (2.6) can be rearranged as follows:

$$\sigma_1 - \sigma_2 = \frac{NF_\sigma}{h}. \tag{2.7}$$

where $F_\sigma = \frac{\lambda}{C}$ which is known as the material stress fringe value. Eq. (2.7) is famously known as the Stress-Optic Law as it relates the stress information to optical measurements. The Stress-Optic Law shows that $(\sigma_1 - \sigma_2)$ and F_σ are linearly related for a certain wavelength λ, but at higher stress values, the relation becomes non-linear and Eq. (2.7) cannot be used.

2.1.4. Photoelasticity for detecting stress concentrations

The discovery of the Stress-Optic Law accelerated the use of photoelasticity across industries. With the advent of Digital Image Processing, visualizing the stress field from birefringence data became faster [10]. As discussed earlier, photoelasticity has a spatial resolution of around 300 nm. In practice, the limit stays about 1000 nm, or 1 $\mu\mathrm{m}$. In order to sense the stress for even smaller spatial resolutions, photoelasticity can be combined with other experimental techniques [17].

Photoelasticity has been used for visualizing stress concentrations in various applications. A couple of them have been explained in this section:

1. **Stress field around sharp notches:**
    - A V-notched Brazilian disk with different angled V-notches is prepared to experimentally obtain the notch stress intensity factors using photoelasticity.
    - A high concentration of fringe lines can be observed near the notch edges. The number of lines increases with the sharpness of the notch.

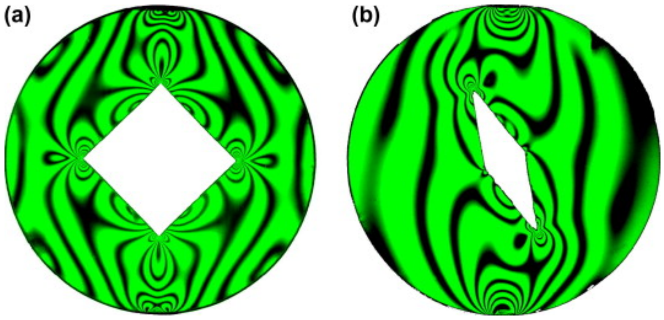

Figure 2.6: The monochromatic fringe patterns of the notched sample; Image adapted from ref. [18].

2. **Stress patterns and defects in bonded silicon wafers:**
    - Photoelasticity, coupled with a near IR transmission system, is deployed to get a 1 μm spatial resolution.
    - Defects/cracks of submicrometer dimensions are difficult to trace optically, but their stress fields are at least an order of magnitude larger.
    - By measuring the transmitted infrared light intensity field, the crack is more apparent because of the birefringence patterns from the stress fields around the crack.

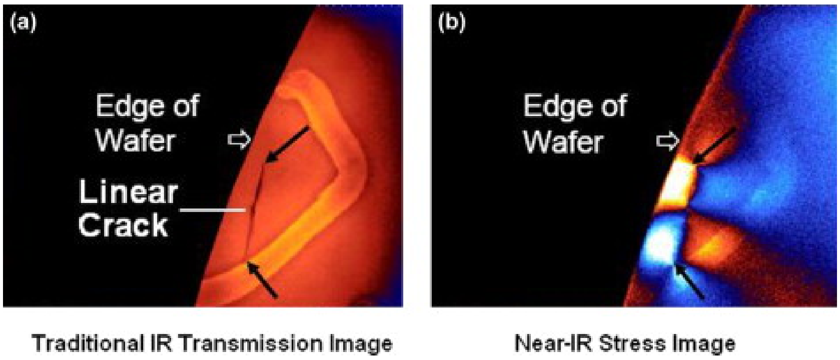

Figure 2.7: Near-infrared stress imaging of fracture in silicon wafers. (a) Traditional IR transmission image visible from one side only, (b) Near-IR stress image reveals the stress patterns in the vicinity of the crack; Image adapted from ref. [17].

As we transition from the topic of photoelasticity to the emergent field of mechanosensing, we carry forward the understanding that both methodologies are optical techniques capable of mapping stress in materials. Fundamentally, both techniques are constrained by the same optical limitation - the resolution of detail they can capture depends on the wavelength of light used. This means they can theoretically resolve details as small as 300 nm. The next chapter comprehensively explains the mechanics of mechanosensing and provides a deeper summary of the existing literature.

2.2. Mechanosensing

Mechanochemistry provides an alternative chemistry-based approach for stress mapping in the nanoscopic, micro-scale, and macroscopic scales using optics, famously known as ”Mechanosensing”. Mechanosensing has been made possible due to strides in the research of mechanoresponsive materials. These smart materials have the ability to adapt their material properties in response to external stimuli. These materials are engineered to reversibly respond to mechanical, optical, temperature changes and other stimuli by changing their shape, viscosity, and color [19].

The innovation and development of mechanophores and force-sensitive chemical groups lie at the heart of these smart material advancements. Generally, mechanophores are embedded into a polymer matrix and are covalently bonded to it. Mechanophores undergo a chemical reaction on the application of load and generally respond with a change in color (mechanochromic response) or by becoming fluorescent [20].

Mechanosensing is an emerging field for stress analysis, which is capable of mapping stresses in the material across scales from macro-scale phenomena like necking, to micro-scale phenomena like cracks, down to the nano-scale events like individual bond scission. The potential for mechanosensing to evolve into a technique for real-time visual monitoring is particularly promising for stress detection in dynamic settings where continuous and immediate feedback is crucial. [21, 22].

This section starts with an introduction to the mechanics of mechanophores, followed by an in-depth look at the chemistry of spiropyran, the specific molecule at focus in this research. Subsequently, various stress visualization attempts at the micro- and macro-scale are reviewed. This follows an analysis of four relevant studies in the literature that have attempted to quantify the stresses using optical measurements. The section ends by summarizing the literature contributions, providing a foundation of background knowledge for the following research methodology Chapter 3.

2.2.1. Mechanics of mechanophores

Mechanophores are small force-sensitive molecules that respond chemically to mechanical stresses. Common chemical responses are bond scission or molecular rearrangement, leading to changes such as light emission (mechanoluminescence), color change (mechanochromic), or change in mechanical properties such as softening or toughening (mechanocatalytic response).

By incorporating mechanophores such as spirolactam, spiropyran, benzocyclobutane [23] or anthracene [24] into material systems, real-time stress distribution can be observed through a visual response. This capability is ideal for damage and failure sensing applications [25]. Mechanophores can be used in a variety of applications like flexible electronics [26], sensors [27], additive manufacturing [28], and structures like bridges or windmill blades that require continuous health monitoring due to cyclic loading. To fully understand the optical response of these smart materials, the underlying molecular phenomenon of these force-sensitive mechanophores needs to be understood.

Smart mechanosensing materials are engineered by embedding mechanophore molecules into stable polymer matrices like Polydimethylsiloxane (PDMS) and Polymethyl methacrylate (PMMA). The mechanophores are joined with the host material through strong covalent bonds or reversible weaker bonds such as hydrogen bonds [29] or Diels-Alder adducts [30]. The application of force triggers a chemical reaction in mechanophores that result in their transformation from a non-active state to a fluorescent active state. This process is simply termed as ”Activation” [20]. This activation can occur in two types of reversible chemical reactions based on the bonds that are affected due to the loading:

1. **Chemical reaction between the mechanophore and the matrix:**
   The interaction between mechanophores and the host material follows either cross-linking of polymer chains or polymerization. This has an effect on the mechanical properties of the bulk material, which is usually seen as softening or hardening of the polymer.

2. **Chemical reaction within the mechanophore:**
   When a chemical reaction is induced within the mechanophore, typically, a chemical bond breaks or an isomeric rearrangement occurs.

   (a) **Bond scission**:
   Bond scission occurs when a weak bond within the mechanophore, like a labile bond (a weak metal-ligand bond) or a strained ring in the molecular architecture, breaks, which eventually breaks the mechanophore into two molecules. The dioxetane mechanophore in Fig. 2.8 demonstrates a bond scission reaction due to a strained O-O ring, producing fluorescent molecules.

   (b) **Isomerization**:
   In isomerization, a molecule rearranges to a different configuration, keeping the same molecular formula. This process does not involve a change in the number or type of atoms in the molecule but rather involves a rearrangement of these atoms. For instance, under stress, the mechanocatalytic molecule shown in Fig. 2.8 undergoes a spatial reconfiguration where the hanging double bonds make a ring pushing the cyclopentane ring out-of-plane of the molecule.

   Inversely, spiropyran undergoes isomerization by breaking a cyclic ring containing a weak $C_{spiro} - O$ bond [31]. This helps lengthen the molecule to the new distinctly purple-colored merocyanine form. The removal of force reversibly returns the molecule to the shortened spiropyran form.

Spiropyran has been immensely researched and understood from various perspectives, such as internal changes of isomerization and reaction kinetics. The next subsection delves into the molecular chemistry and kinetics of the mechanophore response of spiropyran.

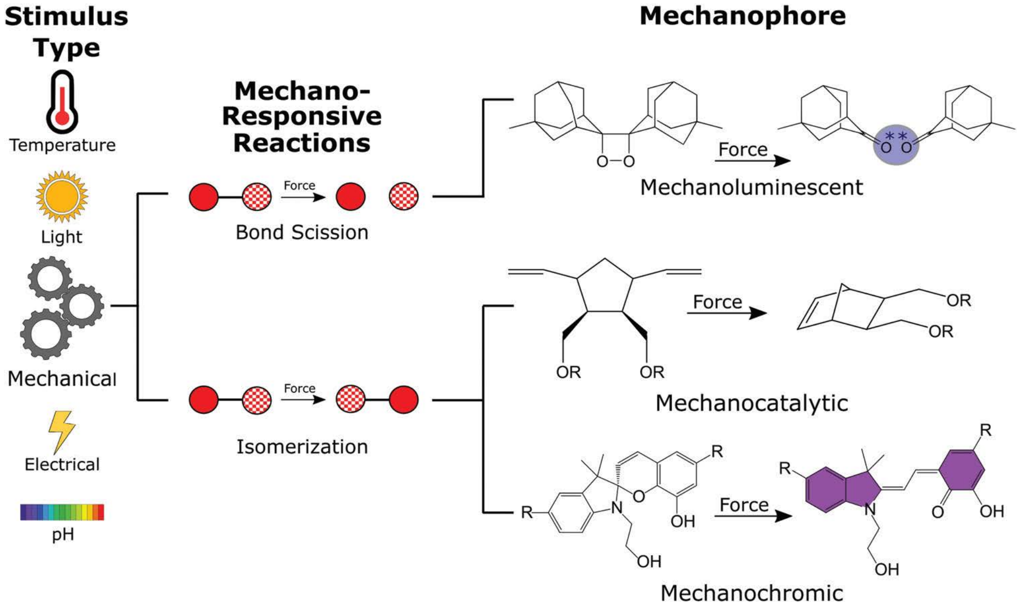

Figure 2.8: Mechanophore classification and nomenclature; Image adapted from ref. [20].

2.2.2. Chemistry of spiropyran

Spiropyran is a mechanophore recognized for its potential use as a mechanical probe for stress mapping [32]. When stimuli like heat, light, or mechanical loads are applied, the spiropyran molecule undergoes a 6-π electrocyclic ring-opening reaction which produces a molecule merocyanine, a molecule with a different chromatization. This transition, referred to as SP-MC transition is an isomerization reaction [33]. Spiropyran can be bonded to the polymer matrix through a strong but reactive covalent bond [19].

The spiropyran molecule (Fig. 2.9) has a ring system that can reversibly go through electrocyclic reactions, which refer to both ring-opening and ring-closing reactions. The equilibrium of photochromatic materials like spiropyran is influenced by the polarity of the environment, which is a cumulative of the polarity of the different equilibrium components. In a non-polar polymer unit like PDMS, the short molecule spiropyran is relatively stable since it is less polar. Thus the spiropyran-embedded PDMS is colorless without excitation. When the bulk material is stretched or excited by light or heat, the environment within the material becomes polar, favoring the stability of the polar merocyanine form. This transition shows a distinct purple color in light exposure and a strong fluorescence in a dark environment, as shown in Fig. 2.10 (a) [34].

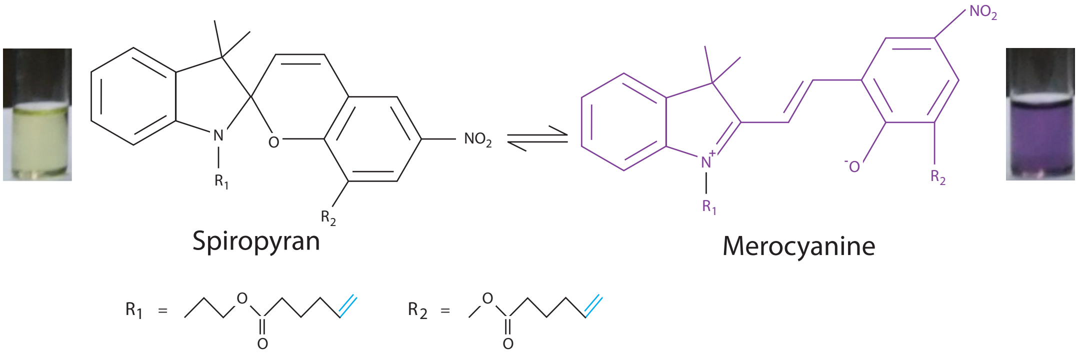

Figure 2.9: Images of pale yellow colored spiropyran-linked polymer and the corresponding activated blue colored polymer containing merocyanine molecules. The vinyl groups attached are highlighted in blue in R_1 and R_2; Image adapted from ref. [35].

Spiropyran-embedded polymer, produced for this thesis, is made as a thermoset elastomer by introducing the cross-links into the polymer at the preparation stage. The cross-linking of the spiropyran with the polymer matrix is ensured by introducing R_1 and R_2, which belong to the vinyl functional groups. The blue groups in R_1 and R_2 are called vinyl groups which are chemically reactive and can undergo polymerization. The Spiropyran component will co-polymerize with the PDMS also containing vinyl groups and become a part of the polymer network. The SP-MC transition reaction is not unidirectional but rather an equilibrium reaction, represented in Fig. 2.9 by a " $\rightleftharpoons$ " symbol. On activation with UV light, the spiropyran molecules in the activation region get converted to merocyanine. Once the UV light is retracted, the merocyanine starts to decay back to its spiropyran form.

The kinetics of the equilibrium have been studied in depth. Kim et al. [34] have studied the SP-MC transition in thermoplastic polyurethanes by measuring the fluorescence change due to activation of the spiropyran mechanophore. They concluded that above a critical stress value, the forward rate constant (spiropyran to merocyanine transition) increases, and the reverse rate constant decreases as we increase the stress (Fig. 2.10 (b)). Calculating the activation energies for both reactions as a function of stress, they found that the applied force lowers the activation energy for the forward reaction but increases the barrier for the reverse reaction. Thus from a kinetics point of view, at higher stresses, the forward reaction is preferred, and the merocyanine form is more stable.

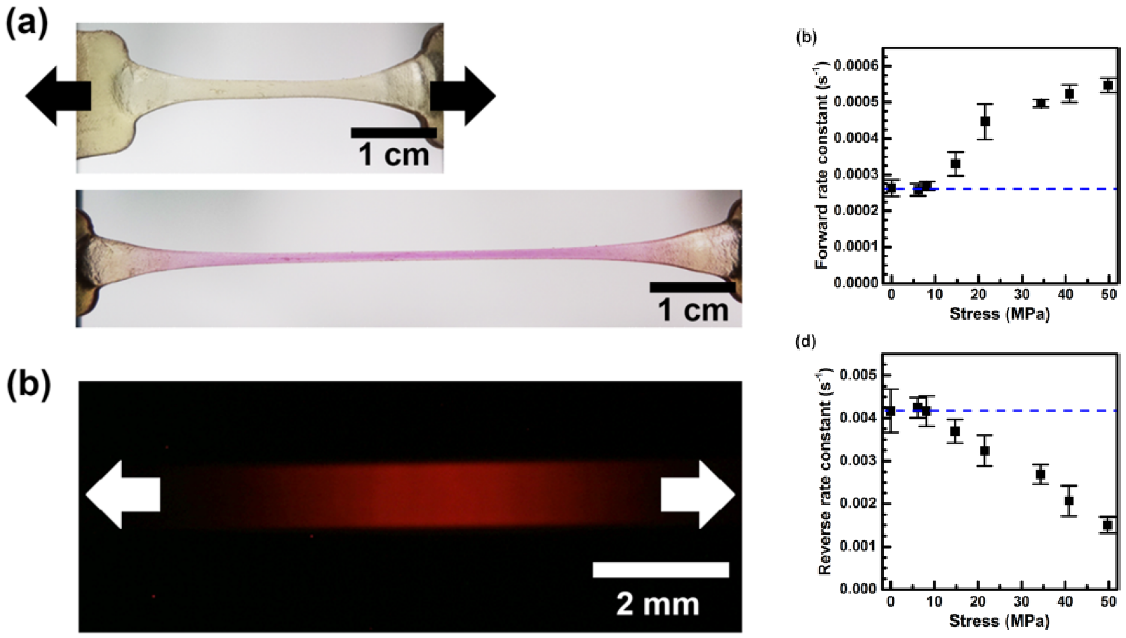

(a) (b)

Figure 2.10: (a) Optical images of spiropyran-linked polymer unit (SP-PU) dog-bone before (top) and after stretching (bottom). Fluorescence images of SP-PU after activation, acquired under dark conditions; Image adapted from ref. [34], (b) Forward rate constant (K_f) and reverse rate constant (K_r) calculated at different applied stress values. Blue dashed lines indicate the initial rate constant; Image adapted from ref. [34].

2.2.3. Factors influencing mechanophore activation in bulk systems

As discussed in Section 2.2.1, the activation of mechanophores requires only 2 conditions to be fulfilled:

1. A weak bond readily available for isomerization.
2. Sufficient force being transmitted to that bond.

However, there are a range of other factors affecting this simple set of conditions. The factors range from internal factors, such as the selection of material (mechanophore and bulk material) and the type of polymerization, to external factors such as the type of loading and the environment. These factors affect the mechanophore's ability to act as a stress sensor. In this section, we will look at the effects of these factors on the activation of mechanophores.

1. **Influence of the polymer matrix on mechanophore activation:**
   In a bulk polymer system, the polymer matrix is responsible for transmitting the applied force to the mechanophore. Polymer viscosity plays a significant role in force transmission.
   - In the case of glassy polymers, the polymer matrix is so brittle that it can reach failure even before activating the mechanophore [36].
   - On the other hand, polymers with low viscosity are readily deformable. This helps them redistribute the stresses very effectively within the matrix, thereby causing very few bond scissions of the mechanophore. This limits the activation and thereby the stress-sensing capability of the material. [37].
2. **Concentration of mechanophores:**
   The concentration of mechanophores in the bulk has a direct effect on the fluorescence. A high concentration of mechanophores means more number of mechanophores in a unit volume, which leads to a stronger fluorescence intensity upon activation [26].
   - A minimum concentration of mechanophores is needed to overcome the sensitivity of the experimental setup being used [34, 21, 38]. Insufficient concentrations could also violate the assumption that the mechanophore is distributed homogeneously throughout the bulk.
   - Moreover, mechanophore concentration also affects the mechanical properties, such as viscoelastic properties of the polymer [20, 38].
3. **Incorporation of mechanophore into matrix:**
   The technique used to embed mechanophores within the polymer matrix has a significant effect on their ability to report stress.
   - While stress is applied through sonication, sound waves majorly hit the center of the sample. An effective activation can be achieved by having a high concentration of mechanophores in the center.
   - Mechanophores embedded into crosslinked polymers show homogeneous activation throughout the bulk compared to those in linear polymers. Since the polymerization of cross-linked polymers leads to a random orientation of the mechanophores, the activation is also random and thus homogeneous, independent of the loading directions [39, 40].
4. **Environmental factors:**
   Environmental factors such as temperature, humidity, exposure to gases, and UV irradiation can limit the application of mechanophores. For example, UV irradiation limits the use of mechanophores as stress sensors for applications in the presence of sunlight. Mechanophores have a thermal stability temperature above which they do not activate [41, 37].

2.3. Visualization of stress concentrations using mechanosensing

In the past decade, fundamental studies of mechanophores have significantly advanced our understanding of the kinetics and response behaviors of mechanophores under various stimuli. The effects of various factors on the efficacy and the activation energy of mechanophores were studied, enhancing the capabilities of mechanophores for visualizing increasingly complex stress-loading situations.

Research groups led by Constantino Creton [42, 22, 43], Davis [20, 44, 45, 46] and Sottos and White [34, 47, 48] focus more on realizing the stress distributions and stress concentrations in the bulk materials. On the other hand, research groups led by Steven Craig [26, 39] and Sottos and White [49, 50] focus more on the microsystems - single molecule force studies [39] and microscopic crack propagations [50].

Mechanophores have been shown to effectively light up and help replicate the stress distributions in various bulk loading cases such as tension [46], compression [46], shearing [48], three-point bending [36], sequential loading [26, 43], friction scratches [45] and even internal swelling [51]. Studies have tried to test the mechanophore capability a bit more by identifying the stress concentrations in the structure through notches [50, 49, 42], and trying to visualize the crack propagation in real-time [22].

In the following subsections, various examples demonstrating the capability of mechanosensing for stress visualization will be discussed at both the micro-scale and the macro-scale.

2.3.1. Visualization of stress concentrations at the macro-scale

At the macro scale, bulk deformation methods such as tension and compression distribute loads across the cross-section of a sample. This induces local stress within the material and causes the activation of mechanophores.

1. **Uniaxial tension loading:**

   Kim et al. (2018) investigated the mechanoresponsive activation of two isomers of spiropyran in cross-linked polymeric materials. The activation stresses, and strains with two different constant strain rates (0.05-0.005 s^{-1}) were reported and analyzed [47].

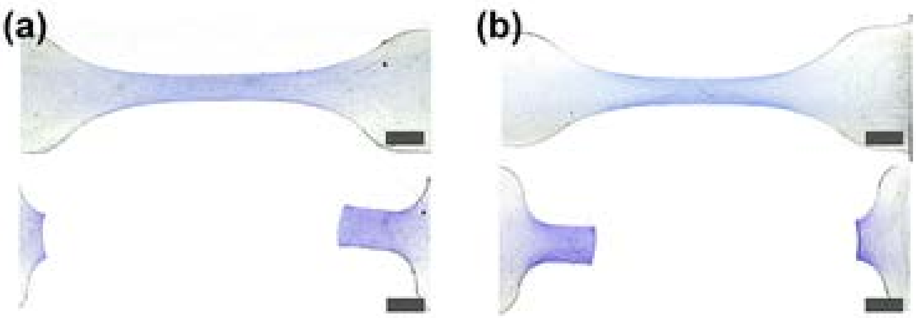

Figure 2.11: Optical images of PDMS polymers with differently linked spiropyran molecules. The top and bottom images depict the samples upon tensile loading and upon fracture, respectively; Image adapted from ref. [47].

2. **Three-point bending:**

   In structural plastics, brittle failure precedes any detectable color change in mechanophore spiropyran. Vidavsky et al. (2019) found a solution by polymerizing dihydroxyspiropyran as a comonomer to embed mechanochromic properties into a polycarbonate glassy polymer. New efficient preparation and processing methods for better activation efficiency of spiropyran are also discussed [36].

   In the process, a three-point bending test was performed on the spiropyran-linked glassy polymer, and the thermomechanical properties were extensively studied.

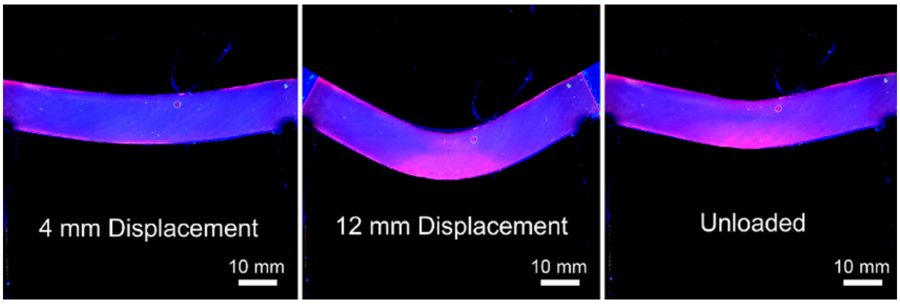

Figure 2.12: Spiropyran fluorescence field during three-point bending at 4mm, 12mm bending displacement, and the unloaded state; Image adapted from ref. [36].

3. **High-rate impact test:**

   With an aim at understanding brain strain for traumatic brain injuries, Xia et al. (2019) performed a high-rate impact test using an in-house air cannon test setup to achieve high strain rates of 1500 s^{-1}. A spiropyran-linked PDMS polymer was impacted by a projectile, which showed reversible activation of spiropyran and demonstrated the application of spiropyran molecules for sensing impact strains [52].

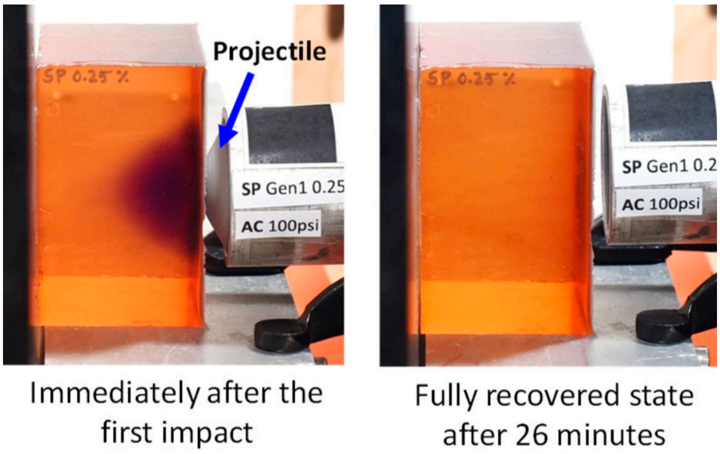

Figure 2.13: Color change in spiropyran-linked PDMS during and after impact at an impact speed of 100 $\mathrm{m\,s^{-1}}$; Image adapted from ref. [52].

4. **Relation between residual stress and spiropyran decay time:**

   Janissen et al. (2022) investigated the influence of residual stresses in the glassy polymer Polymethyl Methacrylate (PMMA) on the mechanochemistry of spiropyran molecules. Spiropyran molecules were excited with UV light within a glassy polymer matrix and the molecules' fluorescence decay over time was studied. Fig. 2.14 shows a heatmap of the decay rate for a circular sample. The circular sample should have more residual stress near the edges which can also be seen in the heatmap, which indicates a relation between the residual stress and the time decay.

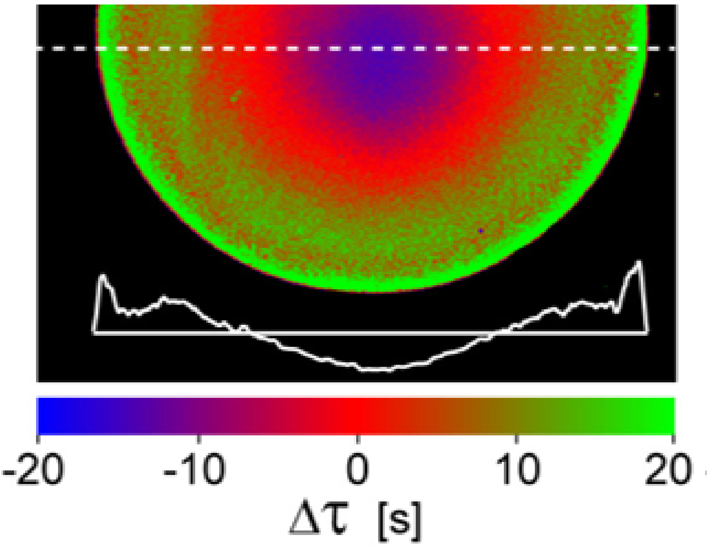

Figure 2.14: Heatmap of time decay of spiropyran in PMMA polymer matrix after UV activation; Image adapted from ref. [32]

2.3.2. Visualization of stress concentrations at the micro-scale

Using mechanophores, phenomena such as crack propagation have been visualized on the micro-scale. The activation of spiropyran molecules near the vicinity of the crack has been used to reproduce a stress field around the crack tip. The fluorescence can be used to predict the propagation direction of the crack at that particular instant.

1. **Stress visualization at crack tip:**

   Celestine et al. (2014) studied fracture-induced mechanochemical activation for rubber-toughened PMMA with spiropyran molecule cross-linked. Single Edge Notch Tension tests were performed, and spiropyran activation was quantified using fluorescence imaging. The region of spiropyran activation was found to correlate directly with the size of the plastic zone ahead of the crack [50].

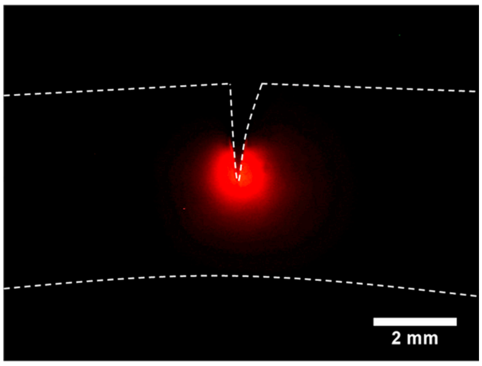

Figure 2.15: Fluorescence image during SENT testing showing activation zone; Image adapted from ref. [50].

2. **Characterization of force relationship of spiropyran isomers:**

   In order to calculate the magnitude of force necessary to activate a spiropyran isomer to a colored merocyanine form, Gossweiler et al. (2015) used an Atomic Force Microscope (AFM) tip. By using the AFM tip to pull on the molecule until it is activated, they determined that the ring-opening of spiropyran occurs at forces of $\sim 240\ \mathrm{pN}$ applied over a timescale of 10 ms.

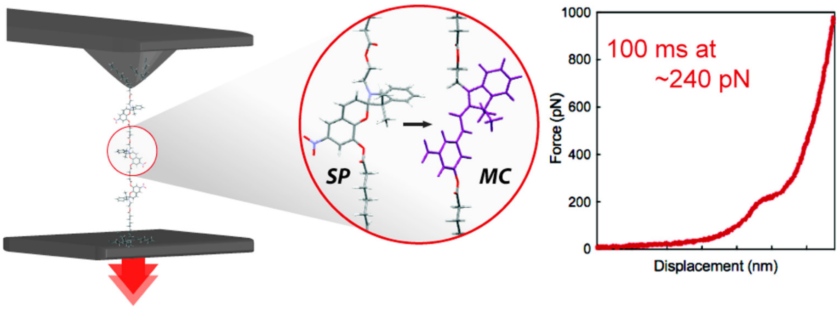

Figure 2.16: Spiropyran pulled to an extended merocyanine isomer, revealing a visibly colored merocyanine; Image adapted from ref. [39].

2.4. Attempts at quantitative stress mapping in mechanosensing

The capabilities of mechanosensing have been qualitatively shown time and again. However, to transform mechanosensing into an industry-ready sensor technology, many challenges have to be addressed through rigorous research. The biggest of the challenges is the calibration of the mechanophore activation response with a stress value. Overcoming this challenge opens doors for mechanosensing to be implemented as self-reporting damage sensors and eventually to indirect applications such as haptic feedback, safety systems, and wearable health monitors [20].

There have been relatively few attempts to correlate the mechanochromic response to stress values. This section will explore the four known attempts to quantify fluorescence into mechanical constructs like stress and strain.

2.4.1. Gossweiler et al. (2014)

Cephalopod-inspired design of electro-mechano-chemically responsive elastomers for on-demand fluorescent patterning.

In 2014, Gossweiler et al. explored the potential to generate on-demand fluorescence patterns by creating specific strains within specific regions of a polymer (Fig. 2.17 (a)). This required them to establish a calibration between the fluorescence and strain. They quantified the fluorescence intensity of the elastomer as a function of uniaxial engineering strain.

$$I = (1+\epsilon)^2 + (1+\epsilon)^{-2} + 1,$$

$$\frac{S}{S_0} = f(I) = -0.004I^3 + 0.098I^2 - 0.557I + 1.816.$$

The first invariant of the right Cauchy-Green deformation tensor $\mathbf{I}$ was used to characterize the degree of stretching. The normalized fluorescence intensity S/S_0 was plotted against the First Invariant (I), and using parametric fitting, a relation between I and S/S_0 was achieved.

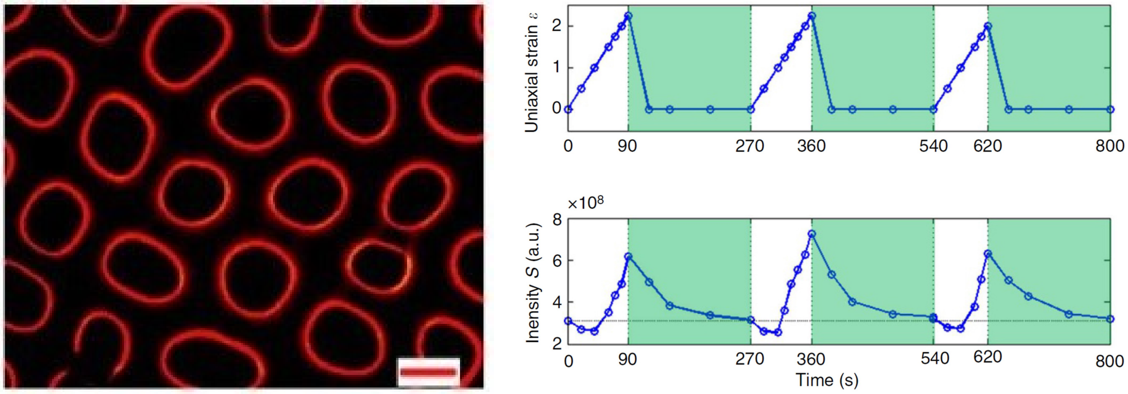

(a)

(b)

Figure 2.17: (a) Fluorescent microscope images of the Elastomer film under an electric field of 63.1 $kVmm^{-1}$, (b) Cyclic uniaxial strain applied to an elastomer and the corresponding fluorescence intensity; Image adapted from ref. [26].

The parametric fitting allowed for the prediction of the fluorescence for a certain input electric field. The study by Gossweiler et al. [26] improves our understanding of the linkage between fluorescence and strain for mechanophore embedded polymers.

2.4.2. Celestine et al. (2019)

Strain and stress mapping by mechanochemical activation of spiropyran in poly(methyl methacrylate).

Celestine et al. (2019) analyzed the fluorescence imaging of the region around the crack tip of the propagating crack in poly(methyl methacrylate) (PMMA), commonly known as acrylic, as depicted in Fig. 2.19 (a).

They performed a Single-edge notch test (SENT) test and calculated the stress field around the crack using the Hutchinson–Rice–Rosengren singularity field equations. They employed Least Squares Regression Analysis to fit the stress and strain data as a function of distance from the crack tip to a power law. The yield stress (σ_Y) was determined using Considère's yield criterion, and the material model for PMMA was modelled using the Ramberg–Osgood stress–strain relation for an elastic–plastic material.

Further, the activation stress and strain for the embedded spiropyran were determined by fitting a Gaussian distribution to the fluorescence intensity data as shown in Fig. 2.18 (b). The activation zone limits were determined as the locations with intensities one standard deviation above the background intensity.

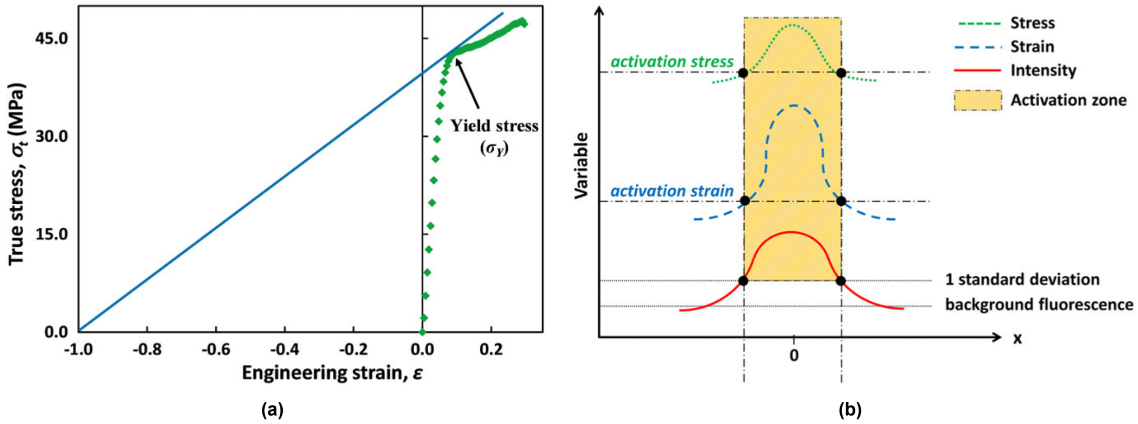

Figure 2.18: (a) Considère's construction for determining the yield stress of a material, (b) Schematic of activation stress and strain analysis; Image adapted from ref. [49].

The activation zone limits of stress and strain were used to calibrate the power law constant (β) for stress, strain, and fluorescence measurements, thereby generating estimated Stress and strain plots about the crack tip Fig. 2.19 (c). The strain values calculated from the fluorescence were validated with the strain values calculated via Digital Image Correlation of the sample.

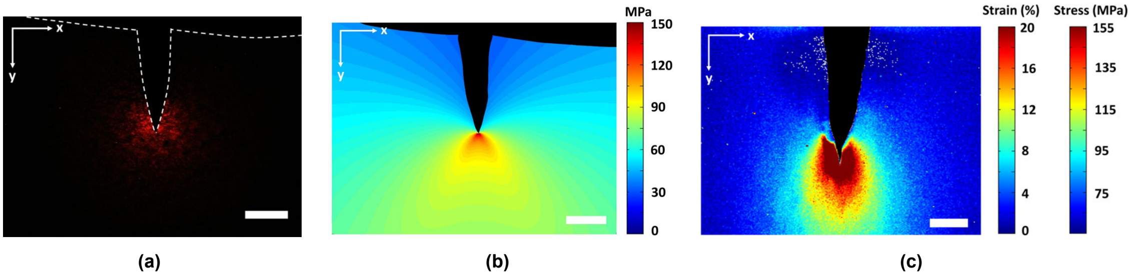

Figure 2.19: (a) Fluorescence intensity of the crack tip, (b) Equivalent stress calculated using Digital Image Correlation strain field measurements, (c) Estimated equivalent strain and equivalent stress distribution without direct strain measurements; Images adapted from ref. [49].

Despite its novel approach, the study by Celestine et al. (2019) faces several limitations:

1. **Valid for very small local region around the crack**:

   Data Analysis was restricted to regions where HRR singularity equations and small-scale yielding was applicable. This was done because the HRR singularity equations assume the strain and stress to drop following a Power Law. This is true only in the close vicinity of the crack tip, limiting the scope of the analysis to a very small length scale.

2. **Limitations due to use of Material model**:

   The Ramberg–Osgood stress-strain relation has been used as the constitutive material model. While constitutive material models provide valuable estimations of material behavior, they often do not accurately predict responses for large strains that are beyond the yield point, especially in soft materials which can experience fractures at very high strains (around 200%).

2.4.3. Chen et al. (2020)

From force-responsive molecules to quantifying and mapping stresses in soft materials.

Stress fields in loaded objects, especially those of arbitrary shape, are spatially heterogeneous. To accurately capture strain data in critical zones near cracks or areas with sharp stress gradients, it is essential to record a high number of images during data collection. This ensures that no immediate deformation information is lost while calculating stress from the measured strain data [42]. Chen et al identified this issue and formulated a new approach that bypasses the use of a material model for stress calculations. Their approach, termed ”RGB analysis”, uses the mechanochromic response of mechanophores.

They performed a uniaxial test on a rectangular sample prepared by photopolymerizing an initial network containing ethyl acrylate (EA) monomers, spiropyran, and 1,4-butanediol diacrylate (BDA) crosslinkers and 2-hydroxy-2-methylpropiophenone (HMP) photoinitiators. Chromatic changes (ΔR, ΔG, ΔB) were calculated with the RGB content at the beginning of the experiment as the basis.

As the sample was stretched, the conversion of spiropyran to merocyanine was observed, indicated by a decrease in the red component and an increase in the blue component of the RGB values, as seen in Fig. 2.20 (a). This emission data is used as a calibration curve for the stress as a function of blue and red chromatic change.

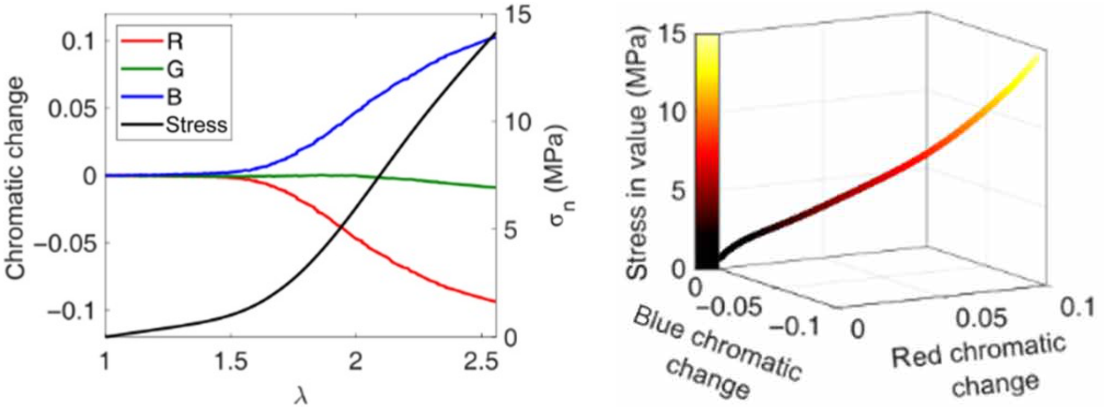

(a) (b)

Figure 2.20: (a) Chromatic change as a function of stretch for images extracted from the video of uniaxial extension, (b) Calibration curve for the stress as a function of the blue and red chromatic change; Images adapted from ref. [42].

An interesting finding from their analysis is that the response of the mechanochromic material seemed to relate more to changes in nominal stress rather than strain. Fig. 2.21 shows the chromatic change observed vs the nominal stress (σ_N) and the stretch ratio (λ), respectively, for various concentrations of spiropyran in the polymer. The observation is that the chromatic change occurs at different stretch ratios but with the same nominal stress. This challenges the notion of strain being the primary measured quantity by the fluorescence in spiropyran.

Further experiments included fracture tests on a sample with a single-notch geometry. The stress field was obtained by using the calibration on the mechanochromic response captured via RGB imaging. The obtained stress field is shown in the Fig. 2.22 (a).

To validate the obtained stress field, Finite Element Simulations were compared with the experimental result for various stretch ratios and concentrations of spiropyran (Fig. 2.22 (b)).

2.4.4. Gohl et al. (2023)

Stress quantification in a composite matrix via mechanophores.

Polymer matrix composites incorporate rigid fiber reinforcements into the matrix to obtain strong and lightweight properties. Gohl et al. (2023) explored the stress concentrations that occur near the interface. The team developed single-particle model composite samples by embedding functionalized glass particles within a silicone/mechanophore matrix, allowing for direct stress observations at the microscopic level.

Confocal microscopy was used to measure the mechanophore activation in situ during mechanical loading. The fluorescence data was collected and then correlated to the maximum principal stress values

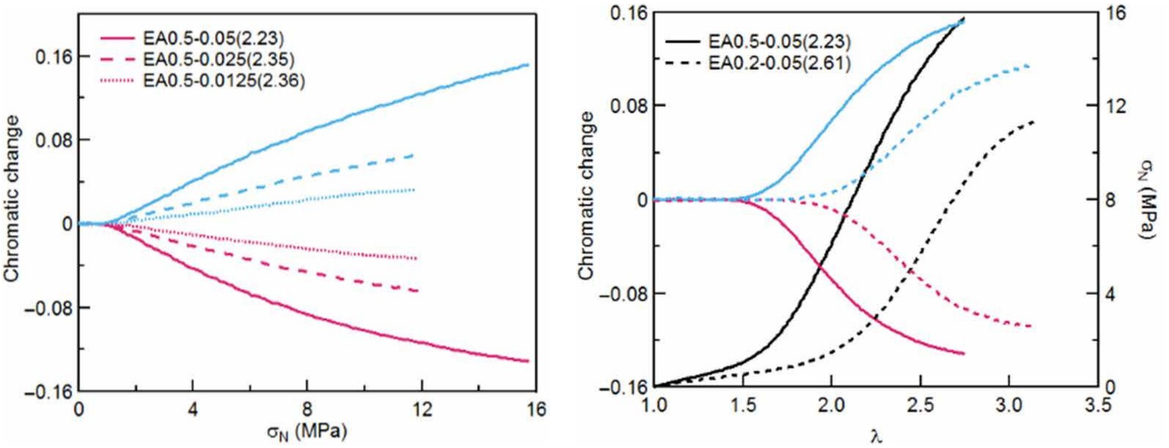

(a)

(b)

Figure 2.21: (a) Red and blue chromatic change plots as a function of nominal stress (σ_N), (b) Stress-strain curves (black lines) and red and blue chromatic change as a function of stretch ratio (λ) for elastomers with various spiropyran concentrations; Images adapted from ref. [42].

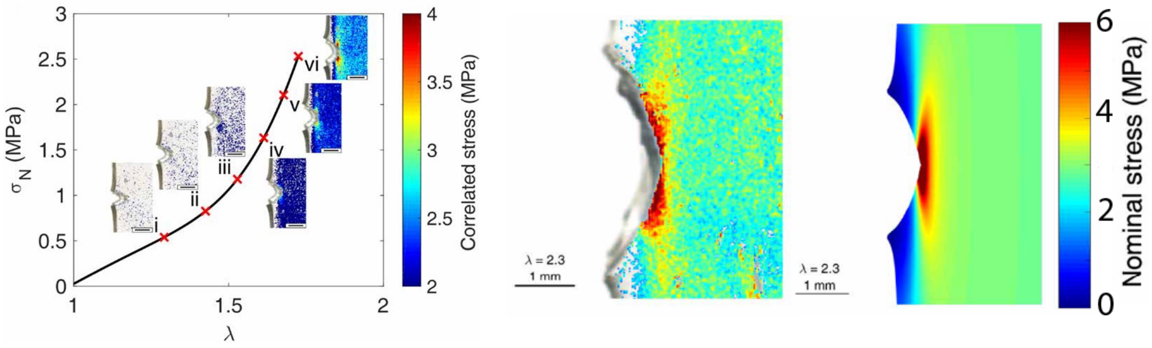

(a)

(b)

Figure 2.22: (a) Stress-strain curve of a uniaxial test of the sample with a single-notch geometry, (b) Comparison of the experimentally obtained and the computationally simulated stress map [42].

derived from a finite element analysis (FEA) model of the composite system. The FEA model utilizes an Ogden hyperelastic model to represent the elastomer. Using the calibration obtained from a single-particle composite, they investigated the stress distribution around cylindrical particles embedded in the matrix.

2.5. Literature conclusions

This section summarized the principal insights and limitations identified in the reviewed literature. There are certain drawbacks in the approaches taken to connect fluorescence and the stress in the material quantitatively.

Using constitutive models to calculate stress from strain inherently involves several assumptions, detailed in subsection 2.4.2. Specifically, these models often apply the small-strain assumption, which is suitable for materials experiencing only minor deformations. However, this assumption becomes invalid for soft polymers such as elastomers, where strains exceed $\varepsilon = 200\%$.

Gossweiler et al. (2014) did not aim to directly quantify stress from fluorescence. Celestine et al. (2019) did not assume a small strain, but the use of material models and HRR singularity field equations limited their analysis scope. More recent studies by Chen et al. (2020) and Gohl et al. (2023) have acknowledged both these issues and generated stress fields directly from the chromatic change and fluorescence measurements, respectively.

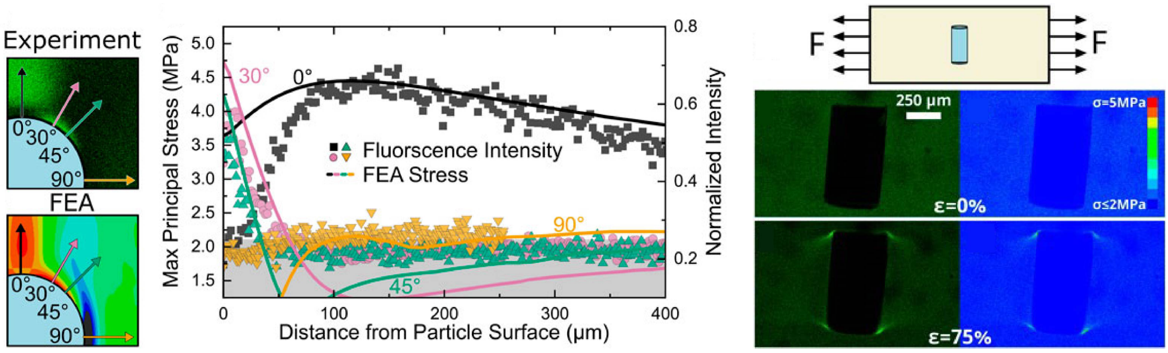

(a)

(b)

Figure 2.23: (a) Fluorescence intensity and FEA images of stress distributions as a function of angle with the loading direction, (b) In situ fluorescence intensity images of short glass cylinder oriented perpendicular to loading direction; and corresponding calibrated stress images utilizing calibration determined from single-particle experiments; Images adapted from ref. [44].

There are two significant gaps that none of the papers thus far have addressed.

1. Previous studies have primarily concentrated on correlating the fluorescence with the nominal stress of the material (σ_N) or equivalent stress measures like von Mises stress without extending the analysis to the correlation of the entire stress tensor.
2. All attempts to connect the fluorescence of spiropyran and the stress in the material have adopted an engineering-focused perspective in the research. A study from the fundamental aspect has not been pursued yet.

3

Research methodology

3.1. Research objectives

The preceding chapter established a basic understanding of mechanosensing and explored the efforts made to quantify the fluorescence of spiropyran for stress mapping. As detailed in Section 2.3.1, some qualitative relation can be observed between the time decay constant of UV-activated spiropyran and the residual stress in the glassy polymer PMMA [32]. However, a fundamental approach to correlate the activation of spiropyran with stress has not been developed yet, representing a gap in the current research.

This thesis aims to bridge this research gap by correlating various numerically calculated continuum mechanics quantities with the following two experimentally obtained local quantities:

1. Fluorescence intensity.
2. Exponential decay time constant for spiropyran decay after UV-aided activation in the mechanically stressed state.

The second quantity is referred to as the ”decay rate time constant” throughout the remainder of this work. Two research questions are formulated as follows:

”How is (a) the fluorescence intensity of the mechanophore spiropyran in a PDMS polymer induced through mechanical activation correlated with (b) various continuum mechanics quantities?”

and

”How is (a) the decay rate time constant of the mechanophore spiropyran in a PDMS polymer induced through mechanical activation correlated with (b) various continuum mechanics quantities?”

To demonstrate the contributions of this work, the following research objectives are devised:

1. Develop, build, and validate a uniaxial tensile tester setup with a simultaneous displacement, force, and fluorescence detection capability.
2. Design and perform dark-room experiments to investigate the fluorescence decay behavior during uniaxial tensile testing conditions.
3. Create a numerical model that mimics the experiment to simulate the behavior and extract local continuum mechanics quantities for further analysis.
4. Systematically investigate the correlations between various numerically computed quantities and the experimentally obtained fluorescence response of spiropyran-embedded PDMS using empirical data.

3.2. Thesis overview

In order to achieve the research objectives, this thesis is divided into three phases:

1. Experimental Phase
2. Simulation Phase
3. Correlation Phase

The thesis is structured in advance along two fronts - the experimental and the simulation phase. In the last segment of the thesis, the results from both the experimental and simulation phases are combined in the correlation phase. The following sections will elaborate further on the details and expected outcomes of each phase.

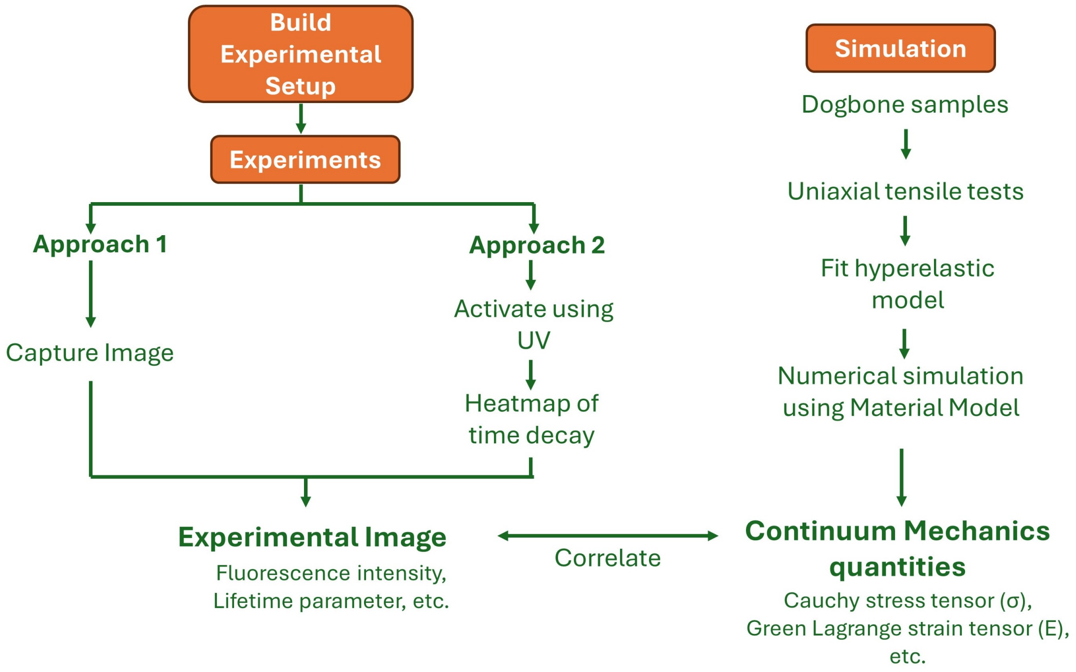

Figure 3.1: Thesis overview

3.2.1. Experimental methodology

Experimental setup and validation

The initial step in the experimental phase involves the design and building of a uniaxial tensile testor. The tensile testor setup is designed to capture force, displacement, and fluorescence data through independent channels - the load cell, the linear stage, and the CMOS camera, respectively. The setup integrates a 200 N load cell to a linear stage via peripheral components. A signal conditioner and a Digital-to-Analog converter are used to capture the force data measured by the load cell. To control the setup and gather data efficiently, a Python script is developed to manage the operations of the linear stage and a LabVIEW program is implemented for the force data capture from the load cell.

Following the assembly, the tensile testor setup is validated for dynamic and static tests across various parameters. The details of the experimental setup and the validation are documented in Appendix A.

Geometry selection for experiments

For the experiments, Polydimethylsiloxane (PDMS) is selected as the best choice of polymer for embedding spiropyran because of its transparency, moldability and high strain tolerance. The PDMS base and curing agent are mixed in a ratio of 10:1 to prepare the sample.

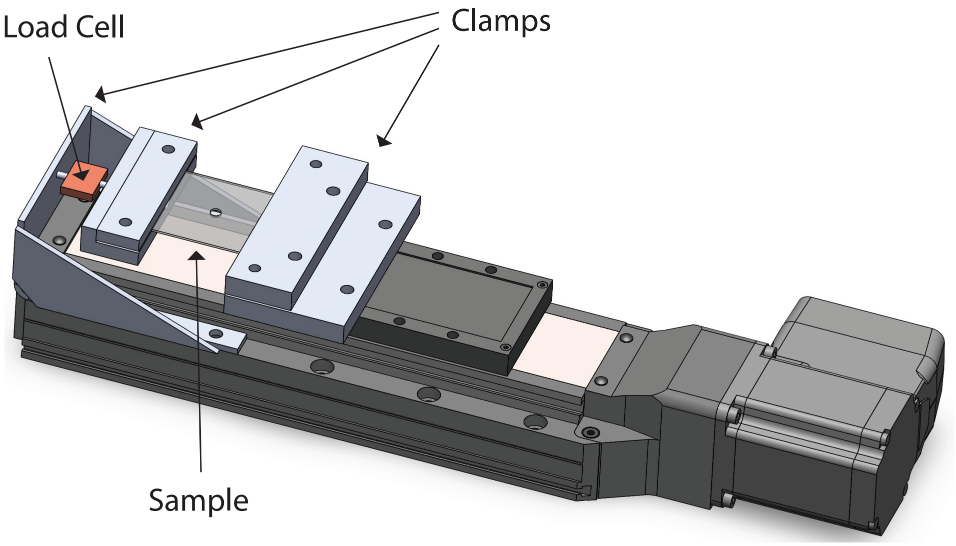

Figure 3.2: CAD Model of the Experimental setup

The chosen geometry for the molded sample is a rectangular plate of $30 \times 30 \times 1$ mm, with a central circular hole. When uniaxially stretched, the sample experiences the maximum equivalent stress at the top and bottom of the hole, with comparatively lower equivalent stress along the direction of stretching. Fig. 3.3 (b) illustrates this distribution with high stresses shown in red and low stresses in blue.

In the existing literature, simpler geometries like a rectangular sample were chosen. The stress distribution for these designs varies only in the direction of stretching. However, the stress visualization for the chosen geometry is complex enough that all four components of the stress tensor are included. This allows for a more holistic stress solution and thus a more extensive correlation between experimental and numerical results.

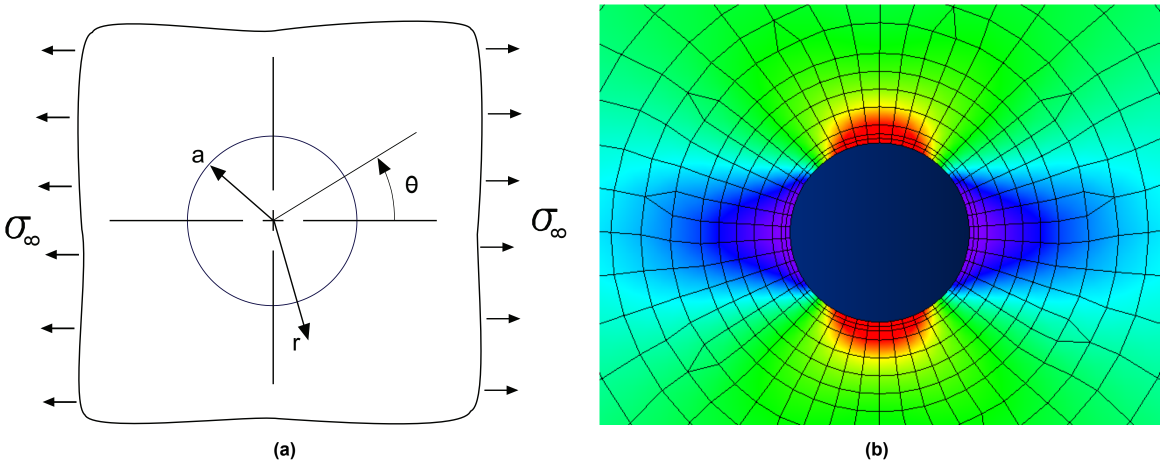

Figure 3.3: (a) Schematic diagram of the analytical model of a plate-with-a-hole, (b) Visualization of the stress field using Finite Element Method; Image adapted from ref. [53].

Imaging process

The imaging process employed in this work is designed to exclusively capture the fluorescence of merocyanine and exclude the parasitic light, such as the reflected light from the sample. The basis of the imaging process lies in the absorption and emission spectrums of spiropyran and merocyanine molecules.

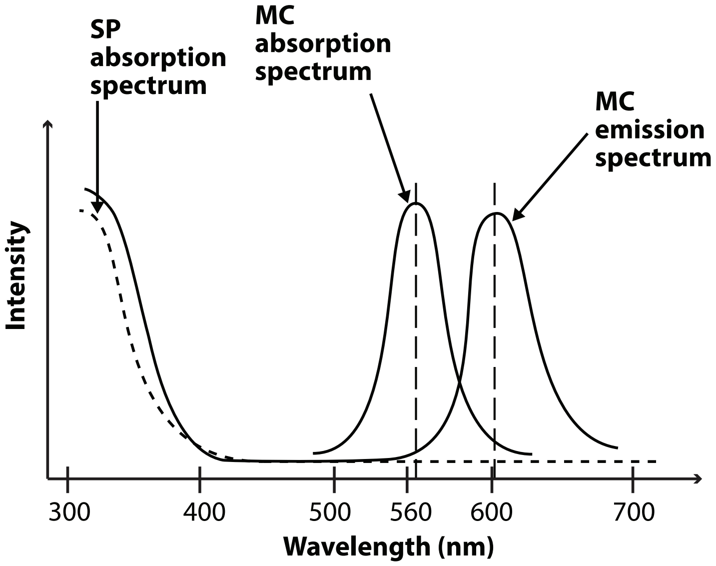

Figure 3.4: Absorption and emission spectrum of spiropyran and merocyanine; Image adapted from ref. [54]

In the equilibrium between spiropyran and merocyanine, spiropyran is non-fluorescent whereas merocyanine is a fluorescent molecule. Even if the equilibrium is highly skewed towards spiropyran due to the prevailing environmental conditions, there is always some quantity of merocyanine in the polymer. The absorption spectrum of spiropyran and merocyanine, and the emission spectrum of merocyanine are shown in Fig. 3.4. Merocyanine absorbs light in a range of wavelengths centered around 565 nm and emits fluorescence in a range of wavelengths centered around 605 nm [54]. These wavelength values differ depending on the particular functional group linked to spiropyran. Both spiropyran and merocyanine absorb UV light.

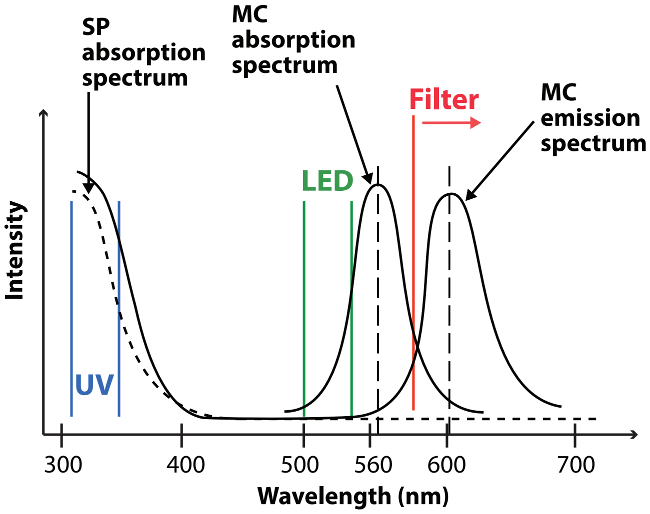

Figure 3.5: Spiropyran and merocyanine absorption and emission spectrums with input, excitation and filter wavelengths specified; Image adapted from ref. [54]

To excite merocyanine, a broadband LED emitting light in the range of 520 $\pm$ 20 nm is used, which lies in the absorption range of merocyanine. The light is directed onto the sample via an optical fiber and a diffuser. For specific experiments, UV light is used to excite the spiropyran and merocyanine to a fluorescent state.

Capturing the fluorescence requires filtering out the scattered and reflected light. A reflective high optical density filter is attached in front of the lens on the CMOS camera which acts as a long pass filter and blocks light of all wavelengths below 575 nm. This excitation and filtering process is summarized in Fig. 3.5.

Data from the experimental phase is gathered via two types of experiments, as described in Fig. 3.1. The experiments are explained below in detail:

Experimental Approach 1 - Fluorescence image

The first set of experimental data is obtained by measuring the fluorescence intensity from activated merocyanine within the sample in a stressed state. The sample is stretched to a strain $\varepsilon = 0.9$ at a strain rate $\dot{\varepsilon} = 0.025s^{-1}$. In the stretched state, a static image of the sample is captured using the CMOS camera. Fig. 3.6 (b) displays the static stretched image obtained from this procedure.

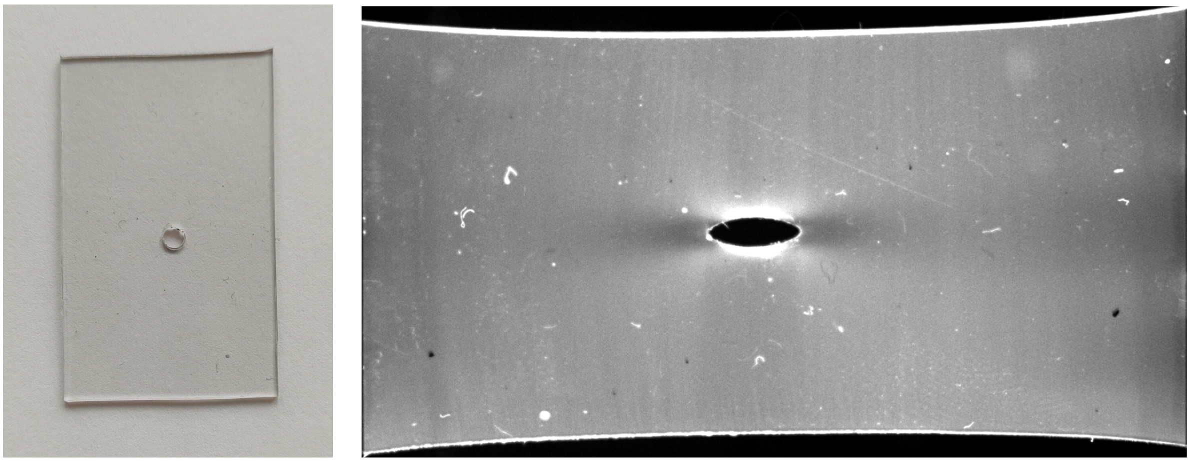
(a) (b)

Figure 3.6: (a) A spiropyran-embedded PDMS sample, (b) Fluorescence image of a sample stretched to $\varepsilon = 0.9$

Experimental Approach 2 - Decay rate time constant image

The second set of experimental data focuses on obtaining the decay rate of merocyanine, after activation using UV light within a stretched sample. For consistency in experimental results, the sample is again stretched to a strain $\varepsilon = 0.9$ at a strain rate $\dot{\varepsilon} = 0.025s^{-1}$. Since PDMS is a viscoelastic material, the sample is allowed to rest for 45 minutes to allow the stress relaxation process to stabilize.

Once the sample is stationary, UV light is applied until the fluorescence intensity of the sample increases to 5 times the baseline level. The intensity is allowed to drop to 3 times the baseline before starting the video capture.

It was observed that the fluorescence decay consisted of two exponents - a fast and a slow exponential decay. Following this protocol ensures that the initial fast exponential decay is allowed to subside, and only the slow exponent is captured.

The fluorescence intensity decay data is analyzed using an in-house graphical user interface (GUI) analysis tool shown in Fig. 3.7. A detailed description of the tool and its functionality is provided in Appendix A. An exponential curve is fitted to every pixel in the video frame to determine the decay time constant. The extracted decay time constants are visualized in a heatmap as shown in Fig. 3.8.

For clarity and ease of reference within this work, the two experimental images - the fluorescence image and the decay rate time constant heatmap are referred to as the Experimental data. The next subsection describes the simulation methodology employed to derive mechanical quantities for correlation.

3.2.2. Simulation methodology

For the simulation phase, COMSOL Multiphysics software is selected to perform the solid mechanics simulations using a hyperelastic material. To accurately simulate the 10:1 ratio PDMS embedded with

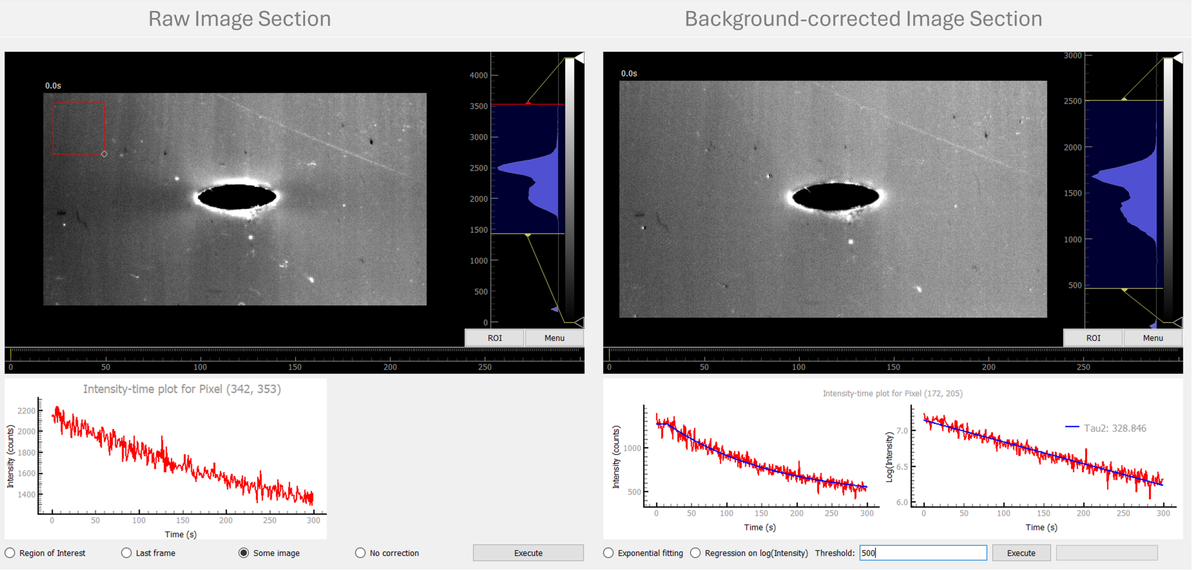

○ Region of Interest ○ Last frame ● Some image ○ No correction

○ Exponential fitting ○ Regression on log(Intensity) Threshold: 500

Figure 3.7: Graphical User Interface used for image postproocessing

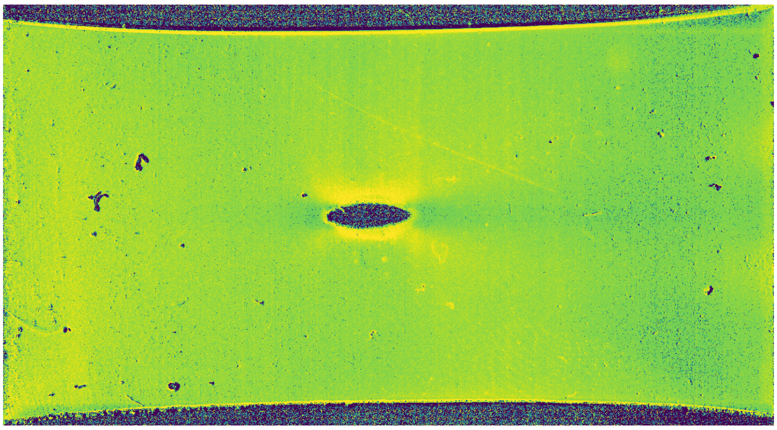

Figure 3.8: Visualization of decay rate time constant data

spiropyran, material properties have to be determined. This is done by curing dogbone samples of spiropyran-embedded PDMS and performing uniaxial tensile tests on them until failure, using the in-house experimental setup. The stress-strain data obtained from these tests are parametrically fitted to a Yeoh hyperelastic material model.

This material model is subsequently used in COMSOL simulations, where the sample is stretched to the similar strain $\varepsilon = 0.9$. Since a higher spatial resolution is required near the hole, the mesh is refined in the vicinity of the hole as compared to the rest of the geometry. The mesh configuration is shown in Fig. 3.10. The steps taken to validate the numerical model are outlined in Appendix C.

The simulation phase provides continuum mechanics quantities for detailed analysis. These include the First Piola-Kirchoff stress tensor $(\mathbf{P})$, von Mises stress (σ_{VM}) and Green-Lagrange strain tensor $(\mathbf{E})$. Various other quantities are obtained using transformations, ensuring that all quantities are ready for correlation with the experimental data. An extensive list of the quantities is provided in Appendix D, referred to as simulation data for simplicity. Fig. 3.11 shows the distribution of the von Mises stress across the entire sample, providing a visualization of the stress distribution.

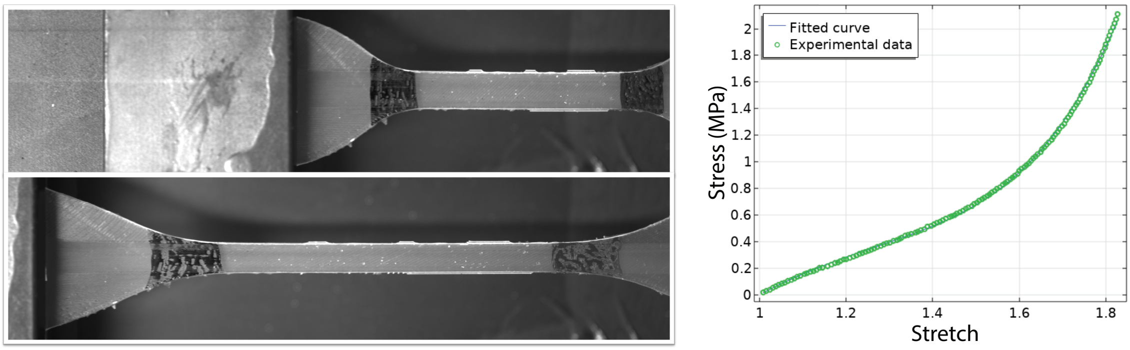

(a) **(b)**

Figure 3.9: (a) Dogbone sample in the experimental setup at $\varepsilon = 0$ and $\varepsilon = 0.8$, (b) Experimentally obtained stress-strain data and the parametrically fit Yeoh hyperelastic material model

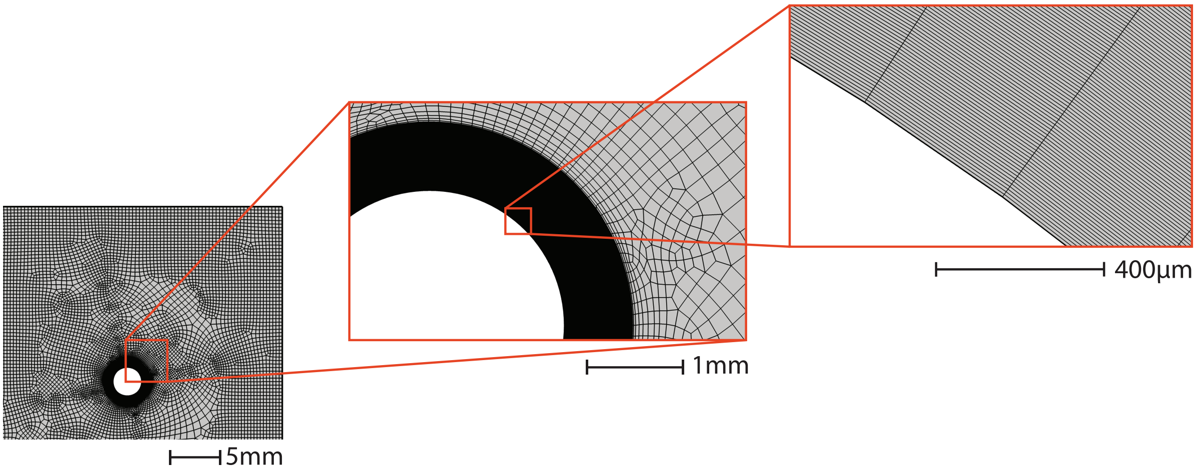

Figure 3.10: The mesh configuration of the numerical simulation

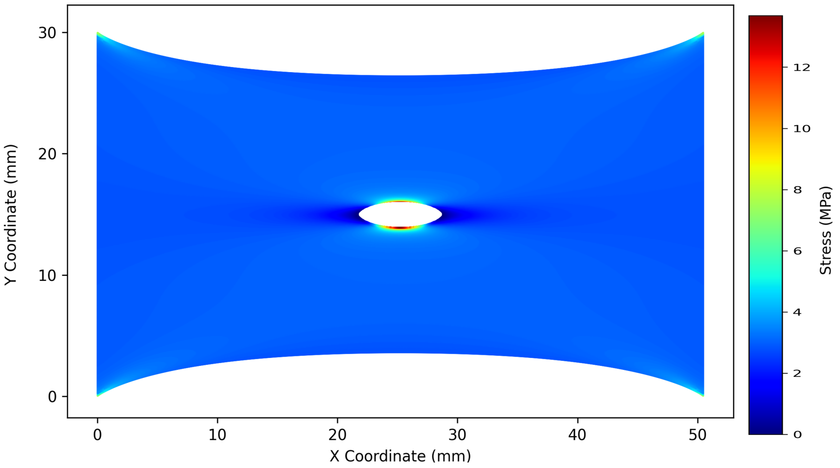

Figure 3.11: Numerically simulated von Mises stress distribution (σ_{VM})

3.2.3. Correlation methodology

Once the experimental data and the simulation data are available, 360 radial lines are drawn on the simulation data from the center of the elliptical stretched hole, as depicted in Fig. 3.12 (a). An affine transformation is applied to the simulation image to align the elliptical holes in both images. The radial lines are also transformed using the same transformation. Fig. 3.12 (b) shows the overlaid images with the transformed radial lines.

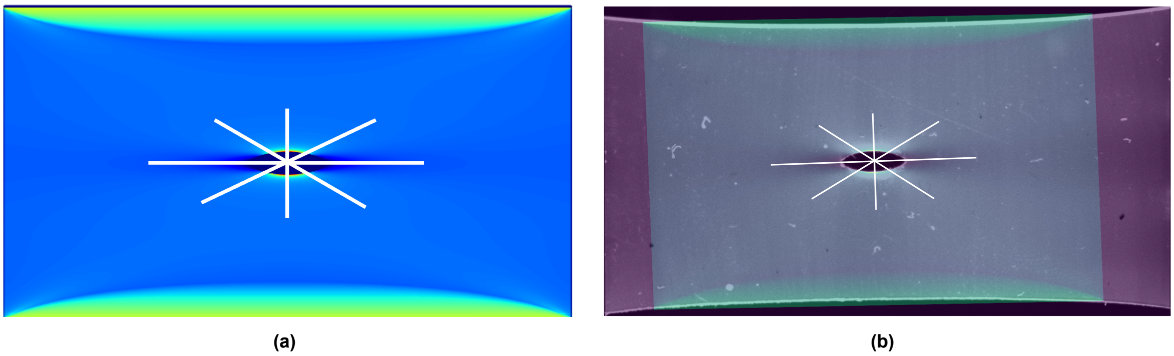
(a) (b)

Figure 3.12: (a) Radial lines on the simulated von Mises stress distribution, (b) Simulated von Mises stress overlaid on the fluorescence image obtained experimentally

Pixel intensity values of the transformed radial lines are extracted from both the experimental and the simulation datasets. These values are correlated to evaluate the relation between the two forms of experimental data and various simulated continuum mechanics tensor components and their derivatives.

4

Fluorescence measurements of mechanically-induced spiropyran activation

This chapter presents significant observations made during the experiments conducted on spiropyran-embedded PDMS samples. In the experiments, the sample is stretched in the horizontal direction as per the procedure of Experimental Approach 1. Fig. 4.1 shows the sample in its unstretched and stretched states respectively at an applied strain $\varepsilon = 0.9$. High fluorescence intensity can be seen at the top and bottom of the hole in the stretched sample with comparatively lower intensities in the horizontal direction around the hole. This sample behavior is expected when compared to the numerically calculated stress distribution shown in Fig. 3.11.

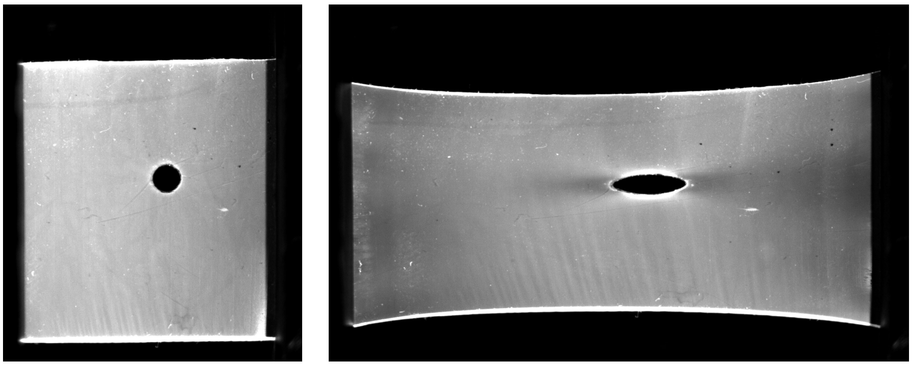
(a) (b)

Figure 4.1: SP-embedded PDMS sample in (a) unstretched state and (b) stretched to a stain of $\varepsilon = 0.9$

Upon reverting the sample back to its unstretched state, the fluorescence patterns formed by stretching the sample are retained, gradually decaying over a period of approximately 10 minutes. This behavior is expected from an spiropyran-embedded PDMS sample. In the stretched state, mechanical stress provides the energy for breaking the C-O bond and eventual ring opening of spiropyran to form the merocyanine molecule. Once the mechanical stress is removed, the merocyanine starts to revert to its spiropyran state, which is more stable in unstretched conditions.

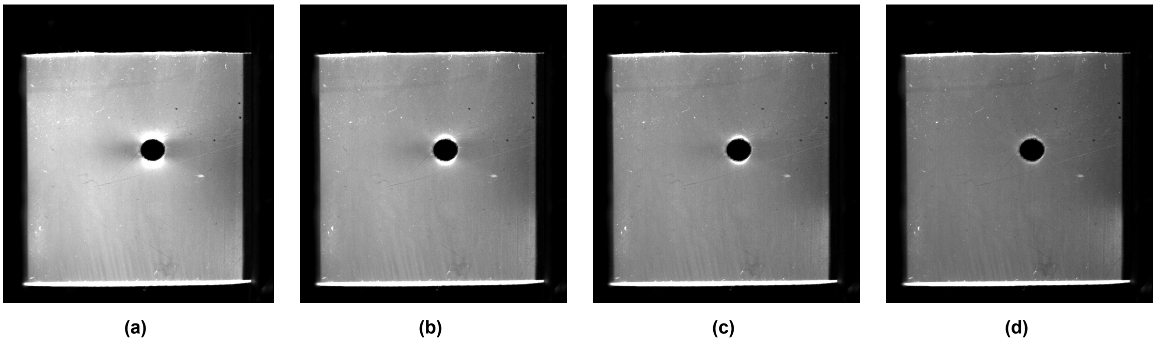

(a) (b) (c) (d)

Figure 4.2: PDMS sample with covalently bonded spiropyran after (a) 0 minutes, (b) 4 minutes, (c) 10 minutes, and (d) 18 minutes of unstretching

Before concluding the experimental phase, it is necessary to verify that the fluorescence captured by the camera indeed originates from the spiropyran to merocyanine conversion caused by mechanical stress. To be completely sure of the origins of the fluorescence, alternate hypotheses have been generated. Using controlled experiments and contradictions, the alternate hypotheses are negated. The two possible alternate reasons for the origin of fluorescence can be as follows:

1. Photoelasticity due to elasticity
2. Photoelasticity due to viscoelasticity

4.1. Ruling out "Photoelasticity due to elasticity"

Hypothesis: The fluorescent patterns of high fluorescence at the top and bottom of the hole and relatively low fluorescence at the sides of the hole are caused by photoelasticity due to elasticity.

Stretching the transparent polymer materials bends light near high-stress regions due to changes in refractive index. This causes a suspicion that the contrast in intensities could be due to photoelasticity.

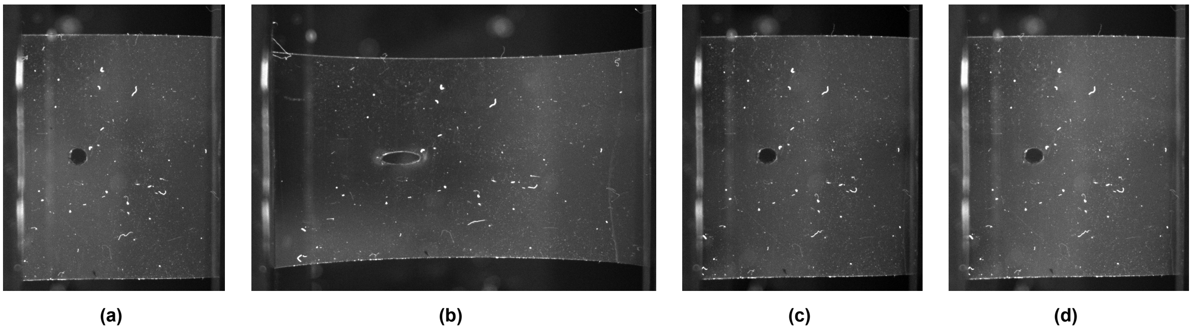

(a) (b) (c) (d)

Figure 4.3: PDMS sample without spiropyran in its (a) Pristine state, (b) Stretched to $\varepsilon = 0.9$, (c) Immediately after unstretching, and (d) 7 minutes after unstretching

To rule out this hypothesis, a control experiment was conducted using a PDMS sample without spiropyran. As seen in Fig. 4.3, no fluorescence contrast can be observed in the images. Since there was no fluorescence observed, after unstretching, no decay was observed either. This result confirms that the fluorescence contrast is not due to ”photoelasticity due to elasticity”.

4.2. Ruling out "Photoelasticity due to viscoelasticity"

Hypothesis: The fluorescent patterns of high fluorescence at the top and bottom of the hole and relatively low fluorescence at the sides of the hole are caused by photoelasticity due to viscoelasticity.

Upon being stretched, viscoelastic materials experience a reduction in force under a constant applied strain due to stress relaxation. Similarly, when the stretching force is removed, viscoelastic materials retain some of the induced stresses, which then gradually relax over time. This causes suspicion that the fluorescence decay after stretching could be due to photoelasticity clubbed with stress relaxation caused by viscoelasticity.

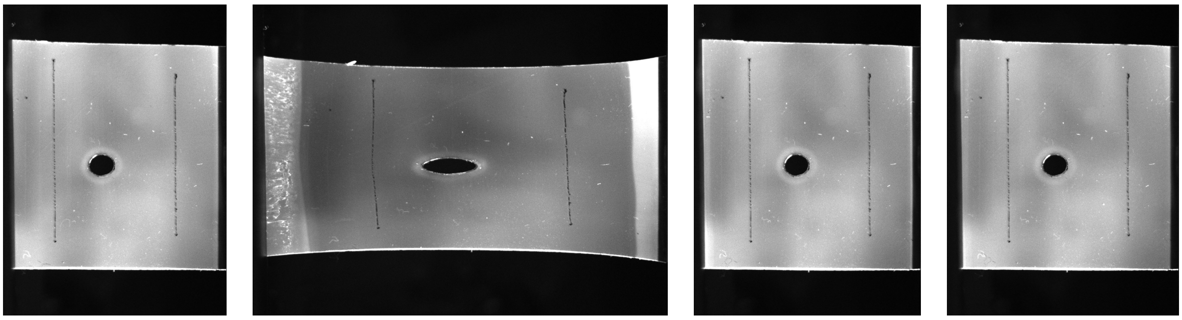
(a) (b) (c) (d)

Figure 4.4: Sample with free dispersed spiropyran in PDMS polymer matrix in its (a) Pristine state, (b) Stretched to $\varepsilon = 0.9$, (c) Immediately after unstretching, and (d) 7 minutes after unstretching

To rule out the possibility, free dispersed spiropyran is added to the PDMS polymer matrix instead of the traditional covalently bonded spiropyran. This is achieved by removing the vinyl groups attached to the spiropyran molecule (R_1 and R_2 in Fig. 2.9). This modification ensures that the mechanical stresses applied to the polymer will not be transferred to the spiropyran molecules. The effect of viscoelasticity can thus be investigated. As seen in Fig. 4.4, no fluorescence activation is seen upon stretching the sample. Also, after unstretching, no fluorescence decay is observed, thereby ruling out ”photoelasticity due to viscoelasticity” as a possible explanation for the fluorescence.

Based on the control experiments, it can be confidently concluded that the competing hypotheses are proven false, and the fluorescence observed in our sample originates from the fluorescent merocyanine molecule.

4.3. Spatial distribution of fluorescence

The problem of mapping the stress tensor over the geometry of an ”infinite plate with a hole” has been a classic problem in stress analysis since 1898 [55]. Fig. 4.5 (a) depicts Kirsch’s analytical solution that tries to capture the stress concentrations near discontinuities. Focussing on the transverse direction relative to the loading, the stress amplification is $K_t = 3$ near the hole. The stress amplification drops to $K_t \approx 1$ at a vertical distance of one hole diameter away from the hole’s edge.

This indicates that the equivalent stress at the top of the hole must be three times the equivalent stress experienced by a point away from the hole. Fig. 4.5 (b) presents experimental data showing the fluorescence intensity at the top of the hole is approximately 2450 counts, which is three times the fluorescence intensity away from the hole, which is approximately 800.

This observation confirms some qualitative correlation between the fluorescence and the equivalent stress in the material.

4.4. Activation duration of spiropyran under stress

To investigate the duration of spiropyran activation under mechanical loading, the spiropyran-embedded PDMS sample is stretched to a strain $\varepsilon = 0.9$ and the fluorescence intensities are captured for two hours post-stretching. Fig. 4.6 (a) shows the fluorescence intensity evolution at locations around the hole, specifically at the top, bottom, side and away from the hole.

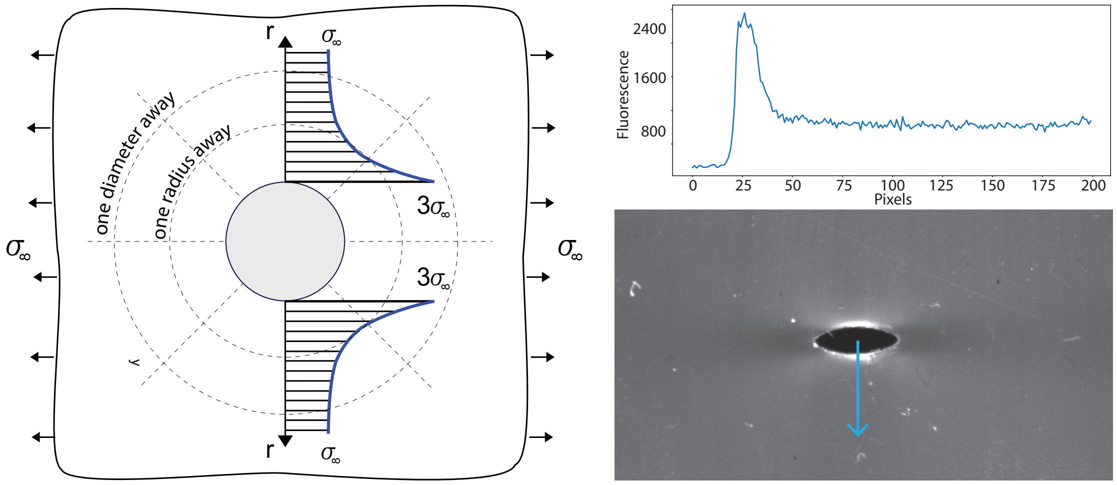

(a) (b)

Figure 4.5: (a) Schematic showing that the stress near the hole in the transverse direction is three times the nominal stress applied to the sample; Image adapted from ref. [53] (b) Plot showing the intensity near the hole in the transverse direction using a blue arrow.

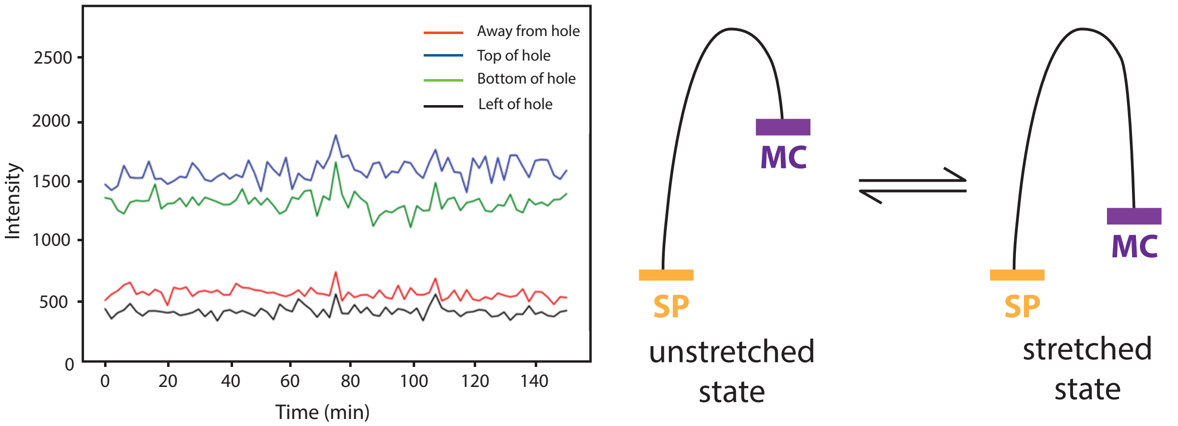

(a) (b)

Figure 4.6: (a) Intensity plot at various locations around the hole with the time elapsed since stretching (b) Schematic showing shift in energy diagram with a shift in equilibrium.

The data in the plot shows that the fluorescence intensities at these points remain constant throughout the observation period. This indicates a shift in the equilibrium between $SP \rightleftharpoons MC$, favoring the merocyanine form in the high-stress regions near the top and the bottom of the hole. Once the applied strain is released, the equilibrium again shifts back to its original state.

5

Correlating mechanics with spiropyran fluorescence

This chapter presents the key findings from the correlation phase of the thesis, focussing on the analysis of the fluorescence and decay rate time constant. The experimental data is compared and correlated with various continuum mechanics quantities predicted in the numerical simulations.

5.1. Analysis along radial lines

For a detailed comparison, pixel data at 360 radial lines centered at the hole is extracted from the experimental and the aligned simulation image. Plotting the experimental data along these radial lines against the simulation data gives a qualitative understanding of the distribution of patterns around the elliptical hole.

5.1.1. Analysis of fluorescence and von Mises stress along radial lines

Fig. 5.1 and 5.2 depict the normalized fluorescence intensity and von Mises stress as functions of the radial distance from the center of the elliptical hole, respectively. The data is hereby gathered along radial lines of angles 90°, 60°, 30°, and 0° relative to the direction of the applied strain. The normalized fluorescence intensity is obtained by dividing the fluorescence with the maximum fluorescence value along the 90° line.

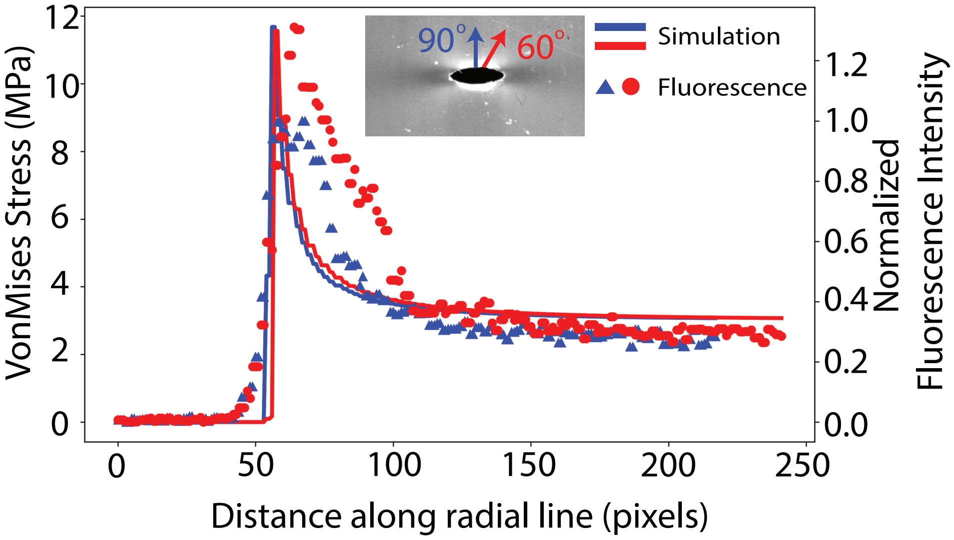

Figure 5.1: von Mises stress and fluorescence along radial lines at angles of 90° and 60° relative to the direction of applied strain.

For the 90° and 60° lines, both the von Mises stress and fluorescence peak at the edge of the hole decay exponentially away from it within a radial distance of one hole diameter.

For the 0° line, there is a noticeable dip in both von Mises stress and fluorescence intensity near the edge of the hole. This pattern aligns with the findings from Gohl et al. (2023) [44], who reported similar fluorescence behavior at specific angles around the hole.

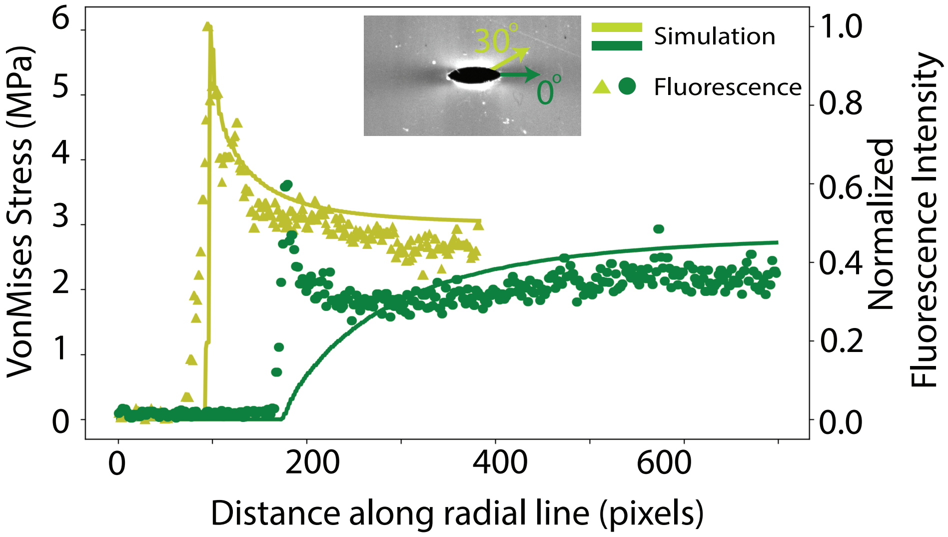

Figure 5.2: von Mises stress and fluorescence along radial lines at angles of 30° and 0° relative to the direction of applied strain.

The von Mises stress experiences sharp fluctuations near the edge of the hole, whereas the fluorescence intensity rises gradually at the edge, and declines slowly, before eventually catching up to the expected spatial decay. This discrepancy is attributed to another optical phenomenon at the hole's edge. Some of the fluorescence from the merocyanine gets captured into the bulk of the PDMS due to total internal reflection. The edge of the hole acts as a boundary, scattering this light into the surrounding air and creating a halo around the hole as seen in Fig. 4.4. The fluorescence image recorded by the camera is a superimposition of the fluorescence and the halo. This effect is evident along the 0°

line, where the expected drop in intensity has a small peak at the edge (Fig. 5.2). This explains the discrepancy between experimental and simulation spatial decay along the radial lines.

Overall, the analysis shows a strong qualitative correlation between the fluorescence and von Mises stress patterns.

5.1.2. Analysis of decay rate time constant and von Mises stress along radial lines

Fig. 5.3 and 5.4 show the decay rate time constant of the slow exponential component and von Mises stress as functions of the radial distance from the center of the elliptical hole, respectively. To imitate the above, the presented data is gathered along radial lines of angles 90°, 60°, 30°, and 0° relative to the direction of the applied strain.

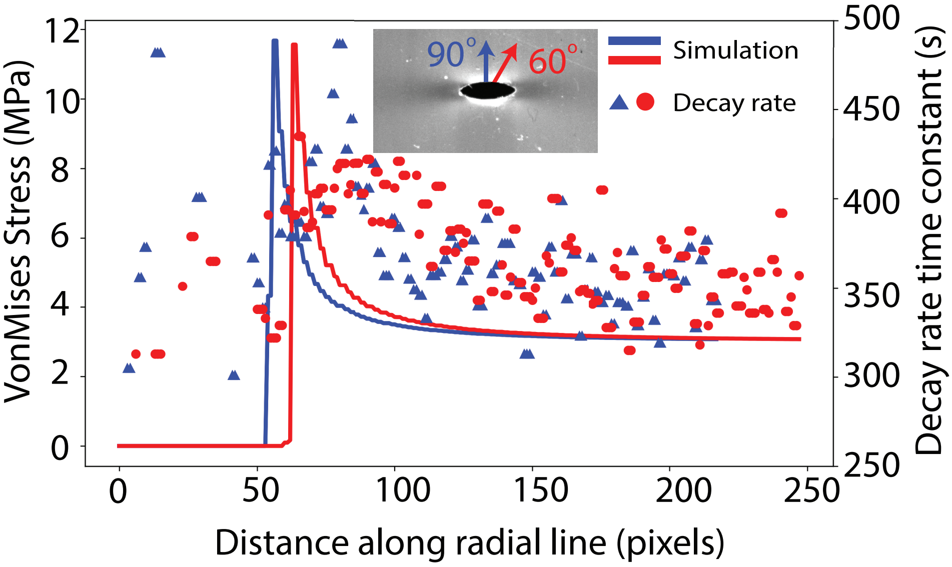

Figure 5.3: von Mises stress and decay rate time constant along radial lines at angles of 90° and 60° relative to the direction of applied strain.

The variance in the decay rate time constant along the radial lines is higher as compared to that in the fluorescence discussed in the previous section. The decay rate time constant is derived from the fluorescence measurements and is not directly measured. This intermediate step adds additional noise, which can be seen in Fig. 5.3 and 5.4. The source of this variance can be traced back to the experiment procedure and the potential ways to mitigate are discussed further in Chapter 7.

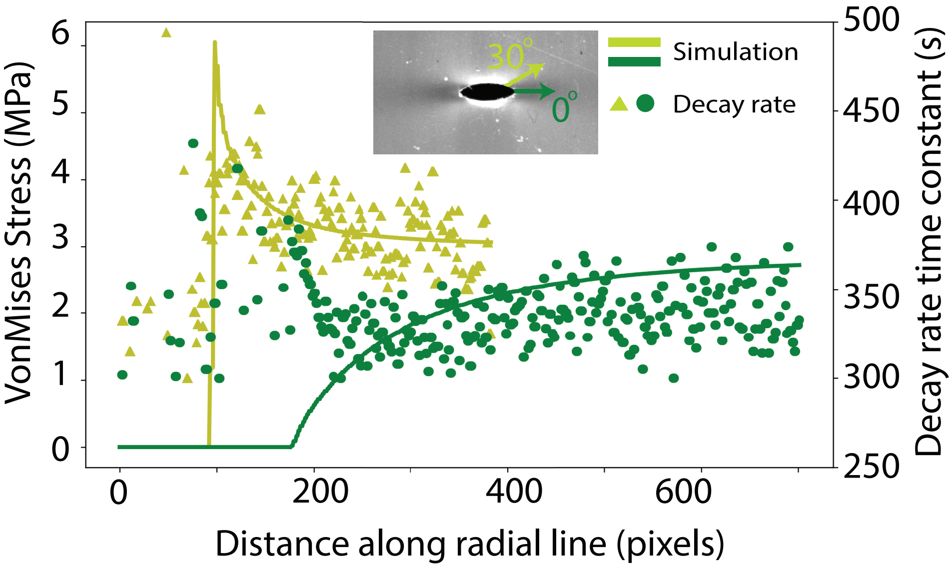

Figure 5.4: von Mises stress and decay rate time constant along radial lines at angles of 30° and 0° relative to the direction of applied strain.

For the 0° line, the decay rate time constant decreases as the distance from the edge of the hole reduces. A noticeable peak is seen very close to the edge, suggesting that merocyanine at the edge takes more time to decay back to spiropyran. However, this may possibly be due to data contamination through light scattering at the PDMS-air interface.

Despite the noise, there is an observable, but moderate correlation between the von Mises stress and the slow component of the decay. The decay rate time constant follows patterns similar to the von Mises stress with more variance than the fluorescence.

5.2. Correlation heatmaps

This section outlines the correlation of various continuum mechanics quantities with the experimental data along the radial lines. Mechanical tensors like the Deformation gradient tensor $\mathbf{F}$ and the First Piola-Kirchoff stress tensor $\mathbf{P}$ are extracted from COMSOL for each pixel. The other continuum mechanics quantities like the right Cauchy-Green deformation tensor $\mathbf{C}$, Green-Lagrange strain tensor $\mathbf{E}$, the Cauchy Stress $\boldsymbol{\sigma}$ and their invariants and eigenvalues are computed using existing relations.

Pearson's correlation coefficient is used as the measure of correlation in the thesis. Pearson's correlation coefficient r measures the linear correlation between two sets of data, X and Y. It is defined mathematically as:

$$r = \frac{\sum_i^n (X_i - \bar{X})(Y_i - \bar{Y})}{\sqrt{\sum_i^n (X_i - \bar{X})^2 \sum_i^n (Y_i - \bar{Y})^2}}, \quad \text{with } r \in [-1, 1]. \tag{5.1}$$

, where $\bar{X}$ and $\bar{Y}$ are the mean of variables X and Y. The coefficient value $r \in [-1, 1]$ can then be interpreted as follows:

1. A correlation coefficient of 1 indicates a perfect positive linear relationship where increases in X are associated with proportional increases in Y.
2. A correlation coefficient of -1 signifies a perfect negative linear relationship, where increases in X are associated with proportional decreases in Y.
3. A correlation coefficient of 0 indicates no linear correlation between the variables.

5.2.1. Correlation between fluorescence and simulated quantites

Of the many quantities, their invariants and eigenvalues correlated with the fluorescence, the four quantities with the highest correlation are visualized in Fig. 5.5, respectively.

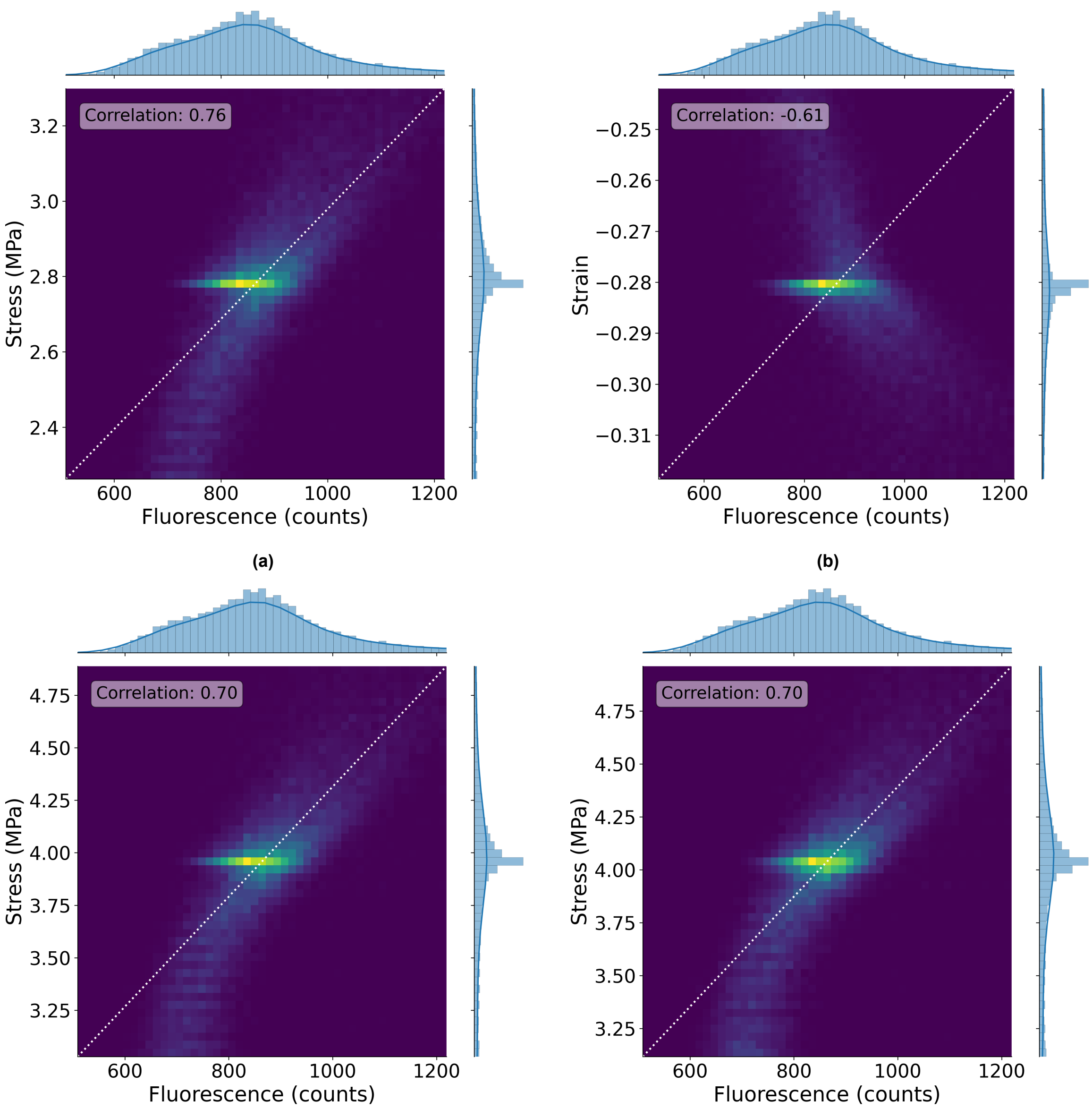

(a) **(b)** **(c)** **(d)**

Figure 5.5: Heatmap and the correlation coefficients for (a) Difference between maximum and minimum eigenvalues of the First Piola-Kirchoff stress tensor $\mathbf{P}$, (b) second invariant of the Green-Lagrange strain tensor $\mathbf{E}$, (c) von Mises stress σ_{VM}, and (d)maximum eigenvalue of Cauchy stress $\boldsymbol{\sigma}$.

It is observed that most quantities have a positive correlation with fluorescence. However, exceptions are observed with the second invariants of the right Cauchy-Green deformation tensor $\mathbf{C}$ and Green-Lagrange strain $\mathbf{E}$ (Fig. 5.5 (b)), which display a strong negative correlation.

The strongest positive correlation of $r = 0.76$ is noted between the eigenvalues of the First Piola-Kirchoff stress tensor $(\mathbf{P})$ with the fluorescence. In practice, correlation coefficients between $r = 0.6 - 0.8$ are considered strong correlations [56].

5.2.2. Correlation between decay rate time constant and simulated quantities

The quantities with the four strongest correlations with the decay rate time constant are visualized below in Fig. 5.6.

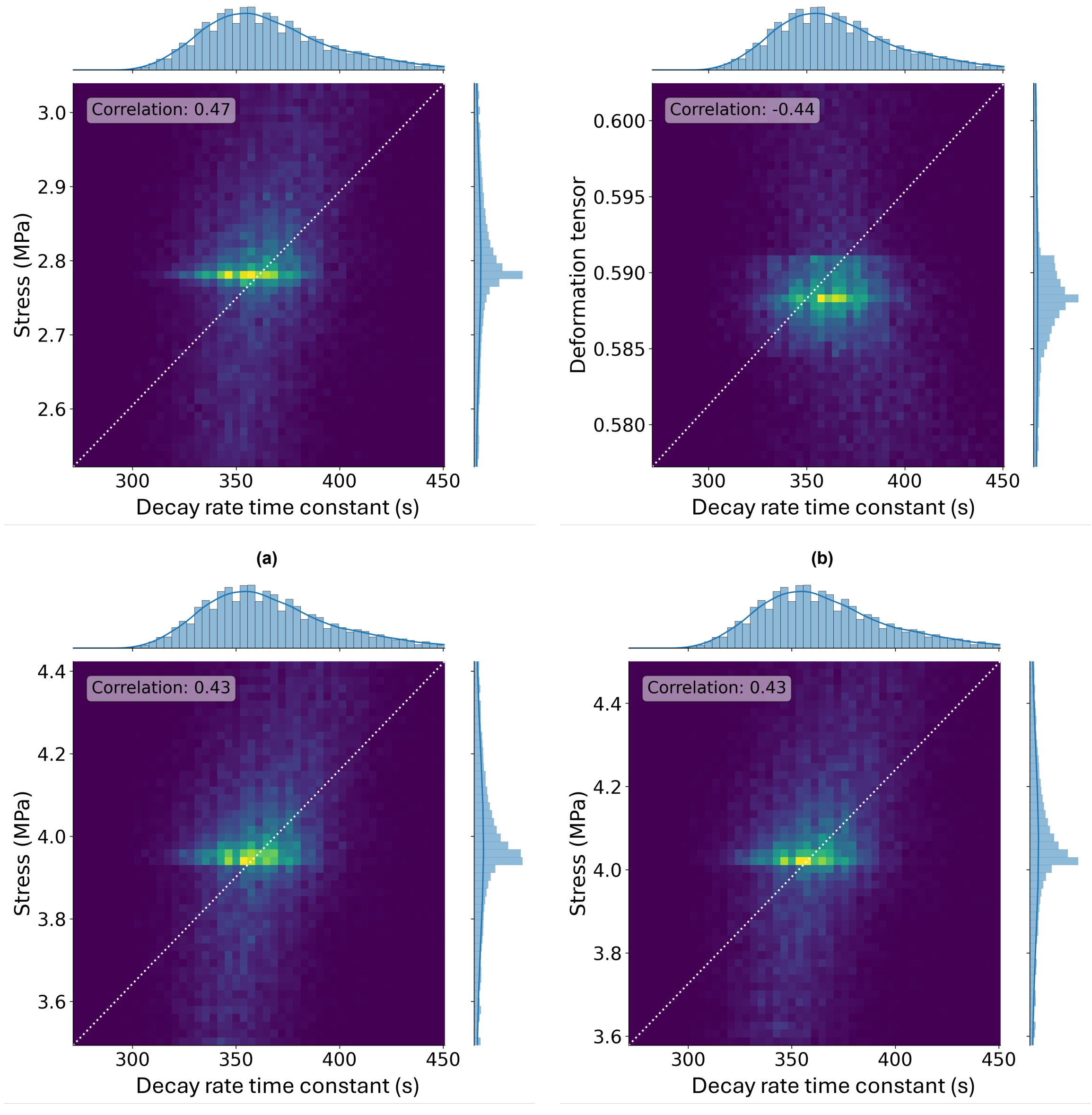

(a) **(b)**

(c) **(d)**

Figure 5.6: Decay rate time constant and the correlation coefficients for: (a) Difference between maximum and minimum eigenvalues of the First Piola-Kirchoff stress tensor $\mathbf{P}$, (b) second invariant of the right Cauchy-Green deformation tensor $\mathbf{C}$, (c) von Mises stress σ_{VM}, and (d) maximum eigenvalue of Cauchy stress $\boldsymbol{\sigma}$.

The strongest correlation noted between the decay rate time constant and the quantities is $r = 0.47$ when correlating with the difference in the eigenvalues of the First Piola-Kirchoff stress tensor $\mathbf{P}$. Correlations of $r = 0.4 - 0.6$ are considered moderate [56]. The moderate correlations can be attributed to the noisiness of the decay rate time constant, which is a derived quantity.

The comprehensive list of all the tested quantities is provided in Tables D.2, D.3 and D.4 in Appendix D.

6

Conclusions

The primary aim of this research is to establish correlations between various measured and simulated quantities while understanding these relationships from a phenomenological perspective. Along the way, many other valuable observations were made during the research process, which are summarized in this chapter.

The fluorescence and decay rate time constants of spiropyran-embedded PDMS samples were recorded in dark-room experiments. The decay rate time constant is defined as the time constant of the exponential decay observed after UV excitation of the stretched sample. It was confirmed that the image recorded is indeed the merocyanine fluorescence, by developing alternate hypotheses and ruling them out.

A significant finding from the study is the activation of spiropyran under mechanical stress, which is found to change the SP $\rightleftharpoons$ MC equilibrium significantly. This change is enough to make spatial locations under high stress favor the merocyanine form. Thus, the activation stays for an extended period of time in the stretched state, instead of decaying back in a few minutes.

To get the material properties for the simulation, uniaxial tensile tests were performed on dogbone samples. The stress-strain curve was parametrically fitted to the Yeoh hyperelastic material model. This material model facilitates the numerical simulations and various continuum mechanics properties were derived, which are then correlated with the fluorescence and decay rate time constant.

Finally answering the research questions posed in Chapter 1, a strong correlation is noted between the fluorescence intensity and certain simulated quantities, whereas a moderate correlation is observed when correlating with the decay rate time constant. The most notable correlation is that of the difference between the eigenvalues of the First Piola-Kirchoff stress tensor $\mathbf{P}$ and the fluorescence, which correlate with a strong correlation coefficient of $r = 0.76$. When correlating quantities with the decay rate time constant, the same quantity had a moderate correlation of $r = 0.47$. This is expected since the decay rate time constant is a derived quantity and not directly measured, which inherently introduces additional noise to the analysis.

7

Recommendations

The thesis observations and conclusions help shed light on connecting two disconnected fields of optics and mechanics with a focus on stress mapping. However, like every research, there is always room for improvements and extensions. This chapter is divided into two sections - possible improvements and future advancements of the research work.

7.1. Possible improvements

After performing the current experiments, a few possible improvements in the experimental procedure and material modeling have been identified.

7.1.1. Sample slippage during experiments

During the experiments, minimal slippage of the sample was observed, approximately 0.5-1 mm corresponding to a strain $\varepsilon = 1$. Due to this slippage, the effective length of the sample increases, and thereby the effective strain applied also reduces.

To solve this problem, two solutions can be implemented:

1. Account for the increased length by modifying the conditions within the simulation to reflect the actual experimental setup.
2. Design and implement improved clamps to minimize or eliminate slippage from the experiment.

7.1.2. Light scattering at the edge of the hole

Some of the fluorescence emitted by the merocyanine molecules gets trapped in the bulk of the polymer due to total internal reflection. When this light passes through the hole, it encounters a PDMS-air boundary, which scatters the light to be captured by the camera. This causes a halo formation around the hole, as seen in Fig. 4.4.

This halo is a permanent presence in the images, superimposing with the fluorescence data near the edge of the hole. The issue has been explained in detail in Chapter 5. To solve for the halo discrepancy in our activation results, two approaches can be followed to separate the activation fluorescence.

1. Capture an image of the halo using free dispersed spiropyran, as done in section 4.2 under the same concentration of spiropyran and other environmental conditions to subtract it from the fluorescence measurements in postprocessing.
2. Ignore the data for a few pixels near the edge of the hole and correlate the rest of the data.
3. Modify the PDMS boundary by filling the hole with water. This changes the PDMS-air boundary which has refractive indices of 1.43 and 1, to a PDMS-water boundary with refractive indices of

1.43 and 1.33. This reduces the critical angle and passively controls the scattering to a great extent.

7.1.3. Shadow formation

As seen in Fig. 4.1 (b), a shadow is formed due to the hole either towards the top of the hole or towards the bottom of the hole. This is caused by the side illumination of the sample by a diffused point-light source.

To eliminate this shadow formation, the implementation of a ring light illuminator is recommended. A ring light illuminator ensures that the light is incident from the top and thus no shadow is formed.

7.1.4. Enhancing material model accuracy

The current material model for the spiropyran-embedded PDMS using a 10:1 ratio of PDMS base to curing agent has been primarily generated through uniaxial tensile testing. This test does not include any transverse movement of the sample influenced by the Poisson's ratio. The shear motion is also not modeled by this test. In an ideal situation, to model the material, two to three different tests - biaxial tension test, shear test, etc. must be performed and the data must be fitted to all test curves simultaneously.

7.1.5. Reducing the variance in the decay rate time constant image

Significant variance and noise are observed in the decay rate time constant image. The reasons could be attributed to the following factors:

1. The halo effects around the hole due to light scattering could cause variation in the decay time constant data around the hole.
2. Overexposure to UV light can cause photodegradation of light-sensitive molecules such as merocyanine. This permanent deactivation process might not be uniform across the sample, especially if the UV exposure varies across different areas. If more merocyanine molecules are deactivated in certain regions than others, there will be inconsistencies in the active versus deactivated molecules across the sample. This variation leads to differences in how much light is emitted upon subsequent excitations, thereby increasing the noise and variance in the decay rate time constant images.
3. A high intensity of green light, which is used to visualize the pristine sample can cause merocyanine molecules to get deactivated. This can especially happen since the green light illuminates the sample throughout the period of one hour of stress relaxation.
4. A high exposure time set increases the amount of light that enters the camera but it also increases the noise in the image.

The solution for the latter three factors is to use the least amount of UV and green light possible during the experiments and to keep the exposure time as short as possible.

To increase the contrast in the decay rate time constant image, better tuning of the duration of UV light activation is required alongside tuning of the time after which the fast decay subsides and only slow decay is recorded.

7.2. Future extensions to the current study

In this study, a phenomenological perspective of the correlation between mechanics and chemistry of mechanophores is provided. This gives a preliminary idea of how these two fields are related in the context of mechanosensing. Preliminary insights from these analyses suggest that the relationship between mechanical stress and chemical responses in mechanophores is strong.

The correlation coefficient investigates linear relationships between quantities. Systemic solvers such as symbolic regression, sparse regression, and funsearch algorithms are capable of identifying and quantifying relationships — both linear and nonlinear — between fluorescence and continuum mechanics quantities. The insights of this study can be used as guiding directions for these solvers to enhance our ability to model the behavior of mechanosensors.

Expanding the experimental scope to research dynamic tests will increase the complexity of the experiments by one level. During the dynamic motion of stretching, while the spiropyran is being activated to merocyanine, at the same time, merocyanine is also decaying to spiropyran. A study of the fundamentals of these two kinetics can lead to a basic understanding of the dynamic behavior of the mechanophore spiropyran.

This thesis has highlighted a finding that stretching influences the SP-MC (spiropyran to merocyanine) equilibrium, shifting it in a way that favors the merocyanine form in regions experiencing mechanical stress. However, the underlying chemistry and kinetics driving this equilibrium shift are not properly understood. Investing in research to explore the kinetics behind the SP-MC equilibrium shift could help test the limits of the chemical phenomenon. This could pave the way to developing live stress visualization methods for experimental validation and demonstrations.

7.2.1. Future areas of application and impact

This research can be extended and applied to numerous possible technological areas. Assuming that the stress-optic correlations are developed further, in the future, probably the next generation of mechanoresponsive materials can have impacts in the following areas:

1. **Destructive testing:** Mechanoresponsive materials can be applied to destructive testing of mechanical components for estimating stress contour while real-time material failure takes place. Material deformation and failure can be observed from high-resolution optical cameras to observe fluorescence intensities and hence estimate stress tensors. This can be applied to vehicular crash testing.
2. **Non-destructive testing:** In systems exhibiting large geometrical nonlinearities, mechanoresponsive materials can be deployed complementary to the computationally expensive FEA solvers.
3. **Experimentation safety:**Mechanoresponsive materials can also be utilized for validating experimental test setups that transmit and absorb static or dynamic loads. When certain fluorescence intensities are observed during experimentations, potential stress failure points can be identified and the experiment can be stopped to prevent damage.
4. **Impact on society:** People can use mechanosensors in day-to-day applications to intuit when a material ventures near its breaking limits. This increases safety in the handling of fragile and expensive components.
5. **Impact on sustainability:** Apart from posing several challenges in computational efficiencies, complex FEM-based solvers require supercomputers to run for long hours in large corporations, thereby increasing their carbon footprints. Mechanoresponsive materials can complement FEM in such nonlinear models and hence mediate the above problem. This combined with the advantage of less breakage of critical structures and materials can help reduce environmental degradation and foster sustainability.

References

[1] William D Callister Jr and David G Rethwisch. *Callister's materials science and engineering*. John Wiley & Sons, 2020.

[2] Seongwoo Woo. "Reliability Disasters and Its Assessment Significance." en. In: *Reliability Design of Mechanical Systems*. Cham: Springer International Publishing, 2017, pp. 7–34. DOI: `10.1007/978-3-319-50829-0_2`.

[3] Russell C Hibbeler. *Engineering mechanics. Statics/-12th*. Prentice Hall, 2010.

[4] K Eareast. *Photo by K Eareast on unsplash*. Nov. 2018. URL: `https://unsplash.com/photos/gray-airplane-window-G_1k_sh96HU`.

[5] *Why do airplanes have rounded windows?* June 2011. URL: `https://aviation.stackexchange.com/questions/15779/why-do-airplanes-have-rounded-windows`.

[6] Amalina Binte Ebrahim Attia et al. "Clinical noninvasive imaging and spectroscopic tools for dermatological applications: Review of recent progress." In: *Translational Biophotonics* 2.4 (2020), e202000010.

[7] Bernard Dennis Cullity. *Elements of X-ray Diffraction*. Addison-Wesley Publishing, 1956.

[8] P Stanley. "Beginnings and early development of thermoelastic stress analysis." In: *Strain* 44.4 (2008), pp. 285–297.

[9] R. V. South-well. "A Treatise on Photo-Elasticity. By E. G. Coker and L. N. G. Filon Pp. xviii, 720. 50s. 1931. (Cambridge University Press)." In: *The Mathematical Gazette* 16.220 (1932), pp. 277–279. DOI: `10.2307/3605934`.

[10] K Ramesh and G Lewis. "Digital photoelasticity: advanced techniques and applications." In: *Appl. Mech. Rev.* 55.4 (2002), B69–B71.

[11] Jan Cernosek. "Three-dimensional photoelasticity by stress freezing: Paper reviews the principles of three-dimensional photoelasticity and describes extensive research and development work performed to make three-dimensional photoelasticity more competitive and cost effective." In: *Experimental Mechanics* 20 (1980), pp. 417–426.

[12] Saravana Bavan and Garje Mohan Kumar. "Finite Element Analysis of a Natural Fiber (Maize) Composite Beam." In: *Journal of Engineering* 2013 (Jan. 2013). DOI: `10.1155/2013/450381`.

[13] MC Watson and TW Clyne. "The use of single fibre pushout testing to explore interfacial mechanics in SiC monofilament-reinforced Ti—II. Application of the test to composite material." In: *Acta metallurgica et materialia* 40.1 (1992), pp. 141–148.

[14] URL: `https://www.britannica.com/science/double-refraction`.

[15] URL: `https://www.olympus-lifescience.com/en/microscope-resource/primer/lightandcolor/birefringence/`.

[16] Theodore C Oakberg. "Relative variation of stress-optic coefficient with wavelength in fused silica and calcium fluoride." In: *Polarization: Measurement, Analysis, and Remote Sensing II*. Vol. 3754. SPIE. 1999, pp. 226–234.

[17] Rajiv Kohli. "Developments in imaging and analysis techniques for micro-and nanosize particles and surface features." In: *Developments in surface contamination and cleaning*. Elsevier, 2012, pp. 215–306.

[18] MR Ayatollahi and M Nejati. "Experimental evaluation of stress field around the sharp notches using photoelasticity." In: *Materials & Design* 32.2 (2011), pp. 561–569.

[19] Ferran Pujol-Vila et al. "Soft optomechanical systems for sensing, modulation, and Actuation." In: *Advanced Functional Materials* 33.14 (2023), p. 2213109.

[20] Naomi Deneke, Mitchell L Rencheck, and Chelsea S Davis. “An engineer’s introduction to mechanophores.” In: *Soft Matter* 16.27 (2020), pp. 6230–6252.

[21] Jess M Clough et al. “Covalent bond scission in the Mullins effect of a filled elastomer: real-time visualization with mechanoluminescence.” In: *Advanced Functional Materials* 26.48 (2016), pp. 9063–9074.

[22] Jianzhu Ju et al. “Real-Time Early Detection of Crack Propagation Precursors in Delayed Fracture of Soft Elastomers.” In: *Physical Review X* 13.2 (2023), p. 021030.

[23] Stephanie L. Potisek et al. “Mechanophore-Linked Addition Polymers.” In: *Journal of the American Chemical Society* 129.45 (2007), pp. 13808–13809. DOI: `10.1021/ja076189x`.

[24] Christopher P. Kabb et al. “Anthracene-based mechanophores for compression-activated fluorescence in polymeric networks.” In: *Chemical Science* 10 (2019). Edge Article, pp. 7702–7708. DOI: `10.1039/C9SC02487E`.

[25] Naomi Deneke, Mitchell L. Rencheck, and Chelsea S. Davis. “An engineer’s introduction to mechanophores.” In: *Soft Matter* 16 (2020). Review Article, pp. 6230–6252. DOI: `10.1039/D0SM00465K`.

[26] Qiming Wang et al. “Cephalopod-inspired design of electro-mechano-chemically responsive elastomers for on-demand fluorescent patterning.” In: *Nature communications* 5.1 (2014), p. 4899.

[27] Brittany A. Versaw et al. “Harnessing the Power of Force: Development of Mechanophores for Molecular Release.” In: *Journal of the American Chemical Society* 143.51 (Dec. 29, 2021), pp. 21461–21473. DOI: `10.1021/jacs.1c11868`. URL: `https://pubs.acs.org/doi/10.1021/jacs.1c11868`.

[28] Mohammad A. Ghanem, Anjan Bedi, Rami Behrou, et al. “The role of polymer mechanochemistry in responsive materials and additive manufacturing.” In: *Nature Reviews Materials* 6 (2021), pp. 84–98. DOI: `10.1038/s41578-020-00249-w`. URL: `https://doi-org.tudelft.idm.oclc.org/10.1038/s41578-020-00249-w`.

[29] Meng Li et al. “Let spiropyran help polymers feel force!” In: *Progress in Polymer Science* 79 (2018), pp. 26–39.

[30] Angela B Grommet, Lucia M Lee, and Rafal Klajn. “Molecular photoswitching in confined spaces.” In: *Accounts of Chemical Research* 53.11 (2020), pp. 2600–2610.

[31] Yuval Vidavsky et al. “Enabling Room-Temperature Mechanochromic Activation in a Glassy Polymer: Synthesis and Characterization of Spiropyran Polycarbonate.” In: *Journal of the American Chemical Society* 141.25 (2019), pp. 10060–10067. DOI: `10.1021/jacs.9b04229`.

[32] Richard Janissen and Georgy A Filonenko. “Mechanochemistry of spiropyran under internal stresses of a glassy polymer.” In: *Journal of the American Chemical Society* 144.50 (2022), pp. 23198–23204.

[33] Stephanie L Potisek et al. “Mechanophore-linked addition polymers.” In: *Journal of the American Chemical Society* 129.45 (2007), pp. 13808–13809.

[34] Tae Ann Kim et al. “Effect of mechanical stress on spiropyran-merocyanine reaction kinetics in a thermoplastic polymer.” In: *ACS Macro letters* 5.12 (2016), pp. 1312–1316.

[35] Kunal Prakash, Priya Ranjan Sahoo, and Satish Kumar. “A substituted spiropyran for highly sensitive and selective colorimetric detection of cyanide ions.” In: *Sensors and Actuators B: Chemical* 237 (2016), pp. 856–864.

[36] Yuval Vidavsky et al. “Enabling room-temperature mechanochromic activation in a glassy polymer: synthesis and characterization of spiropyran polycarbonate.” In: *Journal of the American Chemical Society* 141.25 (2019), pp. 10060–10067.

[37] Brett A Beiermann et al. “Environmental effects on mechanochemical activation of spiropyran in linear PMMA.” In: *Journal of Materials Chemistry* 21.23 (2011), pp. 8443–8447.

[38] Brett A Beiermann et al. “The effect of polymer chain alignment and relaxation on force-induced chemical reactions in an elastomer.” In: *Advanced Functional Materials* 24.11 (2014), pp. 1529–1537.

[39] Gregory R Gossweiler, Tatiana B Kouznetsova, and Stephen L Craig. “Force-rate characterization of two spiropyran-based molecular force probes.” In: *Journal of the American Chemical Society* 137.19 (2015), pp. 6148–6151.

[40] Brett A Beiermann et al. “Role of mechanophore orientation in mechanochemical reactions.” In: *ACS Macro Letters* 1.1 (2012), pp. 163–166.

[41] Yangju Lin, Tatiana B Kouznetsova, and Stephen L Craig. “A latent mechanoacid for time-stamped mechanochromism and chemical signaling in polymeric materials.” In: *Journal of the American Chemical Society* 142.1 (2019), pp. 99–103.

[42] Yinjun Chen et al. “From force-responsive molecules to quantifying and mapping stresses in soft materials.” In: *Science advances* 6.20 (2020), eaaz5093.

[43] Etienne Ducrot et al. “Toughening elastomers with sacrificial bonds and watching them break.” In: *Science* 344.6180 (2014), pp. 186–189.

[44] Jared A Gohl et al. “Stress quantification in a composite matrix via mechanophores.” In: *Frontiers in Soft Matter* 3 (2023), p. 1125163.

[45] Chelsea S Davis et al. “Activation of Mechanophores in a Thermoset Matrix by Instrumented Scratch.” In: *ACS Applied Materials & Interfaces* 13.46 (2021), pp. 55498–55506.

[46] Douglas A Davis et al. “Force-induced activation of covalent bonds in mechanoresponsive polymeric materials.” In: *Nature* 459.7243 (2009), pp. 68–72.

[47] Tae Ann Kim et al. “Mechanical reactivity of two different spiropyran mechanophores in polydimethylsiloxane.” In: *Macromolecules* 51.22 (2018), pp. 9177–9183.

[48] Cassandra M Kingsbury et al. “Shear activation of mechanophore-crosslinked polymers.” In: *Journal of Materials Chemistry* 21.23 (2011), pp. 8381–8388.

[49] Asha-Dee N Celestine, Nancy R Sottos, and Scott R White. “Strain and stress mapping by mechanochemical activation of spiropyran in poly (methyl methacrylate).” In: *Strain* 55.3 (2019), e12310.

[50] Asha-Dee N Celestine et al. “Fracture-induced activation in mechanophore-linked, rubber toughened PMMA.” In: *Polymer* 55.16 (2014), pp. 4164–4171.

[51] Corissa K Lee et al. “Solvent swelling activation of a mechanophore in a polymer network.” In: *Macromolecules* 47.8 (2014), pp. 2690–2694.

[52] Zhiyong Xia et al. “‘Seeing’strain in soft materials.” In: *Molecules* 24.3 (2019), p. 542.

[53] Bob McGinty. URL: `https://www.fracturemechanics.org/hole.html`.

[54] Ruben Ramos-Garcia et al. “Polarization dependence on the holographic recording in spiropyran-doped polymers.” In: *Optical and Quantum Electronics* 35 (May 2003), pp. 641–650. DOI: `10.1023/A:1023964804048`.

[55] Vladimir Andreev and Nikita Tsybin. “The Inhomogeneous Plate with a Hole: Kirsch’s Problem.” In: *Procedia Engineering* 91 (Dec. 2014). DOI: `10.1016/j.proeng.2014.12.006`.

[56] Haldun Akoglu. “User’s guide to correlation coefficients.” In: *Turkish journal of emergency medicine* 18.3 (2018), pp. 91–93.

[57] URL: `https://www.futek.com/store/load-cells/s-beam-load-cells/miniature-s-beam-LSB201/QSH02033`.

A

Appendix A - Experimental setup and support software

This appendix provides an overview of the experimental setup used in this thesis, with additional information and detailed descriptions of the components used. The supporting software capabilities developed for controlled stage movement, force and displacement data capture, and image postprocessing using a GUI are explained in detail.

A.1. Linear stage

The core component of the experimental setup is the linear stage, X-LRT0250HL-AE53C from Zaber Technologies, which is chosen for its displacement-controlled motion capabilities required for the tensile test. The stage is selected on the basis of a list of requirements such as resolution in displacement and peak thrust. Table A.1 lists the requirements and compares them to the performance parameters of the linear stage, showing the superior capabilities of the stage.

Table A.1: Parameters for selection of linear stage

Parameter	**Requirement**	**Linear stage specifications**
Displacement step size	100 $\mu\mathrm{m}$	1.2 $\mu\mathrm{m}$
Displacement range	100 mm	250 mm
Velocity range	0.01 - 5 $\mathrm{mm\,s^{-1}}$	0.000239 - 240 $\mathrm{mm\,s^{-1}}$
Peak thrust	100 N	1200 N

A.2. Peripherals and stage motion

Fig. A.1 shows a comprehensive view of the uniaxial tensile tester setup, illustrating the major components and relevant electronics.

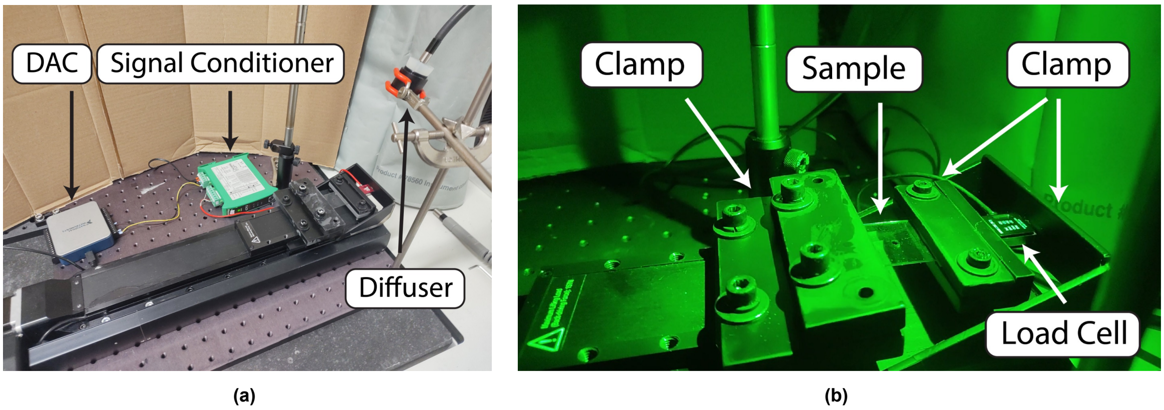

Figure A.1: Experimental setup

The linear stage's motion is controlled through a set of instructions that are stored in a stream and sent to the stage as a package. The position of the stage is recorded by a Linear Analog Encoder and transmitted back to the computer. The code used for stage control and position data acquisition is available via a GitHub repository that can be accessed via the link in Appendix D.

A.3. Load cell and force data acquisition

A 200 N analog load cell, Futek LSB-201 is the core hardware for the force acquisition system. Being an analog load cell, there is no limit to the resolution of the force measured, providing more accurate force data.

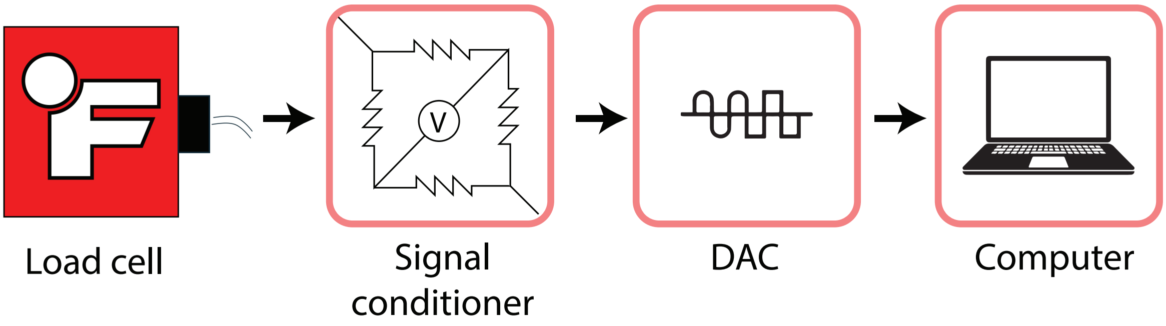

Figure A.2: Schematic of the force data acquisition timeline.

To process the load cell's output, the signal is passed through a signal conditioner. The signal conditioner is essentially a Wheatstone bridge that amplifies the voltage output of the load cell. The signal then passes through a Digital-to-Analog converter (DAC), converting it to a digital format for computer analysis. The resolution of the 12-bit DAC limits the entire range of 0-200 N force to be divided into 4096 steps. Thus, the force resolution of this system is 0.05 N.

A.3.1. Data acquisition LabVIEW project

In this thesis, LabVIEW software was used to implement the force acquisition of system measurements. The software's front panel is designed to allow adjustment of the loop time, a force offset, and real-time force visualization.

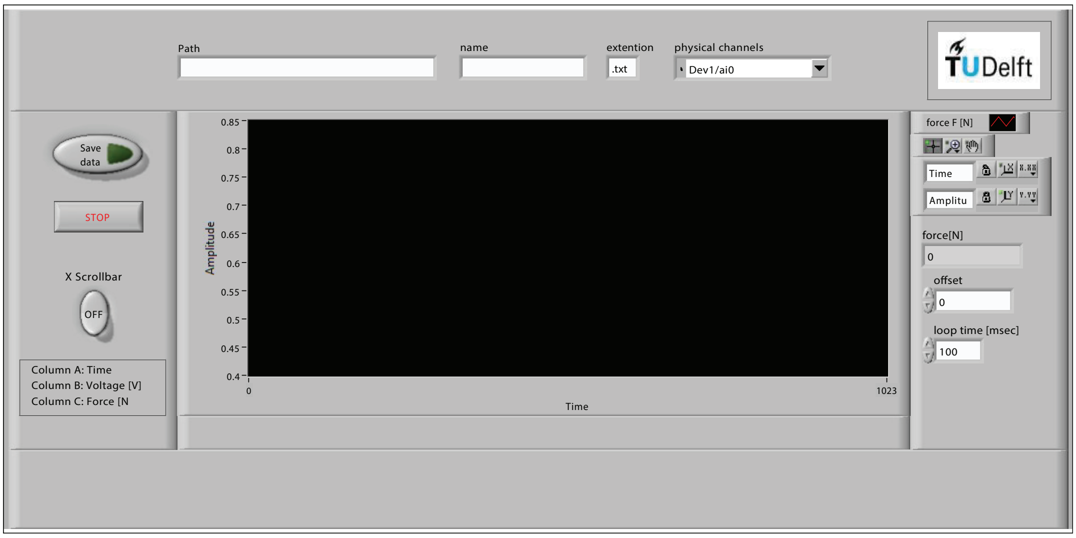

extention: .txt

physical channels: Dev1/ai0

force[N]: 0

offset: 0

loop time [msec]: 100

Column A: Time
Column B: Voltage [V]
Column C: Force [N

Figure A.3: Front panel of the LabVIEW project

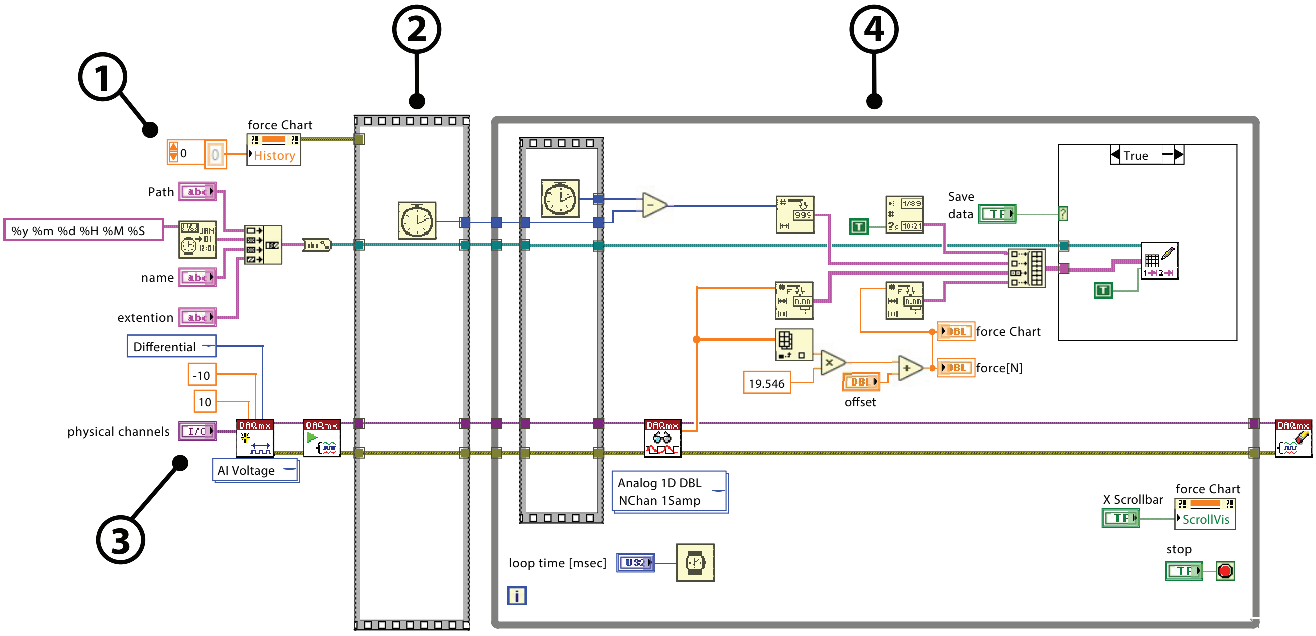

Figure A.4: Block diagram of the LabVIEW project

The design of the LabVIEW block diagram is inspired by a force acquisition project by J. Brenkman (Mechanical Engineering, TU Delft). The block diagram is structured into 4 sections.

1. **Section 1** manages the front panel connections and allows user inputs like sampling time and storage path to the program's logic.
2. **Section 2** records the start of data acquisition. This timer is used to calculate the elapsed time.
3. **Section 3** captures the voltage data from the physical channels and passes it through the DAC, thus preparing it for further calculations.
4. **Section 4** converts the processed voltage data into force measurements using a pre-calculated calibration parameter. It then converts this data into strings for data logging in spreadsheet format.

The entire LabVIEW project is available on GitHub. Access details are provided as a link in Appendix D.

A.4. Image processing software

To simplify and streamline the analysis of time decay in the fluorescence data from Experimental Approach 2, a Graphical User Interface (GUI) was developed using Python. The GUI has the following features:

1. Allows users to view, zoom, and apply contrast on the image stack.
2. To perform various background corrections on the image stack.
3. Clickable images that generate the intensity vs time plot and fit an exponential decay model to the pixel data.
4. Create a heatmap of the time constant of exponential decay.
5. Visualize the heatmap through various Lookup Tables (LUT) and save the .tif image.

The GUI is divided into The Raw Image Section, Background-corrected Image Section, and Time Decay Heatmap Section. Fig. A.5, A.6, and A.7 show the GUI sections with their working components.

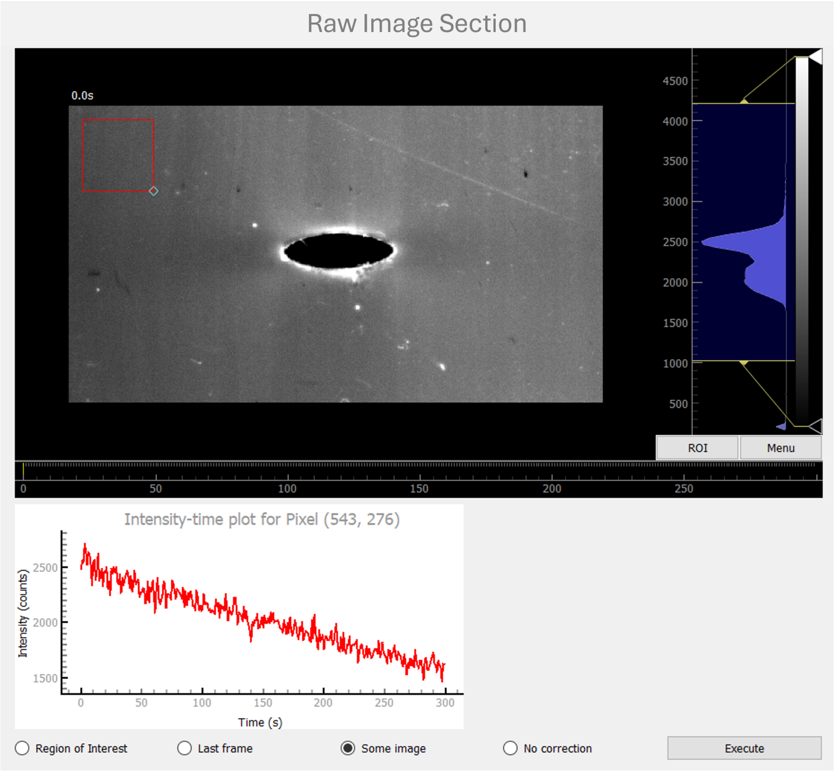

○ Region of Interest ○ Last frame ● Some image ○ No correction

Figure A.5: Raw image section of the GUI

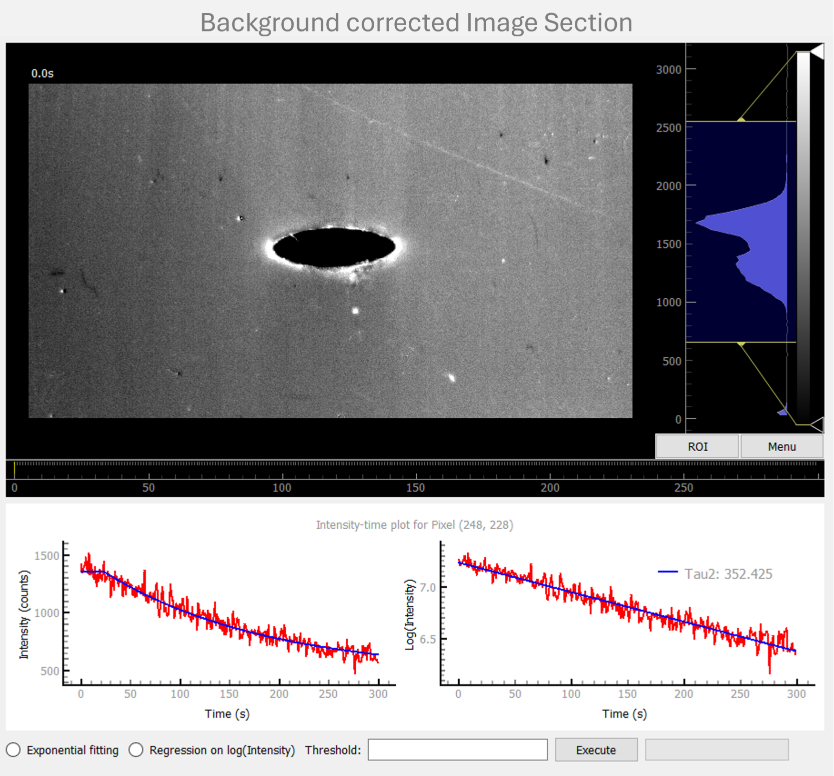

Figure A.6: Background-corrected image section of the GUI.

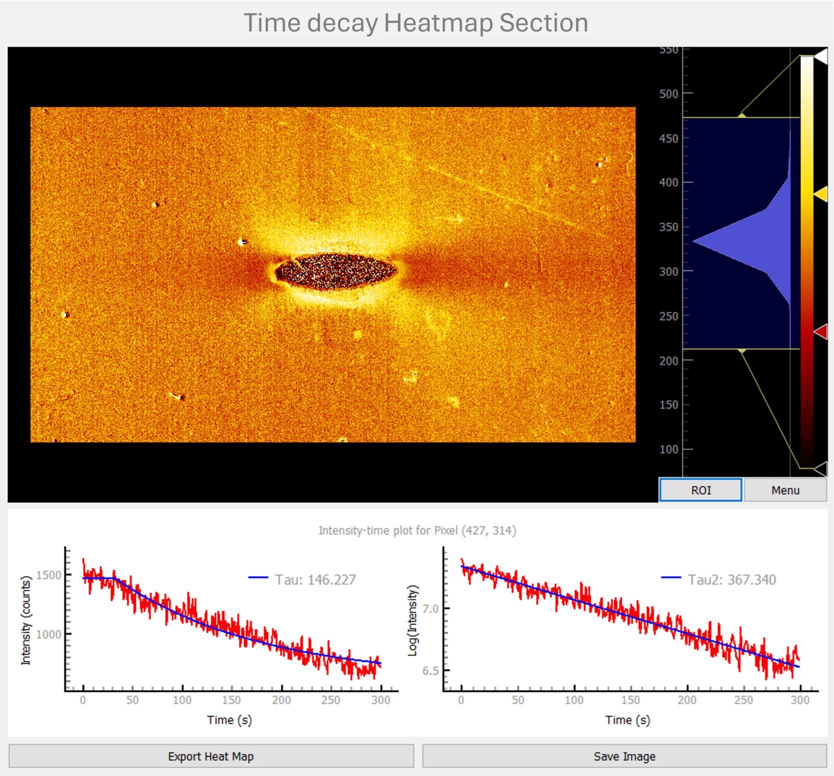

Figure A.7: Time decay heatmap section of the GUI.

A.5. Mold design for sample curing

During the course of the thesis, two types of samples are prepared - A plate-with-a-hole sample and a Dogbone sample.

For the main experiments involving fluorescence imaging, a plate-with-a-hole sample of thickness 1 mm is molded using an aluminum mold, which was finely sanded with a series of progressively finer sandpapers (P180 to P2000). To achieve a mirror finish, an alumina paste with a particle size of 10 $\mu\mathrm{m}$ is applied. The hole is cast into the mold to avoid stress concentrations that might arise from hole punching.

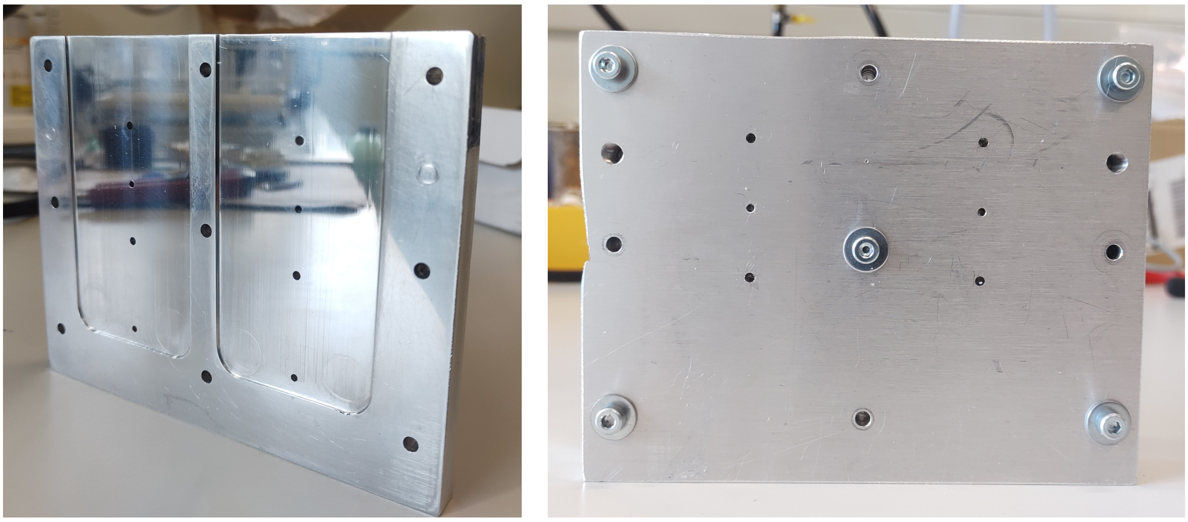
(a) (b)

Figure A.8: Aluminium mold cast for sample curing

An Acrylonitrile Butadiene Styrene (ABS) mold is prepared for curing dogbone samples, following a similar sanding process to ensure the smoothness of the sample.

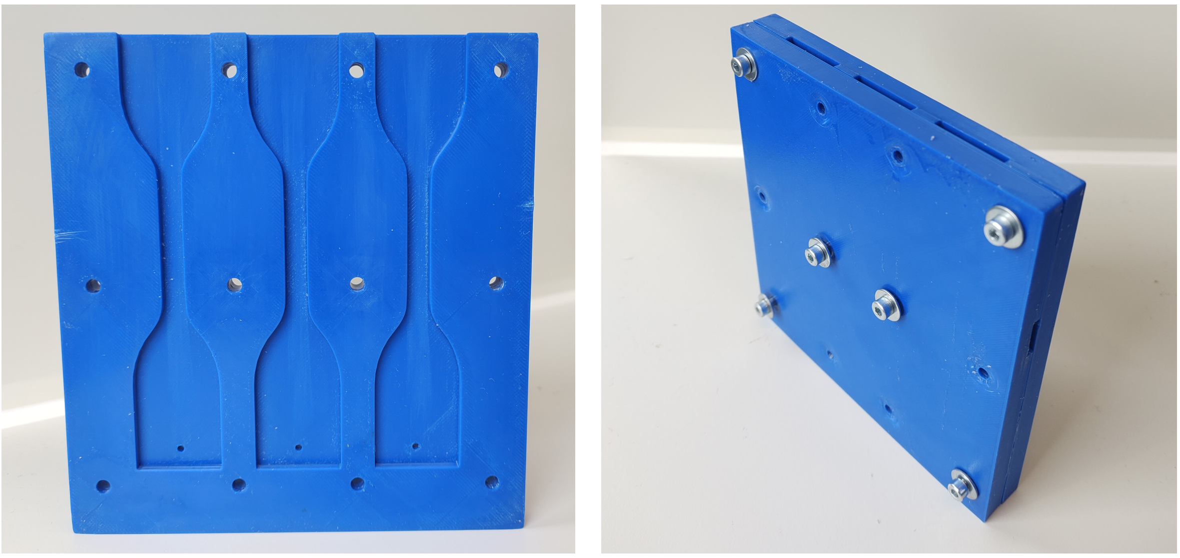
(a) (b)

Figure A.9: ABS mold cast for dogbone sample curing

A.6. Sample preparation procedure

The sample is prepared by covalently bonding the spiropyran molecules with the polymer PDMS (Sylgard 184) by introducing the cross-links into the polymer at the preparation stage.

PDMS preparation is done by mixing two main components - the PDMS base and the curing agent. The PDMS base is a viscous polymer that has vinyl terminal groups on the short chains of PDMS. PDMS curing agent is a low-viscosity liquid that contains a catalyst for triggering polymerization.

PDMS base and curing agent are obtained in the ratio of 10:1. In a standard preparation, $15\mathrm{g}$ of the base is mixed with $1.53\mathrm{g}$ of curing agent with $12\mathrm{mg}$ of spiropyran dissolved in $1\mathrm{mL}$ of toluene. All components are mixed thoroughly, degassed in a vacuum desiccator, poured into the molds using a syringe, and then left to cure in an oven at 70°.

B

Appendix B - Experimental setup validation and error calculation

Since the uniaxial tensile tester is in its first iteration stage, it is checked for various parameters that could lead to errors in the experiments due to the setup. The methods of validation are shown below.

B.1. Visual inspection

The uniaxial tensile tester demands that, ideally, all the forces should flow through a single axis. This minimizes the physical rotation of the components and reduces the transmittance of bending forces to data acquisition systems. During visual inspection, the orientation and misalignments of the peripheral components are recorded, and their effect on the final data acquisition is explained.

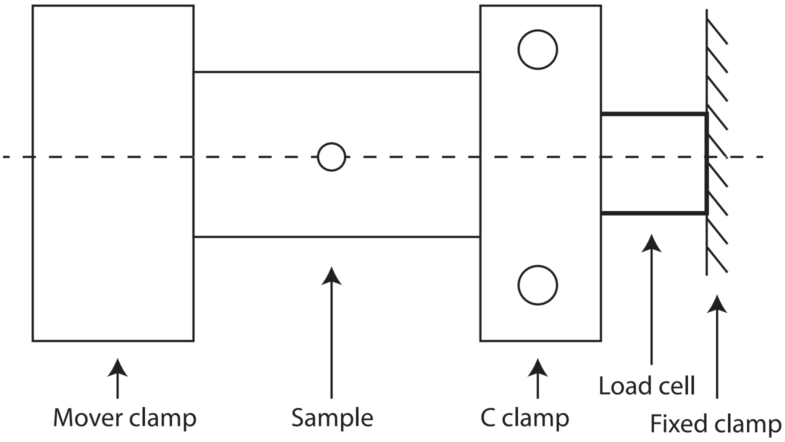

Figure B.1: Schematic of the experimental setup top view.

The misalignments are possible in all six degrees of freedom, i.e. three translational (Δx, Δy, Δz) and rotational (R_x, R_y, R_z). The rotational misalignments are calculated concerning the longitudinal direction of the linear stage (x-direction). The z-direction is considered to be opposite to the gravitational force, and the Y-direction is along the width of the linear stage. The translational misalignments are calculated with respect to the axis passing through the bolt and fixing the fixed clamp with the load cell.

Table B.1: Misalignments in peripherals of the experimental setup

	$\Delta x(\mathrm{mm})$	$\Delta y(\mathrm{mm})$	$\Delta z(\mathrm{mm})$	$R_x(^\circ)$	$R_y(^\circ)$	$R_z(^\circ)$
Fixed Clamp	-	-	-	0	0	0
C Clamp	0	0	0.2	H.E.	0	0
Mover Clamp	0	0	0	0	0	0

*H.E. refers to ”Human Error”

The fixed clamp has no rotational misalignments with the axis of the linear stage. Since the mover clamp is mounted on the mover, there are no misalignments. The surfaces of the fixed clamp, the load cell, and the C-clamp have surface contacts that restrict the rotations R_y and R_z. There are two types of misalignments possible in the C-clamp:

1. **Rotation about the pulling axis (R_x):**

   Rotational misalignment along the pulling axis causes the sample to twist. This causes a part of the sample to go out of focus from the camera's focal plane.

   The alignment is checked manually before every test. Thus, an error in R_x can arise as a human error. The alignment is ensured by measuring the height of both ends of the C-clamp from the ground using vernier calipers. The least count of the digital calipers is $0.01\mathrm{mm}$. The width of the C-clamp is $80\mathrm{mm}$. Assuming a human error-prone operator who allows a height difference of $0.05\mathrm{mm}$, this height difference translates to $tan^{-1}(0.05/80) = 0.035°$.

   The image captures the fluorescence coming from the entire 1mm thickness of the sample. Thus, a difference of 0.05mm in height does not affect the imaging. This is a very minute and reasonable tilt.

2. **Linear offset from the pulling axis (Δz):**

   The C-clamp is made such that when a 1mm thickness sample is clamped, the center of mass of the sample is perfectly aligned with the pulling axis. For the tests, however, a double-sided tape is wrapped around the sample for better adhesion. The double-sided tape's thickness is $0.2\mathrm{mm}$, which offsets the center of mass of the sample $0.2\mathrm{mm}$ away from the pulling axis.

   This shift causes bending in the peripheral components. If the components are stiff enough, which is true for the current setup, the bending forces are transmitted to the load cell. The bending force can be calculated by multiplying the maximum pulling force of 100 N with the offset, as shown in Eq. (B.1).

   $$M = F\Delta z = 100 * 0.2\mathrm{mm} = 0.02\mathrm{N\,m} \tag{B.1}$$

   No documentation regarding the effect of a bending moment on the load cell readings is found on the Futek website [57] (load cell supplier). A bending moment of $0.02\mathrm{N\,m}$ is negligible compared to the scale of forces involved in the experiment. Thus it can be concluded that the bending moment does not affect the load cell.

   Moreover, to be sure that the load cell is not under damage, the total stress is calculated as stated in the load cell documentation [57].

   $$\sigma_{max} = (A)F_x + (B)F_y + (C)F_z + (D)M_x + (E)M_y + (F)M_z$$

   For the experimental setup, F_z = 100N of maximum pulling force. M_y has two components i.e. $0.02\mathrm{N\,m}$ of bending force and $0.005\mathrm{N\,m}$ bending moment due to the gravity force for carrying $30\mathrm{g}$ weight of the C-clamp with the center of mass $20\mathrm{mm}$ away from load cell like a cantilever.

   Plugging the values of C, E, F_z, and M_y, the stress value of $\sigma_{max} = 42990$ units is obtained using the metrics of the supplier website [57]. When compared to the limit recommended on the website i.e. 87000 units, the obtained stress value is well below the breakage stress. Thus, it is concluded that the threat of load cell damage is non-existent.

To validate the working performance of the experimental setup, two tests are performed:

1. The setup needs to consistently record the data if the test is performed more than once. Force displacement repeatability curves ensure the reliability of the output data.
2. The setup force-displacement curves are compared with those of a Universal Testing Machine.

B.2. Repeatability

The repeatability of the experimental setup is tested to ensure that the force-displacement data remains the same for multiple runs under the same conditions.

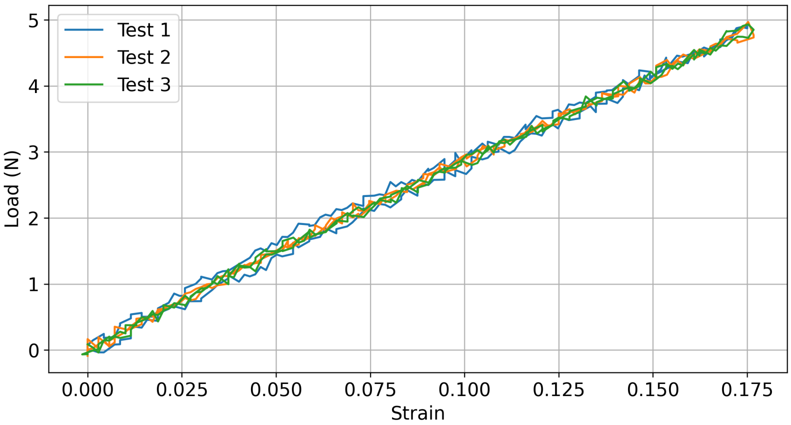

Figure B.2: Time decay heatmap section of the GUI.

Fig. B.2 shows force-displacement curves for three tests of a dogbone sample involving one strain cycle each. With a gauge length of $33\mathrm{mm}$, the dogbone is stretched $10\mathrm{mm}$ and then brought back to its unstretched state. As can be seen, the three force-displacement curves overlap each other completely, thus stating that the repeatability of the setup is good.

B.3. Validation with reference Universal Testing Machine

To account for any unaccounted possible issues with the experimental setup, its response is compared with that of an Instron 5500 Universal Testing Machine.

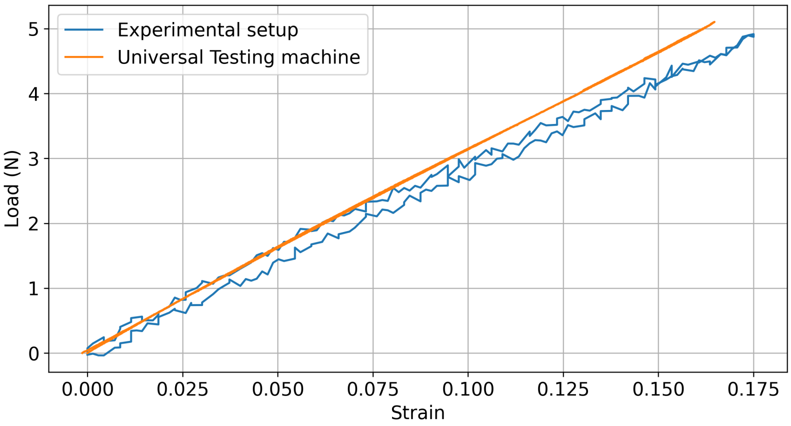

Figure B.3: Comparison of stress-strain curve for one stress cycle on experimental setup with that on UTM.

B.3.1. Backlash

Backlash is observed in the system when the linear stage changes its direction of motion. When the direction is reversed, the lead screw in the linear stage loses contact with the thread for a moment and then again re-establishes contact applying force in the opposite direction. This leads to a change in force without a change in the position of the stage, which is manifested as a vertical line in the force-displacement curve of the tensile test. As shown in Fig. B.3, no vertical line can be seen in the force-strain, which explains that there is undetectable backlash in the system.

B.3.2. Force-strain curve comparison

In Fig. B.3, the orange line represents the force-strain curve for the reference UTM, and the blue line represents the same obtained by the main experimental setup. The fact that both curves are very similar is proof that the main experimental setup provides accurate data with minimal offset from the reference. The small difference in the slope of the curves is attributed to the small gauge length of $12\mathrm{mm}$ for the extensometer used during the UTM test.

B.4. Accounting for stress relaxation of the setup

Like every other experimental setup, the experimental setup shows stress relaxation with the PDMS sample during the test. The stress relaxation can originate from both the viscoelastic PDMS sample and the experimental setup itself.

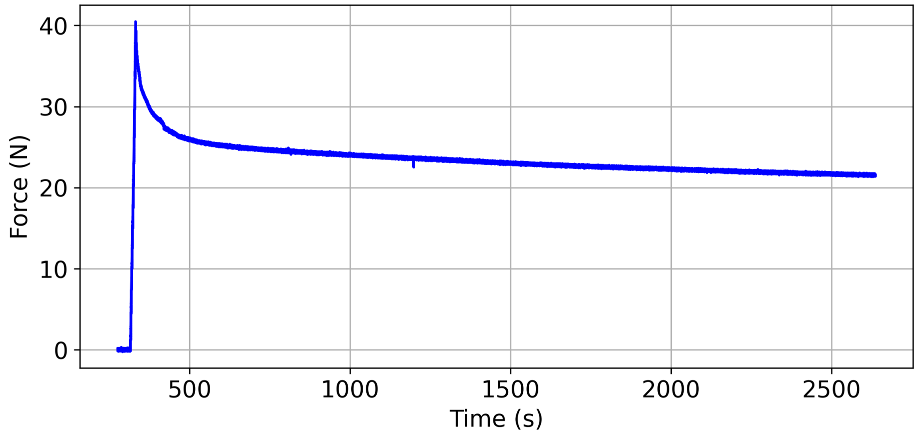

Figure B.4: Comparison of stress-strain curve for one stress cycle on experimental setup with that on UTM

When the sample is stretched, the force with which the stage is pulling also increases simultaneously. Once the sample is stretched to a certain strain, the force starts to decay to smaller values. This is followed by the stabilization of the decay rate after a certain time. Fig. B.4 shows the typical stress relaxation curve observed during the experiments in this thesis. As can be seen, the time frame of the stress relaxation is about 15 minutes. To account for stress relaxation, the experiment is performed after 45 minutes of stretching. This time is much beyond the stress relaxation timeline, thus, the sample has achieved a static state for the experiments.

C

Appendix C - Simulation framework

In this Appendix chapter, the simulation methodology of the thesis is discussed in more detail. In order to get the material model for the numerical simulation, uniaxial tensile tests are performed on an ASTM D412 (Type C) dogbone sample. The stress-strain curve obtained is fitted to various hyperelastic material models, and the best-fit model is used for simulation.

C.1. Strain data acquisition during tensile test

For the tensile test, the dogbone sample is stretched at a rate of $10\mathrm{mm}$ per minute until failure. The force data is obtained from the load cell, whereas the strain is calculated optically through image acquisition and postprocessing.

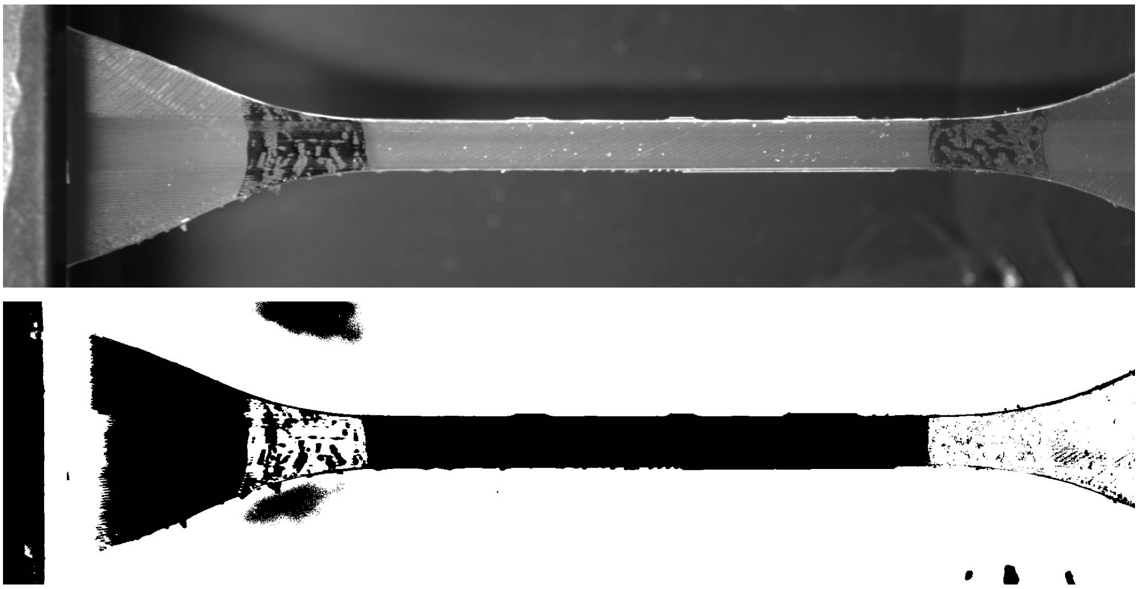

Figure C.1: Image of a dogbone sample and its corresponding binary image

Fig. C.1 shows the dogbone sample during the test. Gauge length markings were made at $33\mathrm{mm}$ distance using an acrylic marker. The .tif image is converted to a binary image using the Maximum Entropy Method. The binary image is shown in Fig. C.1.

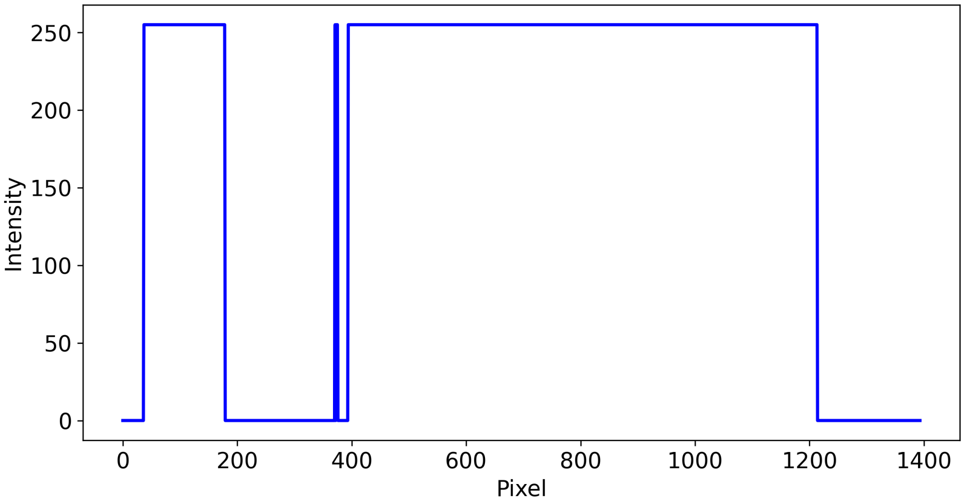

Figure C.2: Intensities of pixels in the binary image along the horizontal line

A horizontal line is drawn on the binary image and a line graph of the intensities, as shown in Fig. C.2 is extracted. A Python code measures the distance between the two dark acrylic markers for every frame and provides the strain data. This strain data is clubbed with the force data from the load cell to get the stress-strain curves.

C.2. Parametric fitting for material model selection

The stress-strain curve from the uniaxial tensile test is parametrically fit to various hyperelastic models such as the Neohookean model, Mooney-Rivlin two-parameter model, Ogden fourth-order model and the Yeoh model.

The workflow for the Yeoh model is shown here. The strain energy density of the material using a Yeoh model can be modeled as

$$W = C_1(I_1 - 3) + C_2(I_1 - 3)^2 + C_3(I_1 - 3)^3.$$

The zz component of the First Piola-Kirchoff stress tensor P_{zz} can be obtained as $Pzz = \frac{\mathrm{d}W}{\mathrm{d}\lambda_3}$. For a plane stress situation, as in our case, $P_{zz} = 0$. This gives a relation between principal stretches as

$$\lambda_2 = \lambda_3 = \frac{1}{\sqrt{\lambda_1}},$$

Plugging this solution in the expression of P_{xx} gives the expression that can be fit parametrically with the experimental data.

$$P_{xx} = \frac{2\left(\lambda_1^3 - 1\right)\left(\lambda_1\left(c_1\lambda_1 + 2c_2\left(\lambda_1^3 - 3\lambda_1 + 2\right)\right) + 3c_3(\lambda_1 + 2)^2(\lambda_1 - 1)^4\right)}{\lambda_1^4}.$$

The parametric fitting is done in COMSOL Multiphysics software using the hyperelastic material models mentioned above. Fig. C.3 shows the performance of the models.

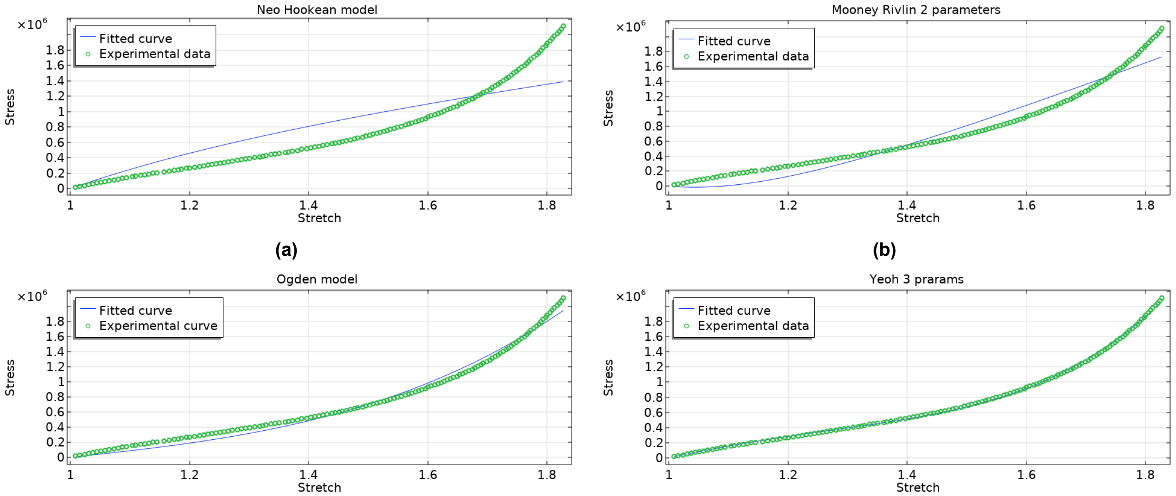

(a) (b)

(c) (d)

Figure C.3: Experimental stress-strain curve with parametrically fitted (a) Neohookean model, (b) Mooney-Rivlin two-parameter model, (c) Ogden four-parameter model, and (d) Yeoh three-parameter model.

Table C.1: Material properties for all fitted models

Hyperelastic Model	**Material Parameters**							
Neo-Hookean model	μ							
	9.08×10^5							
Mooney-Rivlin 2 parameter model	C_{10}	C_{01}						
	$1.40 * 10^6$	-1.53×10^6						
Ogden model	μ_1	α_1	μ_2	α_2	μ_3	α_3	μ_4	α_4
	$2.315e4$	6.057	$2.316e4$	6.057	$2.3156e4$	6.057	$2.314e4$	6.057
Yeoh model	C_1	C_2	C_3					
	2.86×10^5	-4.39×10^4	8.36×10^4					

Since the best fit is obtained from the Yeoh model, the Yeoh model is used for the numerical simulation that is eventually used for correlation.

C.3. Numerical simulation

Numerical simulation is done on COMSOL Multiphysics. The length and width of the sample are recorded during the actual experiment and the length is adjusted in the geometry before the final simulation. In the case of the final experiment runs, the length and width of the sample are 25.74 mm and 30.02 mm respectively. A hyperelastic incompressible Yeoh model is used as the material. The mesh is kept extremely fine around the hole to get a good spatial resolution in the region of interest. In order to confirm the validity of the COMSOL solution, a mesh refinement study is done in order to save on the computing power whilst also ensuring that the solution is accurate enough.

C.3.1. Mesh refinement convergence study.

In order to confirm that the mesh is fine enough for the results to converge, a mesh refinement convergence study is performed for five different levels of mesh from a coarser mesh to a finer mesh.

Since the geometry is subject to high strains such as $\varepsilon = 1$, to avoid skewness of elements, a mesh with quadratic elements is chosen. Boundary layers are defined around the hole and the rest of the mesh is set to be a ”Free Quad mesh” in COMSOL Multiphysics. The size of the ”Free Quad” mesh is selected from one of the predefined mesh settings from ”Very Coarse” to ”Extremely Fine” in COMOSL. The boundary layers can be configured using the following parameters:

1. **Distributions:** Number of elements on each quarter edge of the circular hole.
2. **Boundary layer thickness:** Total distance of the boundary layers from the edge. It can be set in the ”Total thickness” section in COMSOL.
3. **Number of boundary layers:** Number of layers in the boundary mesh

The structure of the mesh in COMSOL Multiphysics software and the specific inputs for the mesh configuration properties are shown in Fig. C.4.

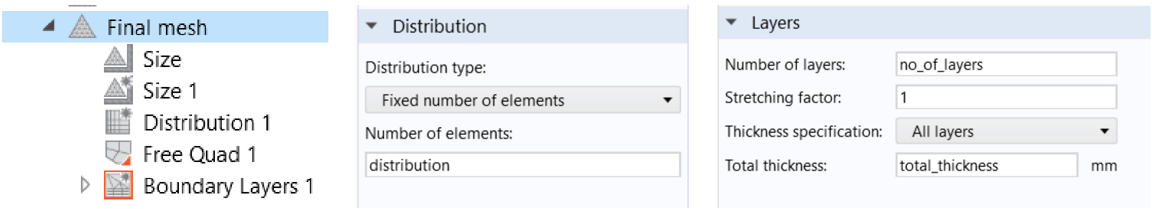

Final mesh
Size
Size 1
Distribution 1
Free Quad 1
Boundary Layers 1

Distribution
Distribution type: Fixed number of elements
Number of elements: distribution

Layers
Number of layers: no_of_layers
Stretching factor: 1
Thickness specification: All layers
Total thickness: total_thickness mm

(a) (b) (c)

Figure C.4: Mesh structure and properties tuned for various mesh sizes

Five meshes are created by varying the parameters as shown in Table C.2. The meshes gradually get finer, from mesh 1 to mesh 5, with mesh 5 being the finest. The zoomed-in versions of the five meshes can be seen in Fig. C.5.

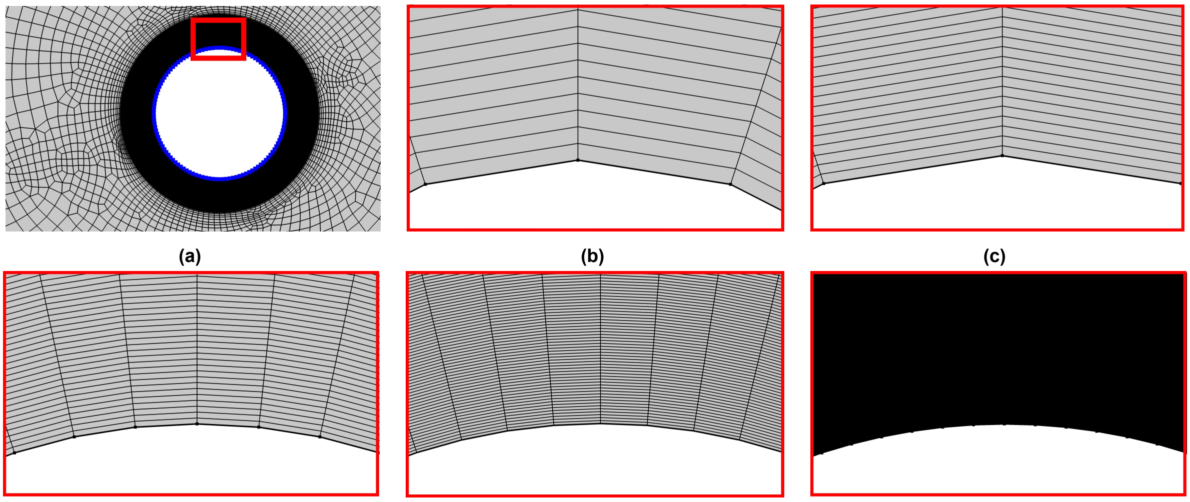

(a) (b) (c)

(d) (e) (f)

Figure C.5: (a) Boundary layer mesh around the hole, (b-f) Close-ups of meshes 1-5 near the hole boundary

Table C.2: Parameters of meshes in the mesh convergence study

Mesh no.	Distribution	Number of boundary layers	Boundary layer thickness (mm)	Remaining mesh size	Stress (MPa)	% change in stress	Solution time (s)
Mesh 1	5	60	2.5	Extra coarse	9.2361	-0.46%	3
Mesh 2	5	60	1.25	Coarse	9.193	-1.26%	3
Mesh 3	15	100	1.25	Normal	9.0766	0.06%	12
Mesh 4	20	200	1.25	Finer	9.0819	0.015%	36
Mesh 5	30	1000	1.25	Extremely Fine	9.0833	-	157

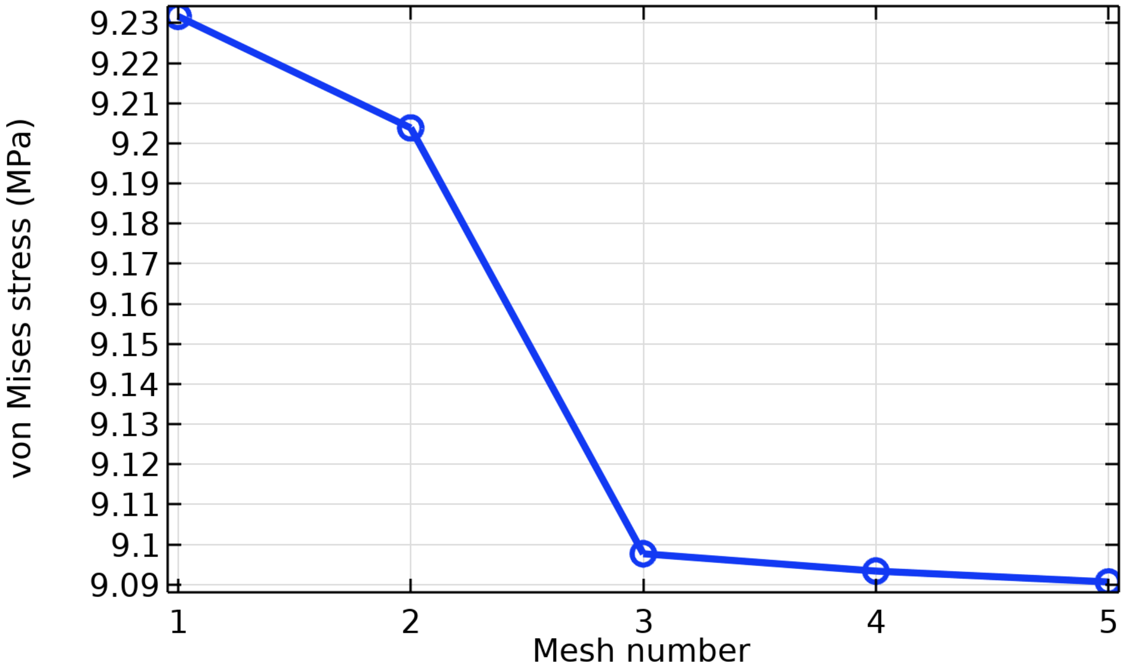

Figure C.6: Stress convergence plot for a point above the hole with mesh refinement.

A mesh convergence plot showing the von Mises stress in the region at the top of the hole is plotted for all five meshes. The results start to converge after the fineness of the third mesh. However, since the finest mesh takes only three minutes to run, the finest mesh has been used during the thesis to get the most accurate results.

D

Appendix D - Correlation data

The codes developed in this thesis are uploaded to the following GitHub link: `https://github.com/anujj19121999/Anuj_Masters_thesis`

The following tables note the correlations obtained by correlating various combinations of continuum mechanics quantities with the fluorescence and decay rate time constant. The correlations with fluorescence greater than 0.6 and correlations with decay rate time constant greater than 0.4 have been marked in green.

Table D.1: Nomenclature of continuum mechanics quantities.

Symbol	**Quantity**
$\mathbf{F}$	Deformation gradient tensor
$\mathbf{C}$	Right Cauchy-Green deformation tensor
$\mathbf{b}$	Left Cauchy-Green deformation tensor
$\mathbf{E}$	Green-Lagrange strain tensor
$\mathbf{e}$	Euler-Almansi strain tensor
$\mathbf{P}$	First Piola-Kirchoff stress tensor
$\mathbf{S}$	Second Piola-Kirchoff stress tensor
$\boldsymbol{\sigma}$	Cauchy stress tensor

Table D.2: Correlations of simulation quantities with fluorescence and decay rate time constant.

Quantity	Correlation with fluorescence	Correlation with decay rate time constant
F_{xx}	0.24	0.18
F_{xy}	0.03	0
F_{yx}	-0.02	0.02
F_{yy}	-0.44	-0.38
C_{xx}	0.36	0.26
C_{xy}	0.02	0.01
C_{yy}	-0.14	-0.16
b_{xx}	0.44	0.30
b_{xy}	0.03	0.01
b_{yy}	-0.46	-0.41
E_{xx}	0.36	0.26
E_{xy}	0.02	0.01
E_{yy}	-0.14	-0.16
e_{xx}	-0.01	-0.01
e_{xy}	0	0
e_{yy}	-0.02	-0.01
P_{xx}	0.74	0.44
P_{xy}	0.02	0.01
P_{yx}	0.02	0.01
P_{yy}	-0.32	-0.37
S_{xx}	0.7	0.43
S_{xy}	0.02	0
S_{yy}	-0.19	-0.27
σ_{xx}	0.7	0.43
σ_{xy}	0.02	0
σ_{yy}	-0.36	-0.40

Table D.3: Correlations of eigenvalues of simulation quantities with fluorescence and decay rate time constant.

Quantity	Correlation with fluorescence	Correlation with decay rate time constant
$\mathbf{F}$ - λ_{max}	0.23	0.16
$\mathbf{F}$ - λ_{min}	-0.40	-0.34
$\mathbf{F}$ - $(\lambda_{\text{max}} - \lambda_{\text{min}})$	0.37	0.29
$\mathbf{C}$ - λ_{max}	0.45	0.31
$\mathbf{C}$ - λ_{min}	-0.52	-0.44
$\mathbf{C}$ - $(\lambda_{\text{max}} - \lambda_{\text{min}})$	0.53	0.38
$\mathbf{b}$ - λ_{max}	0.45	0.31
$\mathbf{b}$ - λ_{min}	-0.52	-0.44
$\mathbf{b}$ - $(\lambda_{\text{max}} - \lambda_{\text{min}})$	0.53	0.38
$\mathbf{E}$ - λ_{max}	0.45	0.31
$\mathbf{E}$ - λ_{min}	-0.52	-0.44
$\mathbf{E}$ - $(\lambda_{\text{max}} - \lambda_{\text{min}})$	0.53	0.38
$\mathbf{e}$ - λ_{max}	-0.02	-0.01
$\mathbf{e}$ - λ_{min}	-0.02	-0.01
$\mathbf{e}$ - $(\lambda_{\text{max}} - \lambda_{\text{min}})$	0.02	0.01
$\mathbf{P}$ - λ_{max}	0.75	0.44
$\mathbf{P}$ - λ_{min}	-0.37	-0.38
$\mathbf{P}$ - $(\lambda_{\text{max}} - \lambda_{\text{min}})$	0.76	0.47
$\mathbf{S}$ - λ_{max}	0.71	0.44
$\mathbf{S}$ - λ_{min}	-0.31	-0.33
$\mathbf{S}$ - $(\lambda_{\text{max}} - \lambda_{\text{min}})$	0.72	0.47
$\boldsymbol{\sigma}$ - λ_{max}	0.70	0.43
$\boldsymbol{\sigma}$ - λ_{min}	-0.42	-0.41
$\boldsymbol{\sigma}$ - $(\lambda_{\text{max}} - \lambda_{\text{min}})$ (Tresca)	0.71	0.43
$\boldsymbol{\sigma}_{\text{VM}}$	0.70	0.43

Table D.4: Correlations of invariants of simulation quantities with fluorescence and decay rate time constant. I_1 and I_2 denote first and second invariants, respectively.

Quantity	Correlation with fluorescence	Correlation with decay rate time constant
$\mathbf{F}$ - I_1	0.05	0.01
$\mathbf{F}$ - I_2	-0.17	-0.17
$\mathbf{C}$ - I_1	0.35	0.22
$\mathbf{C}$ - I_2	-0.20	-0.22
$\mathbf{b}$ - I_1	0.35	0.22
$\mathbf{b}$ - I_2	-0.20	-0.22
$\mathbf{b}$ - I_1 (isochoric)	0.53	0.37
$\mathbf{b}$ - I_2 (isochoric)	-0.16	-0.15
$\mathbf{E}$ - I_1	0.35	0.22
$\mathbf{E}$ - I_2	-0.61	-0.45
$\mathbf{e}$ - I_1	-0.02	-0.01
$\mathbf{e}$ - I_2	0.01	0.01
$\mathbf{P}$ - I_1	0.73	0.41
$\mathbf{P}$ - I_2	0.24	0.01
$\mathbf{S}$ - I_1	0.66	0.42
$\mathbf{S}$ - I_2	0.28	0.04
$\boldsymbol{\sigma}$ - I_1	0.70	0.36
$\boldsymbol{\sigma}$ - I_2	0.28	0.04